Integrated Low-Power Wireless Systems for the Next Generation of IoT, Sensors and Microrobots

by

Alex Moreno

A dissertation submitted in partial satisfaction of the

requirements for the degree of

Doctor of Philosophy

in

Engineering – Electrical Engineering and Computer Sciences

in the

Graduate Division

of the

University of California, Berkeley

Committee in charge:

Professor Kristofer S.J. Pister, Chair
Professor Ali M. Niknejad
Professor Roya Maboudian

Spring 2023

The dissertation of Alex Moreno, titled Integrated Low-Power Wireless Systems for the Next Generation of IoT, Sensors and Microrobots, is approved:

Chair _____ Date _____

_____ Date _____

_____ Date _____

University of California, Berkeley

Integrated Low-Power Wireless Systems for the Next Generation of IoT, Sensors and Microrobots

Abstract

Integrated Low-Power Wireless Systems for the Next Generation of IoT, Sensors and Microrobots

by

Alex Moreno

Doctor of Philosophy in Engineering – Electrical Engineering and Computer Sciences

University of California, Berkeley

Professor Kristofer S.J. Pister, Chair

The relentless pursuit of smaller, cheaper, and lower-power wireless electronics has driven the design of novel radio designs such as crystal-free radios, that offer a fully functional wireless node with minimal external components.

At Berkeley, the Single-Chip Micro Mote (SCµM), a 3x2 mm, 4.2 mg crystal-free 802.15.4 and BLE wireless SoC, was developed to make swarms of mm-scale microrobots a reality. This dissertation will begin by discussing SCµM in the context of system integration, including the challenge of accurate channel frequency tuning in the face of varying temperature and voltage conditions. By characterizing the RF frequency's dependence on voltage droop during transmission, we were able to compensate for the RF frequency shift, increasing SCµM's 802.15.4 packet payload from 10B to 125B while powered from a solar cell.

Several integrated systems with SCµM at their core will also be discussed, including a wirelessly-actuated, solar-powered, quarter-sized, 286 mg microrobot MEMS gripper for microrobotics; and a 244 mg, 5x8 mm BLE SCµM tag, which was used to track an Asian hornet—feats not possible with commercial off-the-shelf components.

The dissertation will conclude with a look at how future crystal-free radios could be designed to address the inherent instability of power sources in low-power systems, potentially pushing the envelope for even smaller, cheaper, lower-power and more reliable wireless electronics.

Updates and errata to this dissertation can be found at this link: `https://drive.google.com/drive/folders/1SsBKq3GIVkbJte-pAhNKaIxvdvXHdD1z?usp=sharing`

To my mother and father:

Thank you for your hard work, support and sacrifice that has given me the opportunity to get to this point. I hope I made you proud.

A mi madre y a mi padre:

Gracias por su arduo trabajo, apoyo y sacrificio que me han dado la oportunidad de llegar hasta este punto. Espero haberlos hecho orgullosos.

Contents

List of Figures

List of Tables

Acknowledgments

I would like to acknowledge all of the people involved in the development of

- SCµM: Filip Maksimovic, Brad Wheeler, David C. Burnett, Osama Khan, Sahar Mesri, Ioana Suciu (Universitat Oberta de Catalunya), Lydia Lee, Arvind Sundararajan, Bob Zhou, Rachel Zoll, Andrew Ng, Tengfei Chang (Inria, EVA Team), Xavier Villajosana (Universitat Oberta de Catalunya), Thomas Watteyne (Inria, EVA Team), Ali Niknejad, and Kristofer S.J. Pister
- Zappy2: Jan Rentmeister (Dartmouth), Professor Jason Stauth (Dartmouth)
- The MEMS Gripper: Daniel Teal, Hani Gomez, Craig Schindler, Dillon Acker-James and Wei Li
- The Lithium-ion Micro Batteries: Anju Toor, Professor Ana Arias

Thank you Lydia Lee for always being kind and supportive. You've helped me get to the finish line. Everyone in my lab has helped me in one way or another so thank you all: Daniel Teal, Hani Gomez, Alexander Alvara, Mauricio Bustamante, Craig Schindler, Daniel Contreras, Dillon Acker-James, Titan Yuan, Daniel Lovell, Anju Toor, David C. Burnett, Brad Wheeler, Fil Maksimovic, Felipe Campos, Andrew Fearing, Yu-Chi Lin, and Yichen Liu. I apologize if you don't see your name on here know I've appreciated having worked together.

I would like to give a shout-out to the the talented undergraduate researcher Austin Patel. I have appreciated his kind personality, dedication and perseverance to getting what needs to be done done (e.g. 3 a.m. debug sessions, weekend work marathons, conference paper deadlines, etc).

I would like to thank my advisors Kris and Ali for believing in me and pushing me to be a better researcher.

Last but not least, I would like to thank my dad, my mom, brother and sister. Thank you for listening to my struggles and celebrating my victories.

This work was supported by the National Science Foundation Graduate Research Fellowship Program under Grant No. DGE 1752814. Any opinions, findings, and conclusions or recommendations expressed in this material are those of the authors and do not necessarily reflect the views of the National Science Foundation.

Chapter 1

The Components of a Low Power System

1.1 The Single Chip micro Mote: a Crystal-Free 802.15.4/Bluetooth Wireless Sensor

Microrobot platforms are likely to enable many new defense, intelligence, and commercial applications. Existing microrobot platforms have the potential to run [22], jump [82], and fly [26] autonomously, although at present they are tethered to power and control. Cigarette-sized rockets have the potential to enable rapid distribution of a sensor network, or counter swarms of small UAVs [70, 25]. All of these platforms have a common need for an embedded controller with the capability to run low-level control algorithms, provide diagnostic communication during application development, and provide 2D or 3D location capability. In addition, RF mesh networking is an enabling capability for many robotic applications and non-robotic applications such as industrial process automation and factory automation [95].

Unfortunately, while there are many commercial chips which include a microprocessor and a radio in a sub-cm package, all of these chips require a significant number of external components such as crystal oscillators for time and frequency reference, bypass capacitors for power supplies, a balun for single-ended antennas, etc. As a result, the smallest useful system featuring these commercial chips is typically a printed circuit board with dimensions on the order of a centimeter and weight close to a gram [83]. This is a prohibitively large payload for a sub-cm robot to carry. In 2013 work began in earnest to design a chip that would meet the requirements of microrobot control and communication with no external components. Funded by DARPA, NSF, and many BSAC member companies over a period of seven years, the chip described below is a result of that effort.

Figure 1.1: SCµM3C on a Penny

Capabilities and operation

SCµM programs are typically written in C in a standard development environment. Binaries are loaded into SRAM via a USB dongle with both wired and wireless optical programming capability. At boot, the chip consumes roughly 0.35mA. Once software has been loaded and begins executing, this baseline current can be dropped to roughly 0.15mA plus 50µA/MHz times the processor clock frequency. The processor clock frequency can be set from tens of kHz to 20 MHz.

Optical Bootloading

An optical bootloader enables contact-less programming, command reception, and timing calibration of SCµM with an infrared LED or visible laser pointer at a distance of roughly 5cm[97]. The subsystem consists of an integrated photodiode and an analog front-end, as

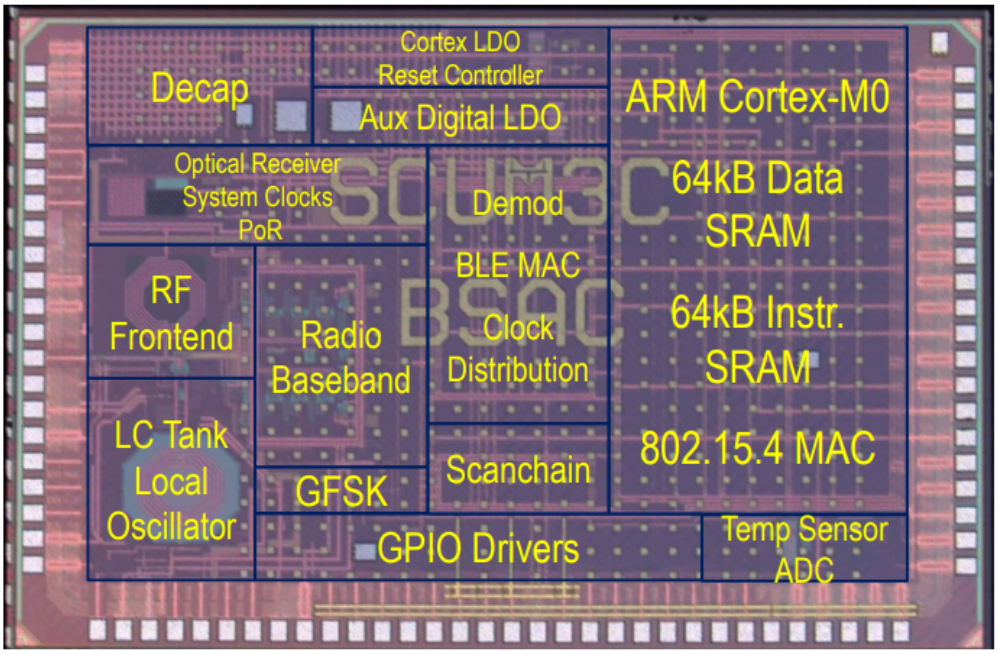

Figure 1.2: Annotated die photo of the Single-Chip micro-Mote (SCµM), a chip custom-designed to control microrobots. SCµM is $2\times3\times0.3\text{mm}^3$ with a mass of ≈ 4.3mg.

well as a self-timed clock-and-data recovery (CDR) scheme which relies on an analog delay to implement pulse width modulation. This allows a user to load software onto the mote's microprocessor without a physical connection between the programming element and the mote, and it is conducive to the simultaneous programming of multiple motes. The optical bootloader subsystem consumes 640nW standby power and 1.52µW active power with a total area of 16,900μm^2 [97]. The same hardware is used for lighthouse localization (Section 1.1).

Standards-compatible RF Communication

Existing wireless systems-on-chip rely on external components—capacitors, inductors, crystals, and MEMS resonators [30]—to obtain a sufficiently accurate frequency reference for operation, and the necessity of such parts places a lower bound on system cost, size, and weight. By removing these off-chip references and instead using on-chip oscillators for frequency generation with a one-time calibration [52], we achieve IEEE 802.15.4-compatible radio communication and BLE packet transmission with only three external connections—power, ground, and antenna [54].

A wirebond across the chip can be used as an antenna, enabling transmission to cell phones up to a distance of roughly 3 meters. An RSSI of -85 dBm was measured at a distance of 1 m on a previous iteration of the SCµM with the same receiver hardware. The entire chip including the microprocessor consumes less than 2 mW of power during transmission

or reception. Transmission power and receive sensitivity for 802.15.4 packets are −10 dBm and −82 dBm.

The ability to wirelessly transmit robot telemetry information during robot development and debugging is quite useful, and the ability to send a wireless trigger to the robot to initiate operations could be useful.

Sub-centimeter 3-DoF Localization

SCµM has the capability of sub-centimeter-precision 3 degree of freedom (3-DoF) localization, using a COTS lighthouse localization system [1]. This is the first time such a lighthouse localization system has been used to localize a monolithic single-chip wireless system [97]. Lighthouse localization is a form of "outside-in" localization which relies on a "lighthouse beacon" to generate a series of of infrared pulses and laser scans [73]. By repurposing the on-chip optical receiver hardware used for optical bootloading (Section 1.1) and determining the time between the pulse and the laser scan's reception on-chip, SCµM can calculate its azimuth and elevation with respect to a single beacon. With a commercially available HTC Vive V1 lighthouse base station, [97] localized azimuth and elevation with an RMS error of 0.386° and 0.312°, respectively. Because each mote calculates only its own azimuth and elevation, this method scales well to localizing large numbers of motes (or robots) simultaneously. Adding a second lighthouse beacon to this system allows us to triangulate a 3 degree-of-freedom position of SCµM with centimeter accuracy.

Using COTS lighthouse beacons is useful during development and in some application environments. In many applications, however, there will be no pre-existing infrastructure. Networks of micro robots may still be able to self-localize however. Using MEMS scanning mirrors it is possible to build laser scanners with a volume and mass compatible with microrobot platforms [47]. By having each robot act as both a beacon and a receiver, the robots localize each other, and only a small number of robots will need to have a sense of their absolute position.

Microrobots will require closed-loop position control to stay on course. The versatility of the platform can be significantly enhanced with computational power greater than hard-coded PID-style control loops. The inclusion of a Cortex-M0 microprocessor integrated with the chip's analog hardware allows for a flexible platform with which to implement control methods, modifiable in software, and configurable without physically contacting the platform (Section 1.1).

GPIO

SCµM includes 16 GPIOs whose signals can be routed to and from various sub-systems within the chip and configured via software. Several interrupt inputs are available, as well as an ADC and UART. The IO pad ring voltage is supplied from a separate pin from the battery voltage, and can be driven to at least 3.6 V. The R_{on} looking up or down at the

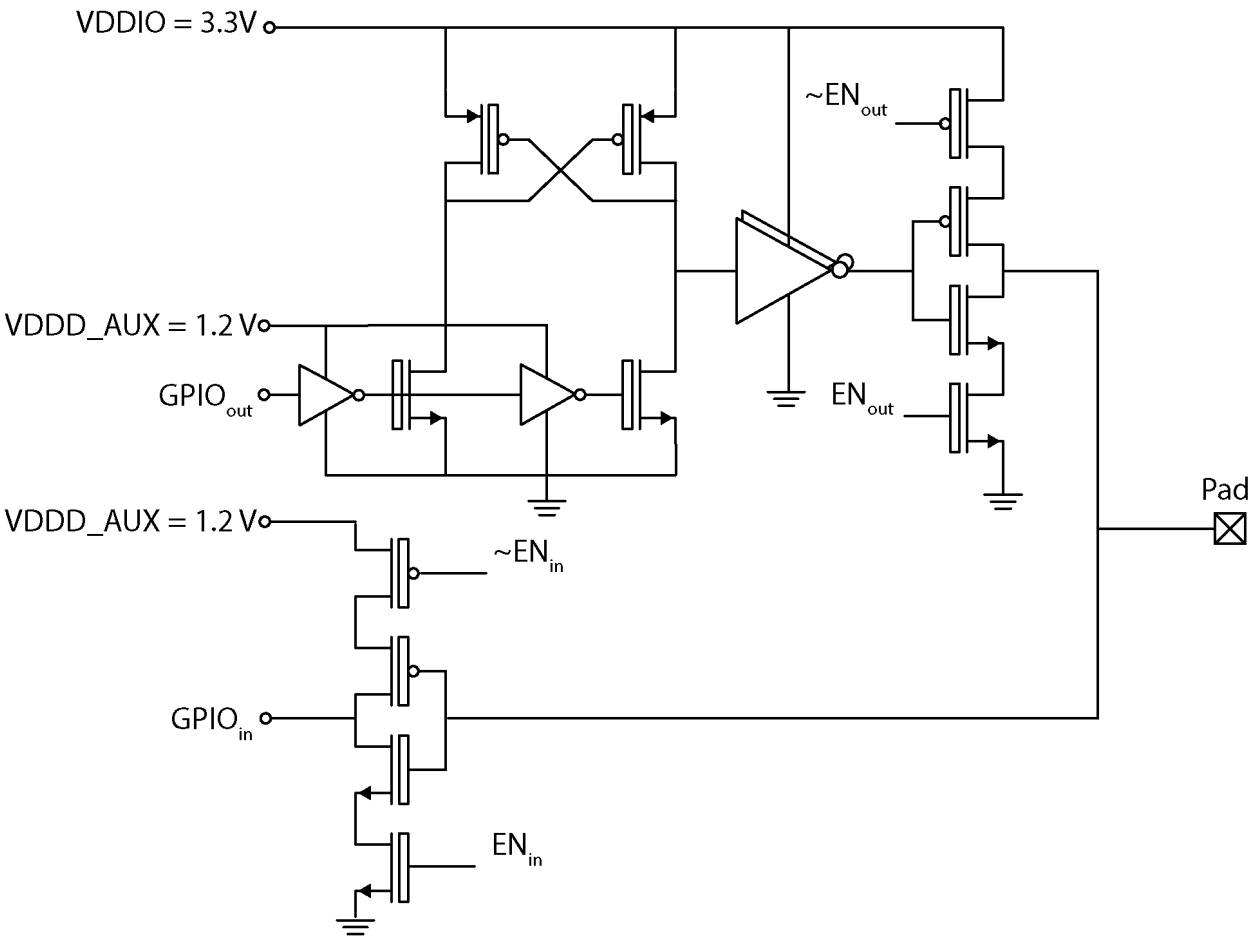

Figure 1.3: GPIO circuit schematic

Table 1.1: $GPIO_{output}$ Specifications

Specification	Value
VDDIO	0.8-3.6 V
VDDAUX	0.8-1.2 V
F_{max} @ HCLK = 10 MHz	734.25 KHz
$I_{VDDIOleakage}$ @ VDDIO = 3.3 V	4.37 nA
$I_{sink/source}$ @ VDDIO = 3.3 V	19 mA

output of GPO can bee seen in Fig. 1.4. The schematic of the GPIO drivers can be seen in Fig. 1.3 The relevant specifications for the GPO can be seen in Table 1.1.

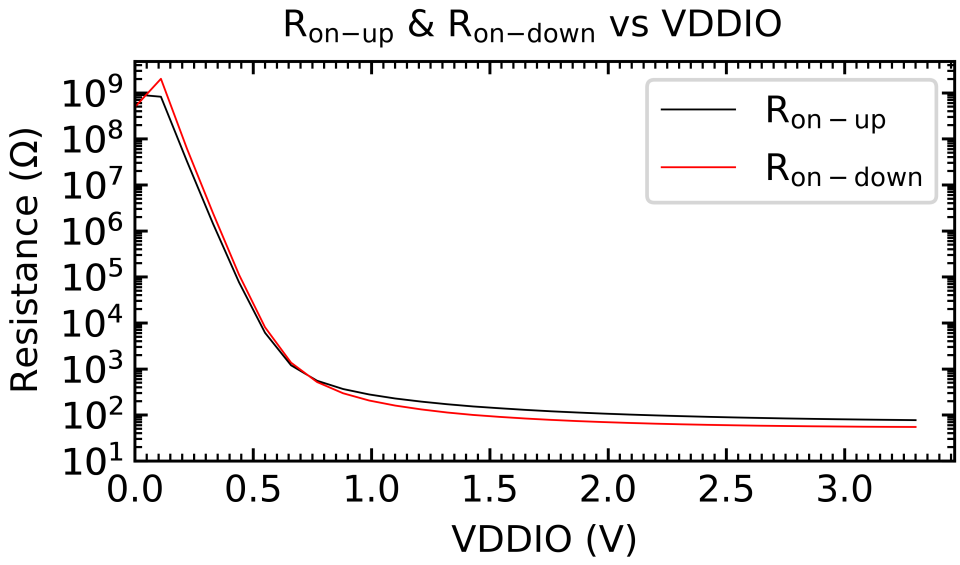

Figure 1.4: $GPIO_{output}$ Resistance vs VDDIO

Sensors and Sensor Interfacing

SCµM contains an analog-to-digital converter (ADC) with a programmable gain amplifier (PGA) to digitize on-chip and off-chip signals. On-chip sensors include a temperature sensor and voltage supply sensor. The ADC has been used to interface with an H2S gas sensor and a lactate sweat sensor. Wireless transmission of gas sensor information has been demonstrated with just SCµM and the sensor chip and no other components [7]. Serial digital interfacing with external sensors including a commercial nine-axis inertial measurement unit (ICM-20948) has been demonstrated. A MEMS IMU is likely to be critical for microrobot control in practical applications.

In addition to an analog temperature sensor, the chip is able to generate a temperature estimate by taking a ratio of two low frequency oscillators. This is somewhat similar to the technique presented in [40], in which two ring oscillators with different temperature coefficients are counted against one another. The two oscillators on this chip that are compared are the 32 kHz oscillator intended to act as a surrogate for a low-frequency crystal timer, and the 2 MHz oscillator used as the chipping clock for data transmission.

The maximum error on this chip was approximately 2.4 °C, although this varies from chip to chip. The sensor, as well as more information about the implementation, is discussed in [100].

Networking

OpenWSN and 802.15.4 OpenWSN is an open-source software project which has demonstrated an implementation of the IEEE/IETF standards-compliant 6TiSCH constrained net-

work protocol stack for wireless mesh networks [96]. SCµM was designed to run the OpenWSN IPv6 mesh networking communication stack.

Equipping each microrobot with an OpenWSN-capable radio enables them to form a cooperative mesh network that increases the effective range of the robots communication (beyond that of what would otherwise be a home base) and makes them resilient to RF environments and fading. Using the wireless subsystem on the single-chip mote and an FPGA emulating the on-chip digital hardware, [14] demonstrated the single-chip mote joining an OpenWSN network. Since then, the radio with integrated digital baseband and processor has communicated with Texas Instruments CC2538 802.15.4 radios.

The physical layer that OpenWSN is built on is IEEE 802.15.4, a standard that uses HSS-OQPSK modulation.

Data is sent with a directly modulated LC oscillator where a tunable capacitor is switched in and out of the resonator at the 2 MHz data rate. The receiver is a low-IF superheterodyne architecture with switched-capacitor baseband filtering, a 4-bit analog to digital converter, and a matched filter demodulator. More detail of the implementation is described in [52].

Speaking standards-compatible RF protocols without an external crystal is a difficult challenge [8]. Requirements for center-frequency accuracy, modulation frequency, bit rate, and inter-packet interval timing are typically measured in tens of parts per million, whereas on-chip oscillator phase noise and frequency error are more often in units of percent. SCµM solves these problems using a combination of circuit techniques and packet-based and network-based dynamic calibration [89, 88]. It is possible for a mote with no initial calibration to learn everything that it needs to know about time and frequency just from the packets flying around in the network that it joins.

Bluetooth Some Bluetooth Low Energy (BLE) functionality is available in SCµM. Beacon transmissions with sensor payload data are received routinely by cell phones. Reception range depends on the antenna used, with a range of several meters using a wirebond antenna across the chip, and a range of several tens of meters using a commercial antenna. Reception of BLE packets by the mote has not yet been demonstrated. The radio can move between 802.15.4 and BLE modes in a matter of milliseconds, allowing a node to relay data out of an 802.15.4 mesh to a nearby cell phone.

1.2 Energy Storage

The Ceramic Capacitor

We all know that there is a tolerance with capacitors ±20% however it was surprising how bad capacitors truly were when I tested them. I first came across this issue when the voltage drop was significantly higher than what theory said it would be in the [63]. Thus characterizing this seemingly simple capacitor started I had one approach to testing using the standard LCR meter. I provided a signal that was 1 kHz Level = 1.8 V and BIAS=1.5 V

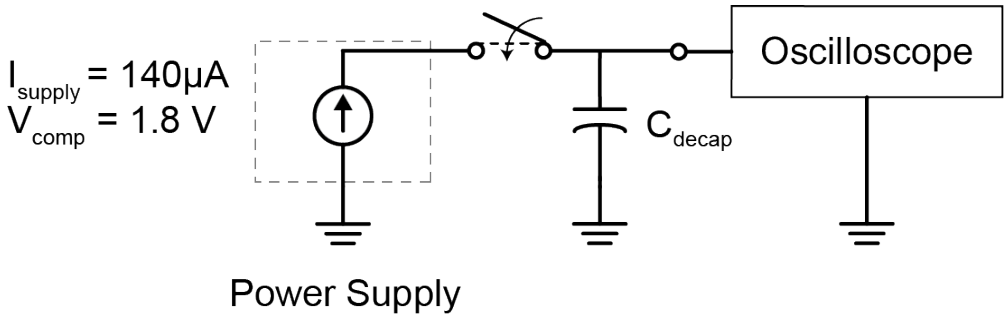

Figure 1.5: The test setup for measuring the effective capacitance by applying a 140 µA current source and letting it charge to VBAT = 1.8 V. An oscilloscope was used to capture the VBAT vs Time characteristics

and quickly saw to my dismay there was a fairly big difference between the measured value and the rated value. Some were as high as 35% in difference thus there doubts and other methods of measuring the capcitors were explored.

To mimic the situation these capacitors were actually going to be used I used the test setup seen in Fig. 1.5. A 140 µA current source with a voltage limit of 1.8 V was used to charge the capacitors. Then, the oscilloscope was used to measure VBAT vs Time. From the the slope, $\frac{\mathrm{dV}}{\mathrm{d}t}$, the effective capacitance was calculated. As seen in Fig. 1.8 , 1.7, 1.6, the capacitances are nowhere near the actual value that they were rated for. The general trend is the effective capacitance decreases as VBAT approaches 1.8 V. The max capacitance appears to be close to 0.5 V for all the plots. While the min capacitance is near 1.8 V.

What should be done? The right answer depends on the application. If the application requires the capacitance to not be dependent on voltage and does not have size limits an electrolytic or tantalum capacitor should be far more reliable. However, if the smallest capacitor is a design requirement understanding the DC bias conditions and AC signals is important to calculating the effective capacitance. In most of the applications used in this dissertation VBAT is held at 1.8 V with periodic drops of ΔVBAT = 165mV. This meant the worst case effective capacitances: 50 µF, 27 µF, and 8 µF for 100 µF, 47 µF, and 22 µF, had to be used. Table 1.2 summarizes what the capacitors were rated and how it compares to the LCR and current source measurements with the highest difference being 63% for the 22 µF. The results here are seen in other places such as a data sheet from Murata Manufacturing [55]. For a 50 V rated capacitor you can see drops in capacitance as high as 50% if the DC voltage is close to the max rating. For an AC voltage, you have a similar situations with capaciances close to -30% or 20% if ac voltage is 0 V and 2 V. While it is helpful that these issues are documented it is still unlcear why exactly this occurs.

As discussed in this article [86], multi layer ceramic capacitors (MLCC)s are the primary choice for small electronics but not without compromises in effective capacitance due to DC bias. The crystal structure of the ceramic material is polarized due to the asymmetry. The spontaneous polarization can be reversed with an electric field but this becomes challenging

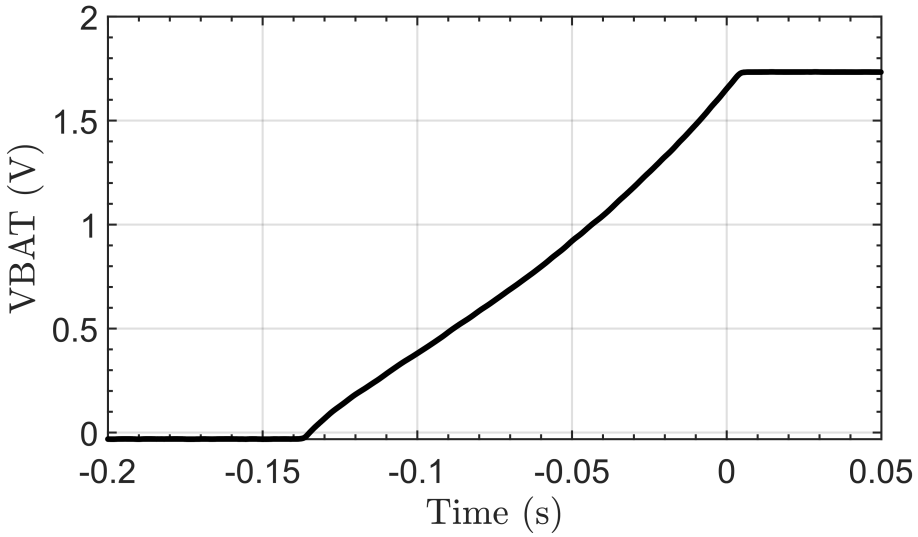

(a) VBAT vs Time for an 0402 22 µF capacitor

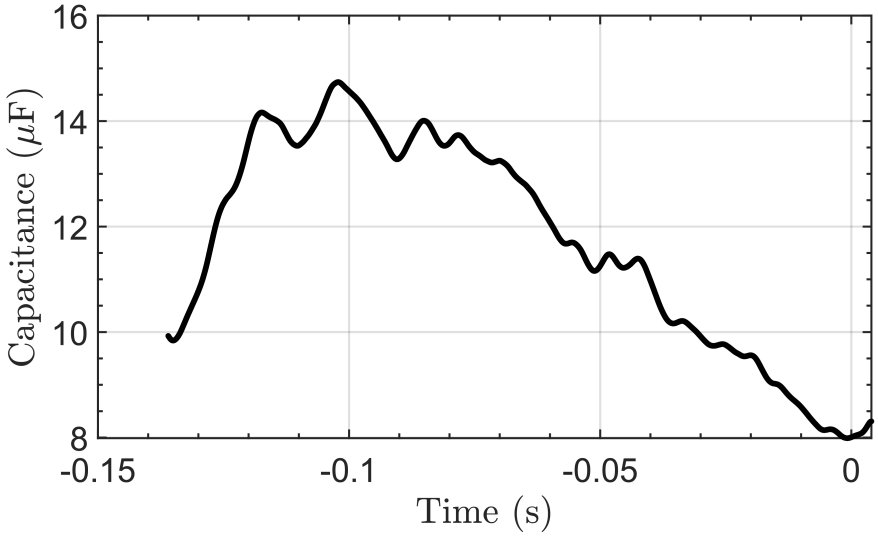

(b) Effective Capacitance vs Time for an 0402 22 µF capacitor

Figure 1.6: Measuring the effective capacitance of an 0402 22 µF capacitor by applying a 140 µA current source and letting it charge to VBAT = 1.8 V

if the capacitor is under a DC bias. Since the relative dielectric constant depends on the reversal of spontaneous polarization per unit volume the effective capacitance is lower.

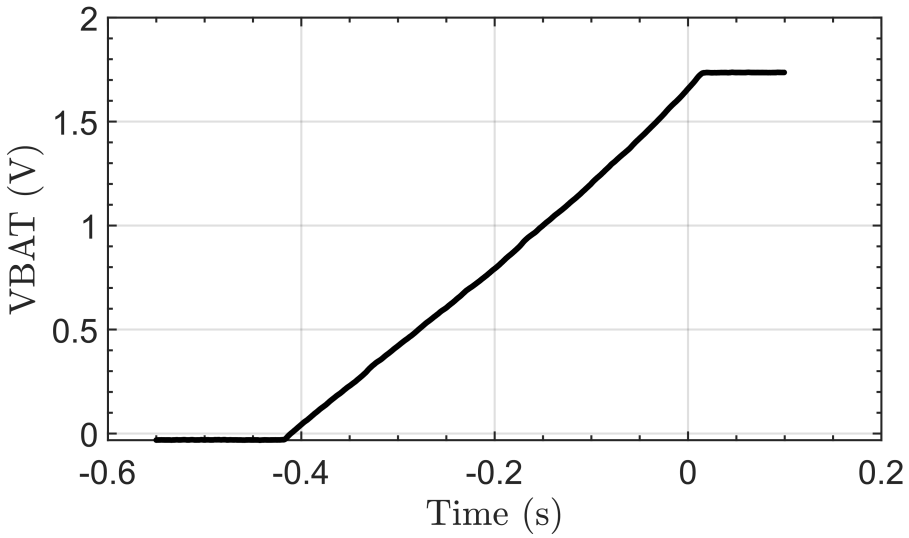

(a) VBAT vs Time for 0603 47 µF capacitor

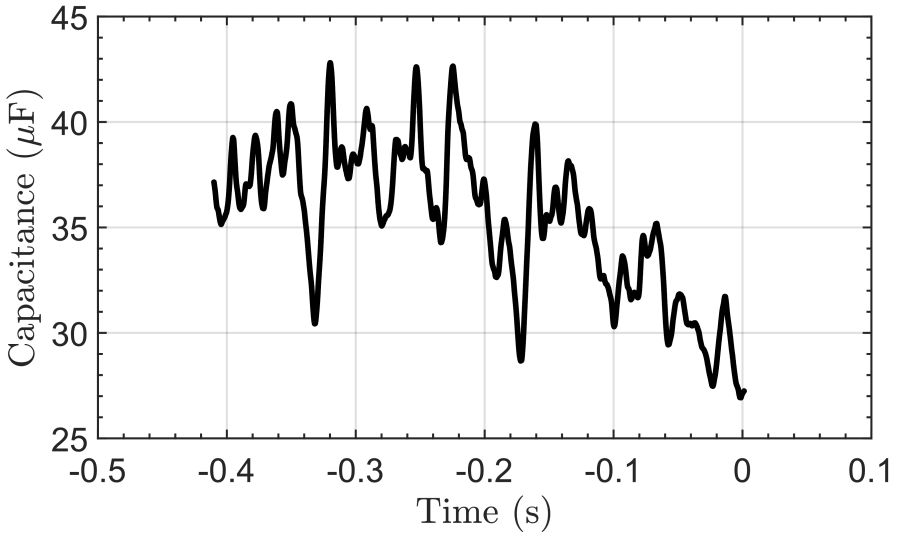

(b) Effective Capacitance vs Time for an 0603 47 µF capacitor

Figure 1.7: Measuring the effective capacitance of an 0603 47 µF capacitor by applying a 140 µA current source and letting it charge to VBAT = 1.8 V

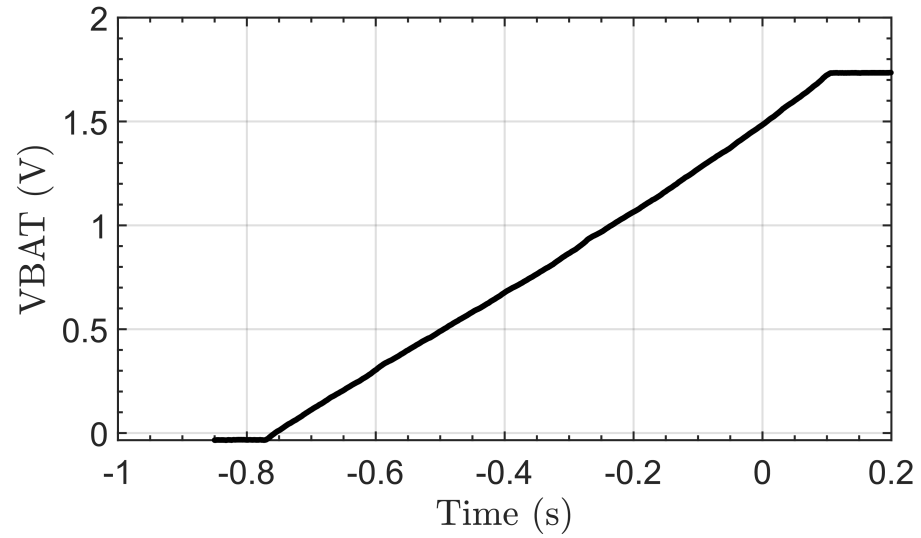

(a) VBAT vs Time for an 0805 100 µF capacitor

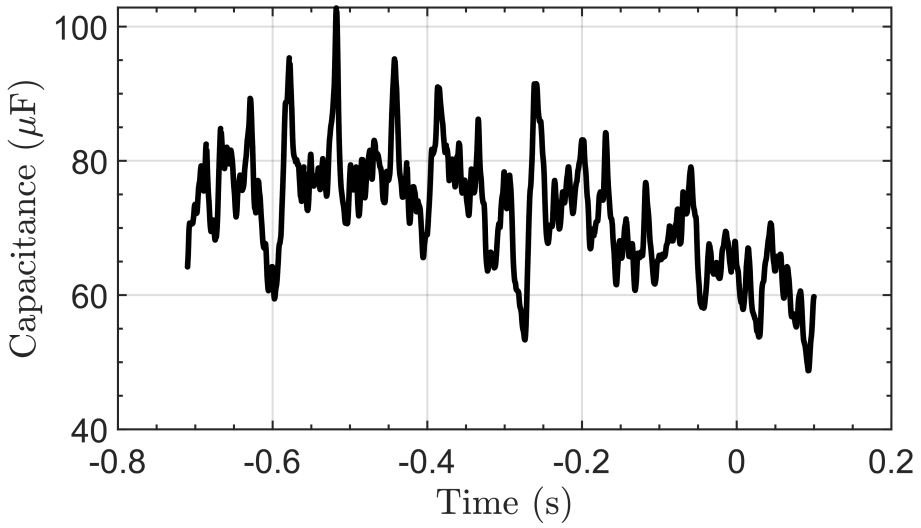

(b) Effective Capacitance vs Time for an 0805 100 µF capacitor

Figure 1.8: Measuring the effective capacitance of an 0805 100 µF capacitor by applying a 140 µA current source and letting it charge to VBAT = 1.8 V

Table 1.2: Capacitance Comparison

Capacitor	LCR	Current Source Linear Regression	Current Source Min Value	Percentage Difference
100 µF 0805 2.5 V	64.5 µF	69.5 µF	50 µF	50%
47 µF 0603 4 V	38 µF	34.1 µF	27 µF	42%
22 µF 0402 6.3 V	16.5 µF	11 µF	8 µF	63%

Lithium Ion Batteries

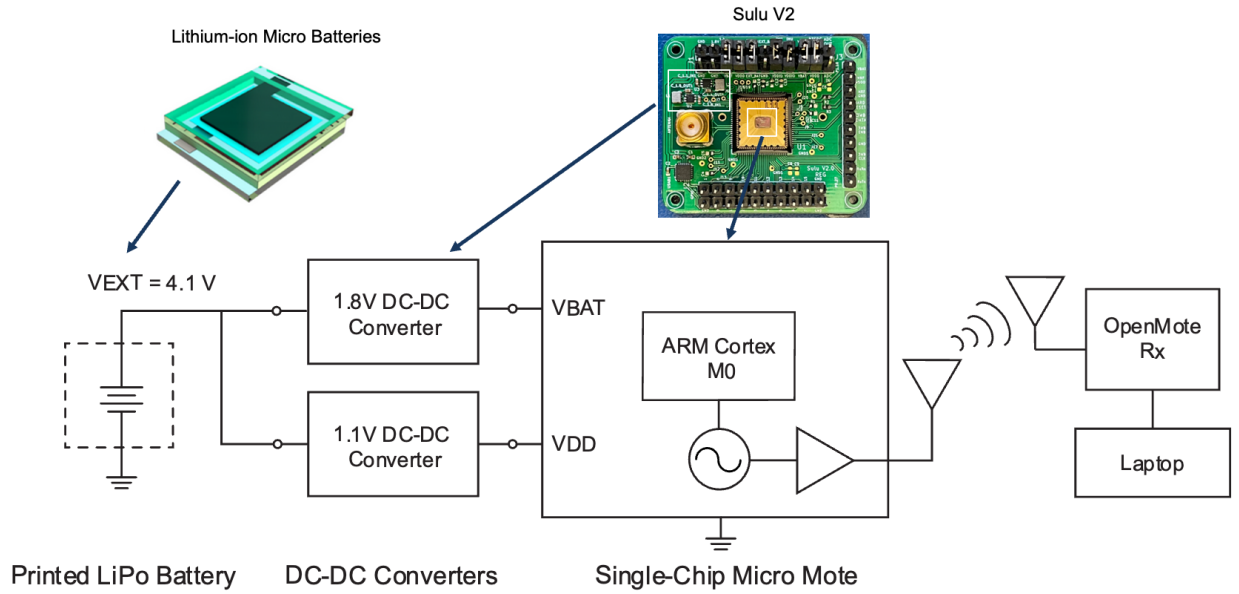

Figure 1.9: The test setup for the lithium-ion batteries. From left to right, the lithium-ion batteries, the DC-to-DC converters, and SCµM. Packets were sent at a 1 Hz rate to an OpenMote

Table 1.3: These are the expected battery life specs. 13.6 hours is what was actually measured while the last two theoretical numbers are based on the assumption a 1 µA sleep current is achieved with future iterations.

Case	Battery Life
Measured TX 1 Hz	13.6 h
Theoretical w/ 1 µA sleep current	128 d
Theoretical w/ TX 1 Hz	13 d

The vision for future low-power systems is to be able to print batteries directly onto SCµM. Ideally, the battery and antenna would be directly printed on a wafer, have the die cut and have the wireless sensors ready. To reach this goal batteries were created by Anju Toor, who was a post doc in Professor Ana Arias lab at the time and currently is a Professor at Georgia Tech Institute of Technology.

The battery itself is fairly small at a mere 5x5 mm and has a capacity of greater than 1.5 mAh some as high as 1.64 mAh h. The energy density, 23.6 mWh cm^{-2}, and areal capacities, 6.4 mAh cm^{-2}, are unmatched by 11 other similar works as discussed in [91]. This was achieved by using a thick 184 µm graphite anode layer and ~205 µm lithium cobalt oxide (LCO) cathode layer. In comparison, typical lithium-ion batteries use 65 µm for the graphite

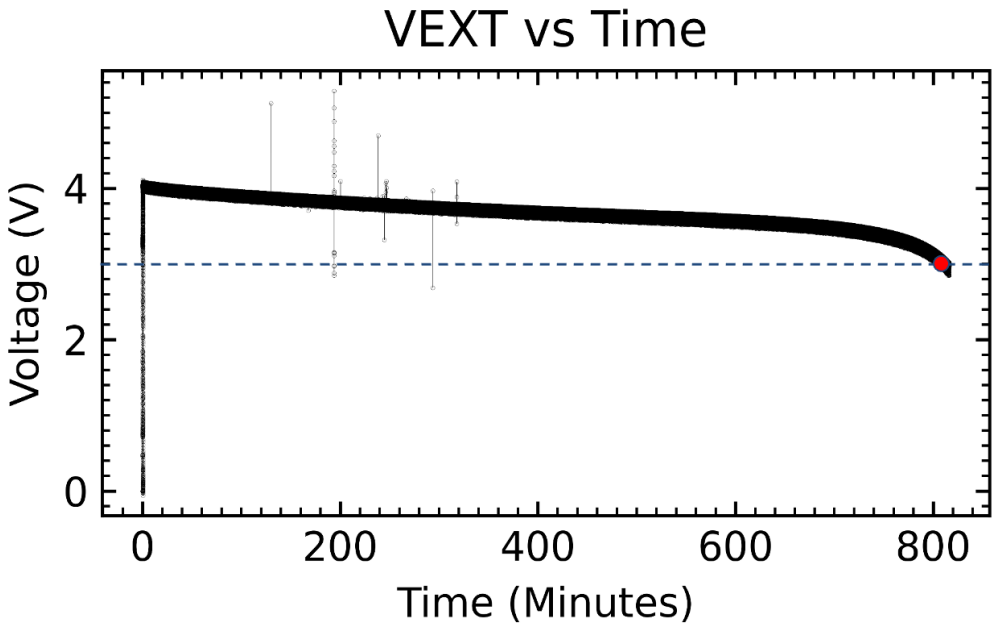

(a) The output voltage of the lithium-ion battery, VEXT, vs time. The red dot indicates the voltage has hit 3 V giving a battery life of 13.6 h

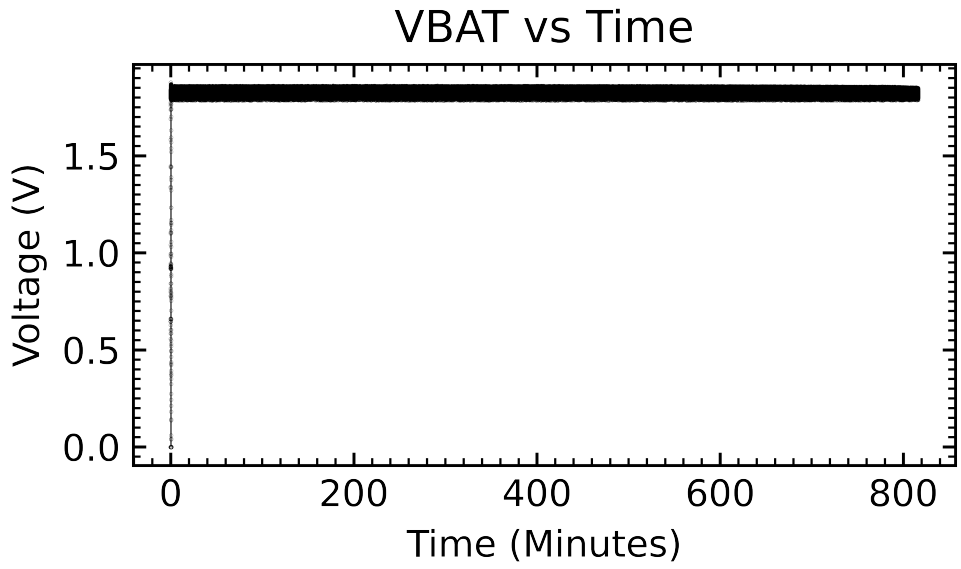

(b) The voltage output of the 1.8 V DC-to-DC converter, VBAT, vs time.

Figure 1.10: Voltages of the lithium-ion battery and output of the 1.8 V DC-to-DC converter vs time.

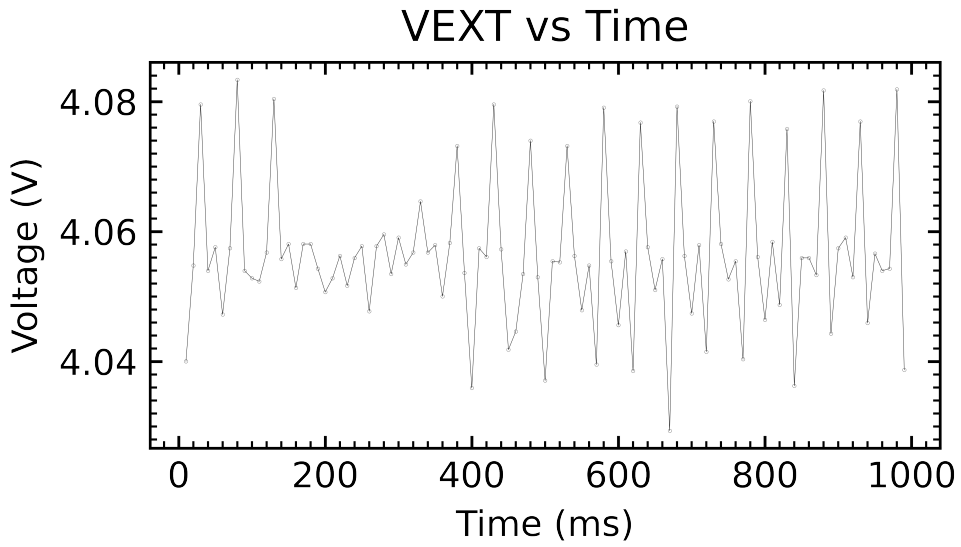

(a) Zoomed in view of VEXT. Since DC-to-DC converters were used a voltage ripple of ~56 mV is present.

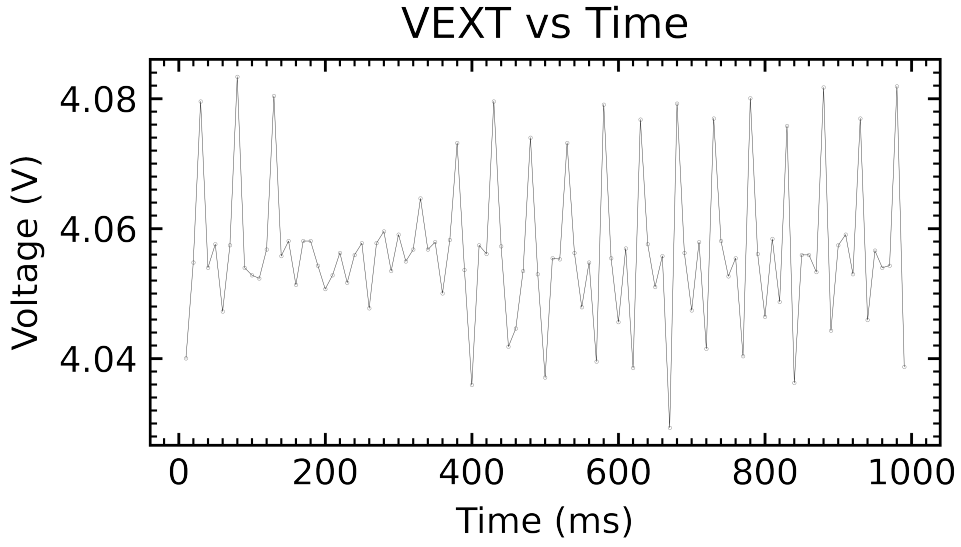

(b) Zoomed in view of VBAT. A voltage ripple of ~62 mV is present which causes challenges keeping crystal-free radio's tuned to the correct frequency.

Figure 1.11: A view of voltage ripples on VBAT and VEXT across time.

layer, and 75 µF for the LCO. As a result, the battery's energy density outperform similar batteries but suffers from a higher series resistance in the order of ~100 Ω. During high-current draw the high resistance causes the voltage to drop. Repeated events high-current

events deteriorates the battery since it can cause chemical instability, and capacity loss.

To power SCµM from these batteries, the Ablic S-85S1AB18-I6T1U and S-85S1AB11-I6T1U DC-to-DC converters with an efficiency of 90.5% efficiency were used to covert from 4.2 V to 1.8 V and 1.1 V, respectively. The custom-designed SULU V2 board, a bare minimum SCµM prototyping board, included the DC-to-DC converters making it easy to accept lithium-ion batteries as shown in Fig. 1.9. For more details on the design refer to the GitHub Repo found here `https://github.com/PisterLab/scum-dev-board/tree/master/sulu-reg`.

In our tests, 10B packets were transmitted every second to an OpenMote (Fig. 1.9). The results seen in Fig. 1.10a, indicate a battery life of 13.6 h marked by the red dot crossing the 3 V threshold. Presently, SCµM is capable of a sleep current equal to ~150-200 µA depending on VBAT. If SCµM were to achieve a sleep current of 1 µA, the projected theoretical battery life would be close to 13 days while transmitting 10B packets at 1 Hz and 128 days while sleeping at 1 Hz.

However, there are concerns that need to be addressed. A zoomed view of VBAT and VEXT reveals ripples that are ~62 mV and ~52 mV, respectively. A probable cause for these ripples is the DC-to-DC converter's switching frequency. Typically, it's close to $f_s = 1\text{MHz}$ using pulse width modulation but in low current mode it uses pulse frequency modulation causing $f_s \ll 1\text{MHz}$. These ripples pose significant challenges for the frequency stability of crystal-free radios and meeting the 40 ppm requirements of 805.15.4 since a mere 15 mV (Fig. 2.16) will kick you out of the channel. Sec. 2.3 and 5.2 covers how software and hardware could address this issue, respectively.

1.3 Energy Harvesting: Small Solar Cells & Zappy2

Table 1.4: Energy Density Specs for Zappy2's solar cells

Solar Cell	Voltage (V)	Current (µA)	Power (µW)	Power Density ($\mu W\,cm^{-2}$)
VBAT	1.8	280	504	15500
VDDIO	3.5	16	56	23000
VDDHV	119	2.4	285	14500

With the recent advancements in low-power technology, the possibility of battery-free wireless sensors has emerged. The solution lies in harnessing the energy from the environment these sensors are placed in. The four main forms of ambient energy sources include mechanical, thermal, radiant and biochemical. Solar energy, a radiant source, provides the best energy density, as high as $100\,000\,\mu W\,cm^{-1}$, in outdoor environments as discussed in [5]. Even in indoor environments solar energy provides among the highest energy density compared to other forms of energy harvesting such as vibration, thermal gradients and RF harvesting. Each energy harvesting techniques, however, suffer limitations. For example, light renders solar useless and the same goes for a lack of vibrations or thermal gradients

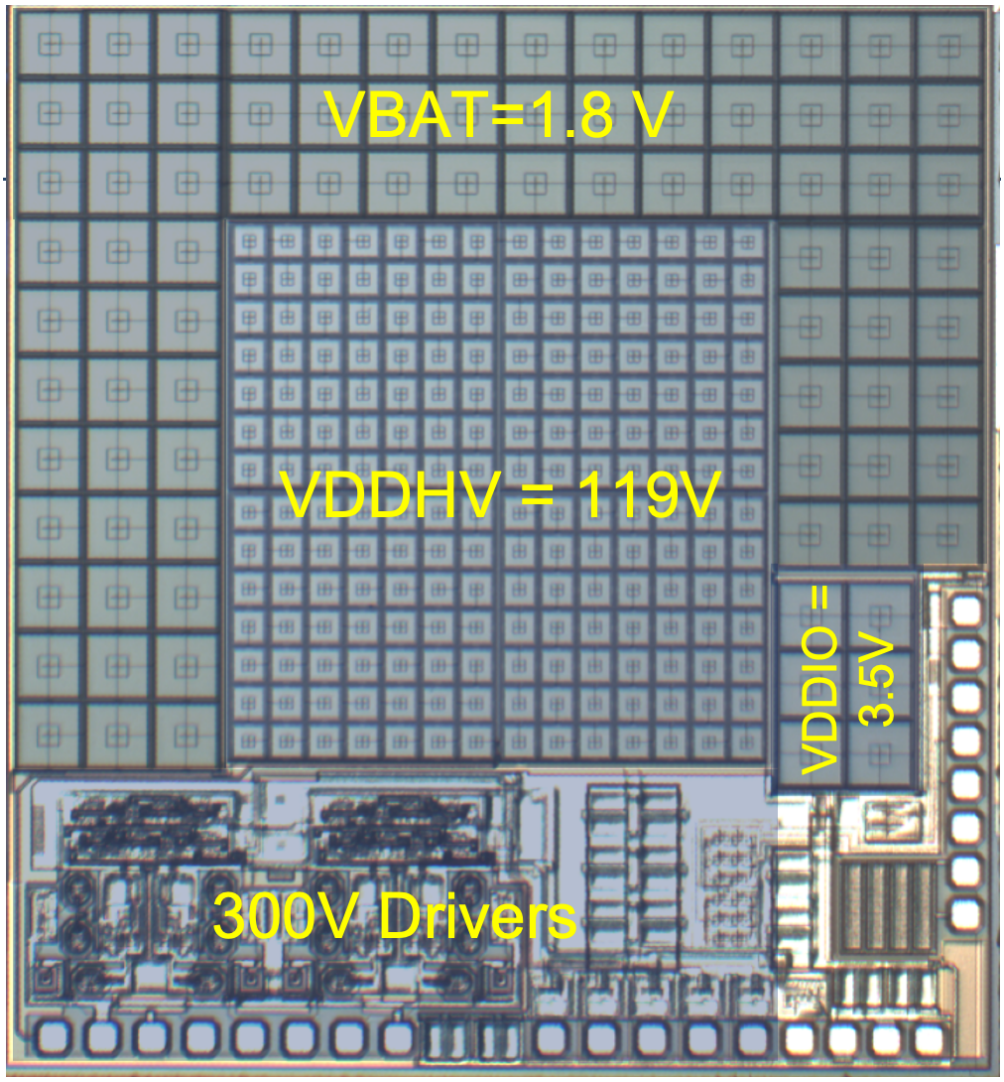

Figure 1.12: Zappy2 chip with labels for the 3 solar cells, VDDHV, VDDIO, VBAT and the 300 V level shifters

in other forms of energy harvesting. The reality is that energy storage is required to bridge the gaps of available ambient energy sources, leading to exploring lithium-ion printed micro batteries and selecting solar energy for energy harvesting due to it's high energy density.

Rentmeister et al. designed a $3.26 \times 3.5\,\mathrm{mm}^2$ solar cell CMOS chip, referred to as Zappy2 Fig. 1.12, containing 4 high voltage (HV) buffers and three solar cell arrays [71]. Using a 650 V trench-isolated CMOS process, Zappy2 contains hundreds of PV cells were fabricated on the same chip. These cell are configured as follows:

- 3 PV cells in series yielding the 1.8 V VBAT to power the SCµM digital system
- 6 PV cells in series for 3.5 V VDDIO necessary for the SCµM GPIOs to drive the input

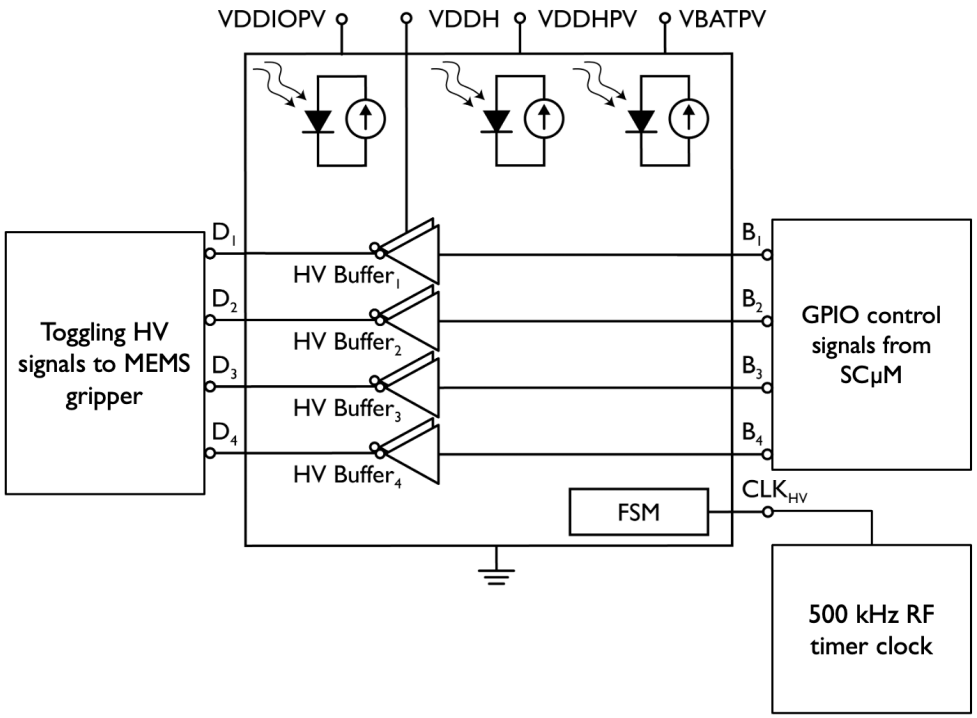

Figure 1.13: Zappy2 schematic. The chip consist of three solar cells, 119 V VDDHV, 3.5 V VDDIO, and 1.8 V VBAT. In addition, four 3.3 V to 300 V level shifters were included to drive MEMS inchworm motors. The HV level shifters are controlled a finite state machine.

to the high-voltage level shifters

- 196 PV cells in series generate 119 V VDDHV to supply the four high voltage (HV) level shifters used to drive the high voltage MEMS inchworm motors

For low-voltage actuators that require tens of mW, SCμM's GPIOs can drive them directly. However, for MEMS inchworm motors the voltage levels required for actuation are higher than 60 V. The 4 HV level shifters on Zappy2 on solar power can drive MEMS motors as discussed in Sec. 3.1 but they have a separate pin from the VDDH PV pin. This allows the HV level shifters to convert a 3.3 V signal to as high as 300 V with an external power supply. If needed, with a chip redesign the process could support a design up to 650 V. A built-in finite state machine (FSM), hardwired to VDDIO, controls the HV drivers using the 500 kHz RF clock. Further details about the circuit design are detailed in [71]

There are two critical lessons learned while working with Zappy2:

- The FSM needs to operate significantly faster than input of the HV level shifter otherwise the level shifter. Otherwise, they might fail to output a level shifted signal or the waveform will be corrupted.

- The HV buffers need to be shielded from the light to operate properly such as not switching or increasing the leakage current significantly.A small piece of electrical tape proved effective at shielding as seen in Fig. 3.1

For this dissertation, Zappy2 was powered under an irradiation of $200\,\mathrm{mW\,cm^{-2}}$ $I_{\mathrm{sc}} =$ with $560\,\mu\mathrm{A}$ because of the high current draw from MEMS devices and SCµM during transmission. Section 2.1 discusses how to model Zappy2, alongside a capacitor and SCµM during current draws bigger than what Zappy2 could provide.

Chapter 2

Calibration Techniques for Crystal-Free Radios

Crystal-Free radios aim to reduce the amount of components necessary to have a fully functioning wireless node. As result Crystal-Free radios tend to be low power, smaller in size and lower in weight. However, these radios are sensitive to voltage and temperature variations.

Since SCµM is a crystal-free radio the on-chip clocks must be calibrated to compensate for temperature and voltage fluctuations. The temperature coefficients of the 2 MHz and the 2.4 GHz oscillators are 160 ppm/°C [99] and −40 ppm/°C [52], respectively. Prior work, demonstrated clock calibration through optical [97] and RF packets[88, 89]. Even with an initial calibration the 2.4 GHz local oscillator (LO) was still susceptible to temperature variations which was addressed in [100, 63, 15]. Most recently [61] demonstrated frequency compensation while transmitting packets and facing voltage variations.

This chapter is broken up into three main parts:

2.1 Discusses the system and how SCµM is modeled while solar-powered.

2.2 Discusses how to calibrate a solar-powered SCµM for temperature variations

2.3 Discusses how to compensate a solar-powered SCµM to increase the amount of data transmitted from 10B to 125B

2.1 A Solar-Powered SCµM System and Model

Since the goal for the lab is to miniaturize the electronics for microrobotic applications, the least amount of components were used. Section 2.2 and 2.3 use the same three components SCµM (Sec. 1.1), Zappy2 (Sec. 1.3) and an 0805 capacitor (Sec. 1.2). As can be seen in Fig. 2.1, these three components are smaller than a quarter and can be further miniaturized as shown in Sections 3.3, 3.2 and 3.4, for penny-sized microrobots, tracking hornets, and nail-sized human-computer interaction devices.

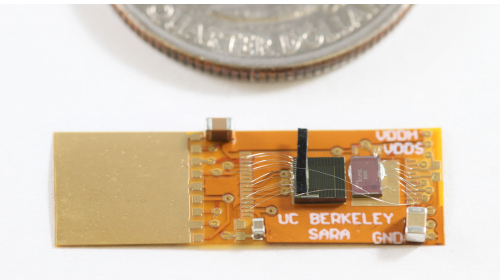

Figure 2.1: Pad for MEMS integration, HV buffer & solar cells chip, and SCµM (left to right). Only the capacitor on the bottom right is used while the remaining capacitors were used for MEMS integration discussed in Section 3.1.

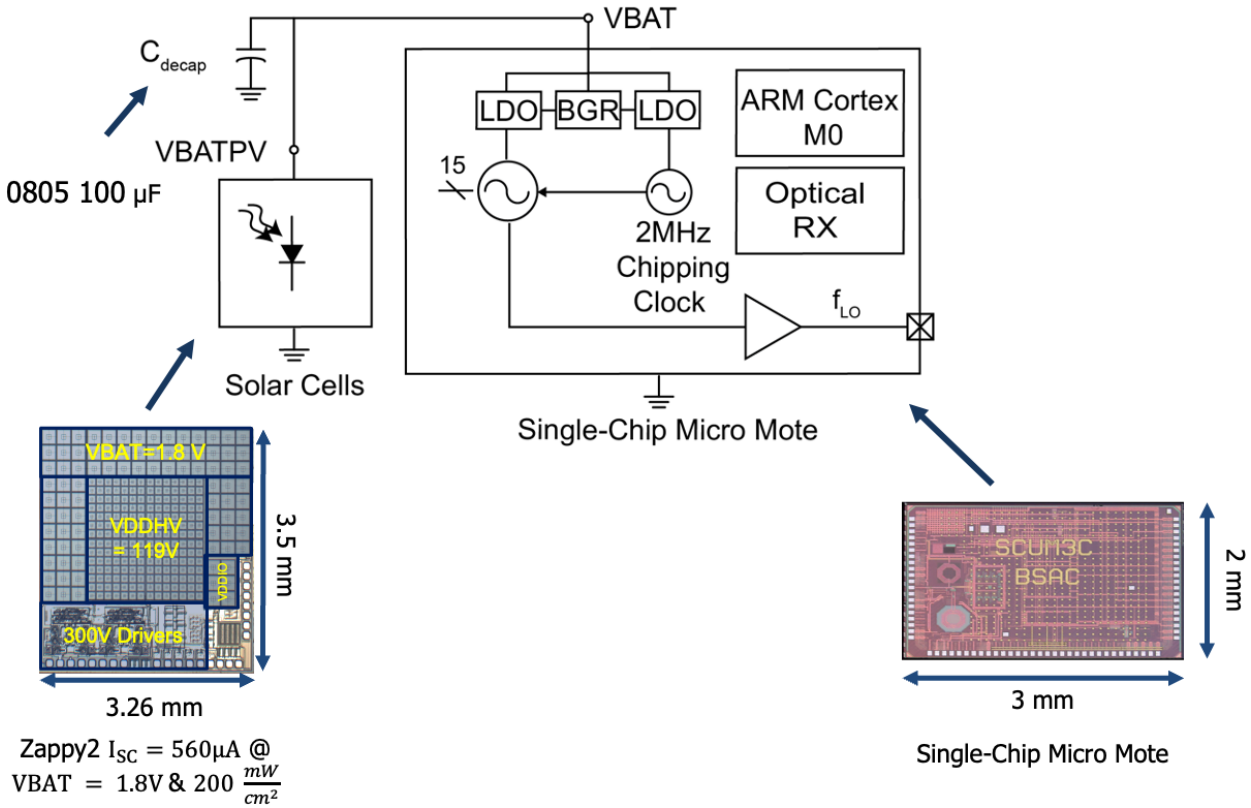

Figure 2.2: SCµM has an ARM Cortex M0, an optical receiver, a 2.4 GHz oscillator, a 2 MHz chipping clock, a bandgap reference, and separate LDOs for the oscillators. The local oscillator can be tuned by a 15-bit capacitive DAC that is divided into 3 5-bit capacitor banks, coarse, mid and fine. SCµM is being powered from a solar cell under an irradiation of 200 mW cm^{-2} which provides a $I_{sc} = 560\,\mu A$. A $C_{decap} = 100\,\mu F$ was used.

To get a sense of what is going on let's discuss the system seen in Fig 2.2. Zappy2, contains high voltage (HV) buffers and three solar cell arrays [71]. For this chapter, only

the VBATPV = 1.8V solar cell array is used to power SCµM under an irradiation of $200\,\mathrm{mW\,cm^{-2}}$ which provides a short circuit current $I_{\mathrm{sc}} = 560\,\mu\mathrm{A}$. Zappy2 was used in a similar capacity in [62] while transmitting and receiving 805.15.4 packets and driving high voltage MEMS gap closing actuators. As discussed in [62, 63] while transmitting or receiving a packet SCµM draws significantly higher current than what Zappy2 can deliver under an irradiation of $200\,\mathrm{mW\,cm^{-2}}$. For this application, an 0805 capacitor $C_{\mathrm{decap}} = 100\mu\mathrm{F}$ was used to provide the extra charge needed during those high current transients. Otherwise, SCµM loses its boot state if VBAT drops below 1.3 V. While adding the biggest capacitor until SCµM can transmit and receive packets is an option the limitations are unclear. Such as how long and often the radio can be turned on and how small the capacitor can be to miniaturize the whole system.

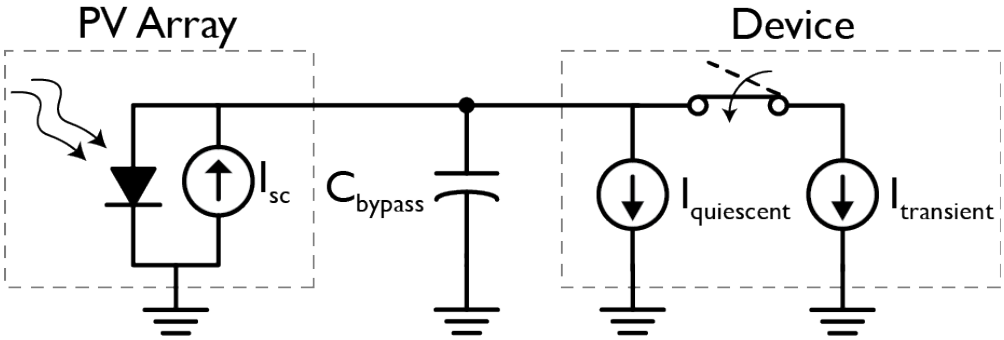

Figure 2.3: Model for a solar-powered SCµM. Typically, $I_{\mathrm{quiescent}}$=380 µA and $I_{\mathrm{transient}}$=1220 µA during radio operation.

Therefore, the model in Fig. 2.3 was created to have a better sense of all three components. SCµM is modeled by Eq. 2.1 which consists of $I_{\mathrm{quiescent}}$, the current drawn while idle, I_{sleep}, the current drawn in low power mode, and $I_{\mathrm{transient}}$, the additional current required to transmit or receive a packet. Typically, I_{sleep}=210 µA, $I_{\mathrm{quiescent}}$=380 µA, and $I_{\mathrm{transient}}$=1220 µA during radio operation.

$$I_{\mathrm{VBAT}}(V) = \begin{cases} I_{\mathrm{sleep}}(V) & \text{low power mode} \\ I_{\mathrm{quiescent}}(V) & \text{idle} \\ I_{\mathrm{quiescent}}(V)+I_{\mathrm{transient}}(V) & \text{TX or RX} \end{cases} \tag{2.1}$$

The ideal model for a solar cell was used for Zappy2. Thus, the current provided by Zappy2 is described by the Shockley solar cell equation (Eq. 2.2) and $I_{\mathrm{ph}} = I_{\mathrm{sc}}$ [56]. The 0805 capacitor's IV characteristics are described by Eq. 2.3. Combining all of these equations results in Eq. 2.4. To simplify things it is assumed that $I_{\mathrm{transient}}$ and $I_{\mathrm{quiescent}}$ are constant for small changes of VBAT and $I_{\mathrm{sc}} \gg I_o\left(e^{\frac{qV}{k_B T}}-1\right)$. Note that I_{VBAT} does a vary slightly with voltage as can been in the I_{VBAT} vs Time plots for TX (Fig. 2.4) and RX (Fig. 3.4). The simplification leads to Eq. 2.5 which allows us to solve for VBAT.

$$I_{\text{solar}} = I_{\text{ph}} - I_{\text{o}}\left(e^{\frac{qV}{k_B T}} - 1\right) \tag{2.2}$$

$$I_{\text{decap}} = C_{\text{decap}}\frac{dV}{dt} \tag{2.3}$$

$$I_{\text{solar}}(\text{V}) = I_{\text{decap}}(t) + I_{\text{VBAT}}(\text{V}) I_{\text{sc}} - I_{\text{o}}\left(e^{\frac{qV}{k_B T}} - 1\right) = C_{\text{decap}}\frac{dV}{dt} + I_{\text{VBAT}}(V) \tag{2.4a}$$

$$I_{\text{sc}} = C_{\text{decap}}\frac{dV}{dt} + I_{\text{VBAT}} \tag{2.5}$$

With this simplification VBAT(t) can be solved for three cases: charging the capacitor, TX or RX cap discharge and idle. Eq. 2.6 can be rewritten to solve for Δt if ΔVBAT is known as shown in Eq. 2.7.

$$\text{VBAT}(t) = \begin{cases} \frac{I_{\text{sc}} - I_{\text{quiescent}}}{C_{\text{decap}}}(t - t_{\text{o}}) + V_{\text{o}} & \text{charging cap} \\ V_{\text{oc}} & \text{idle} \\ \frac{I_{\text{sc}} - I_{\text{quiescent}} - I_{\text{transient}}}{C_{\text{decap}}}(t - t_{\text{o}}) + V_{\text{o}} & \text{TX or RX discharge} \end{cases} \tag{2.6}$$

$$\Delta t = \begin{cases} \frac{C_{\text{decap}}\Delta\text{VBAT}}{I_{\text{sc}} - I_{\text{quiescent}}} & \text{charging cap} \\ \frac{C_{\text{decap}}\Delta\text{VBAT}}{I_{\text{sc}} - I_{\text{quiescent}} - I_{\text{transient}}} & \text{TX or RX discharge} \end{cases} \tag{2.7}$$

2.2 Transmitting Packets and Sensing Temperature on Solar-Powered SCµM

This work is based on [63] and was the first attempt to miniaturize a SCµM based system. By using, SCµM, Zappy2 and a 0805 capacitor the system was reduced in size. However, while solar-powered SCµM's 2.4 GHz oscillator varied a lot with voltage and temperature. The temperature dependence was addressed in this section.

System Operation

For this application, SCµM transmits 802.15.4 packets on channel 11 (2.405 GHz). The 802.15.4 specifications prescribe a frequency error less than ±40 ppm. However, since SCµM's oscillators have a large temperature coefficient, 2 MHz and the 2.4 GHz oscillators are 160 ppm/°C [99] and −40 ppm/°C [52], respectively. Thus, it becomes difficult to transmit 802.15.4-compatible packets over temperature variations. In fact, this becomes even more challenging under solar power, which causes the SCµM's supply voltage to vary during packet transmission. The operational procedure is used to address these problems.

As shown in Figure 2.4, transmitting a packet (Φ_3) requires a lot of power, so we need to charge the VBAT capacitor, C_{decap}, between periods of radio operation. Normally, the CPU clock rate is at 5 MHz ($I_{\text{VBAT}} = 380\mu\text{A}$) ($\Phi_2$,$\Phi_4$), but we decrease it to 78 kHz ($I_{\text{VBAT}} = 210\mu\text{A}$) ($\Phi_1$) to further reduce SCµM's power consumption in a low-power state. Note that Figure 2.4 was measured with a 20 µF VBAT capacitor, but a 100 µF one was used for this experiment to improve packet delivery.

SCµM has been shown to send and receive packets under two suns of illumination with a 20 µF capacitor, but large voltage drops shift radio clock calibration parameters and prevent robust radio operation (Figure 2.4). These voltage drops corrupt the packets and are addressed in Section 2.3. With a $C_{\text{decap}} = 100\mu\text{F}$ and an $I_{\text{sc}} = 560\mu\text{A}$, SCµM can be theoretically powered at I_{VBAT} of 1.6 mA during TX or RX for 54 ms (using Eq. 2.7) before VBAT drops from 1.86 V to the operating minimum of 1.3 V.

Transmitting a packet at 1.6 mA with a duration of 5 ms (Figure 2.4) requires 8 µC of charge. Assuming a constant VBAT voltage, a 560 µA constant current input from the solar cells at 200 mW cm^{-2} irradiation, and a 380 µA idle state between transmissions, the theoretical transmission rate is 30 Hz.

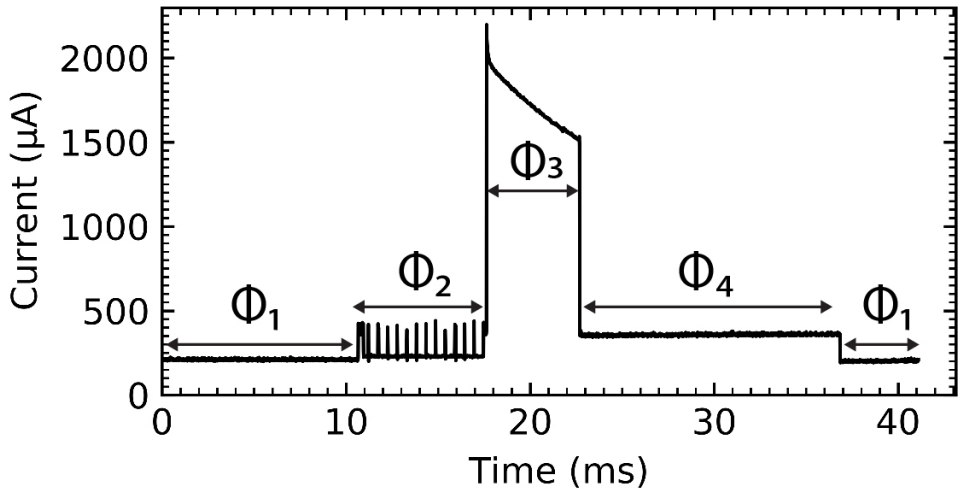

Figure 2.4: I_{VBAT} transient during wireless 802.15.4 transmission (200 mW cm^{-2} irradiation; 20 µF capacitor). Φ_1: Low power mode, Cortex clock = 78kHz, $I_{\text{VBAT}} = 210\mu\text{A}$; Φ_2: printf, Cortex clock = 5MHz; Φ_3: TX, 5MHz; Φ_4: Configuring back to low power, 5MHz, $I_{\text{VBAT}} = 380\mu\text{A}$

Optically Program and Calibrate

At 39 °C, SCµM is connected to an external 1.7 V VBAT source due to the sustained high-power radio-on period required during calibration. Once calibrated, a bright light is turned on to provide 200 mW cm^{-2} of irradiation, and the power source is disconnected to allow

SCµM to operate autonomously, as shown in Figure 2.5. The illumination is focused solely on the solar cells and does not significantly impact the SCµM temperature measurement.

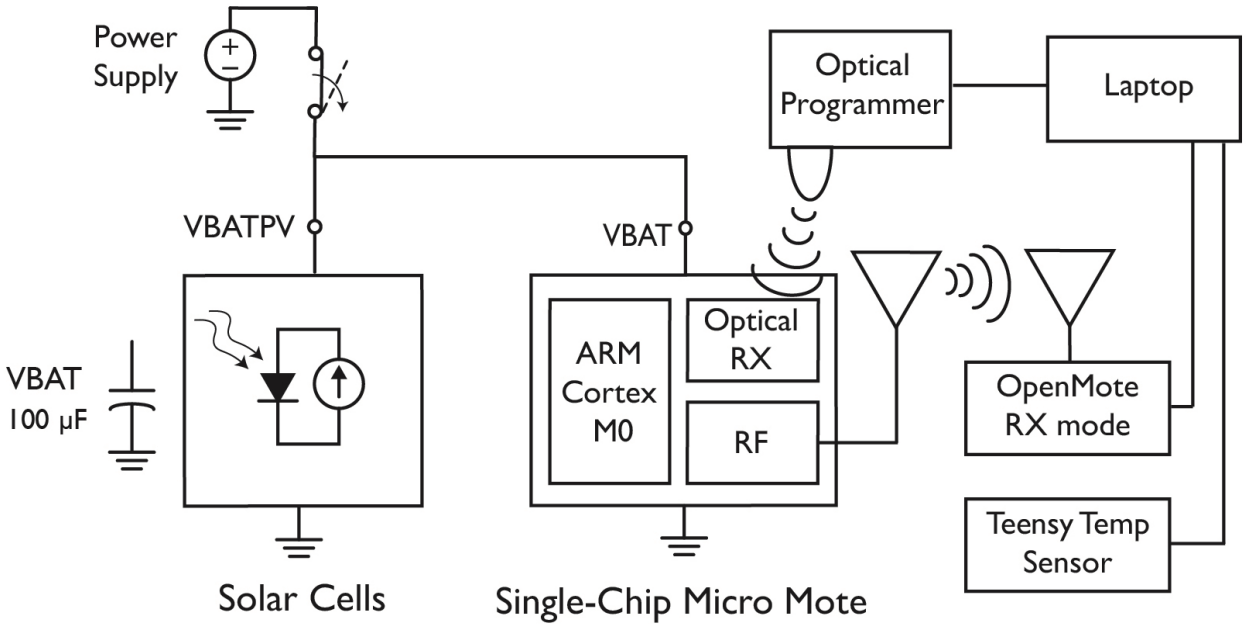

Figure 2.5: System Diagram

Local Oscillator Temperature Compensation

As a wireless temperature sensing node, SCµM needs to transmit packets at various temperatures. To accomplish this, the RF LO needs to be continually compensated over temperature to stay within approximately ±40 ppm of 2.405 GHz. One prior approach used the frequency error in received packets to compensate the LO over temperature [52]. Further work demonstrated this correction on all sixteen 802.15.4 channels between 5 °C and 55 °C [88]. The LO calibration approach used for this experiment is based on a linear relationship between temperature and the ratio of the temperature-dependent on-chip 2 MHz and 32 kHz clocks [100].

Specifically, the first step for the calibration procedure used for this system involves determining which LC fine codes allow for proper radio transmission at which temperature. As we vary the temperature with a hot plate, we continuously sweep through all 32 LC fine codes, measure the ratio of the on-chip 2 MHz and 32 kHz frequency counts over 100 ms, and transmit the ratio in a 14-byte 802.15.4 packet. The coarse and mid codes were predetermined from an earlier calibration.

1. Use a hot plate to control the system temperature to a specific value.
2. Using the RF timer, measure the 2 MHz and 32 kHz clock counts after 100 ms and compute the frequency count ratio.

3. Using the predefined coarse and mid codes and the current fine code (starting at 0), tune the LC and transmit one packet containing the ratio and LC fine code
4. If LC fine code < 31, increment the LC fine code and loop starting at step 2.
5. Reset the LC fine code to 0 and repeat step 1 with a new temperature.

Throughout this process, we record the frequency ratios and LC fine codes of the packets that are successfully received by an OpenMote CC2538 [93]. For each received packet, a reference temperature measurement is taken with a TMP102 digital temperature sensor ($\pm 0.5\,^{\circ}\mathrm{C}$ accuracy) attached to a Teensy 3.6 microcontroller. A linear model is then fit between the clock ratio and the LC fine code as shown in Figure 2.6. For subsequent radio operation, SCµM measures the clock ratio and then use this linear model to determine which LC fine code to transmit at. The viability of this LO temperature compensation is demonstrated by the frequency offsets of the received packets measured by the OpenMote (Figure 2.7).

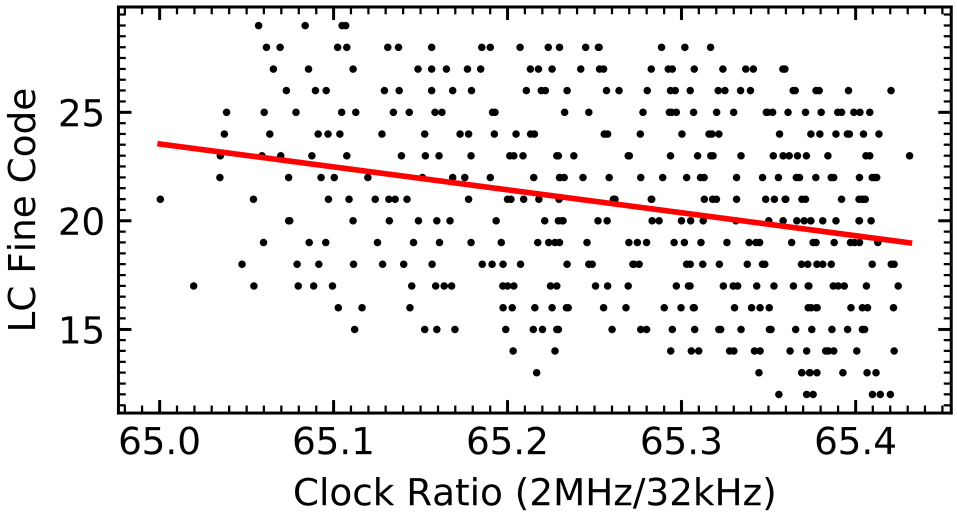

Figure 2.6: LC fine codes of packets received by OpenMote (± 150 ppm tolerance [99]) and SCµM's 2 MHz/32 kHz ratio

Temperature Estimate Calibration

Now that SCµM adjusts its LO frequency to properly transmit across different temperatures, the next step is to calibrate SCµM's temperature estimates [100]. This calibration is accomplished by continually transmitting the 2 MHz and 32 kHz clock ratio to an OpenMote across a temperature range controlled by the hot plate. SCµM continuously corrects its LO frequency using the linear model in Figure 2.6. Meanwhile, temperature measurements are

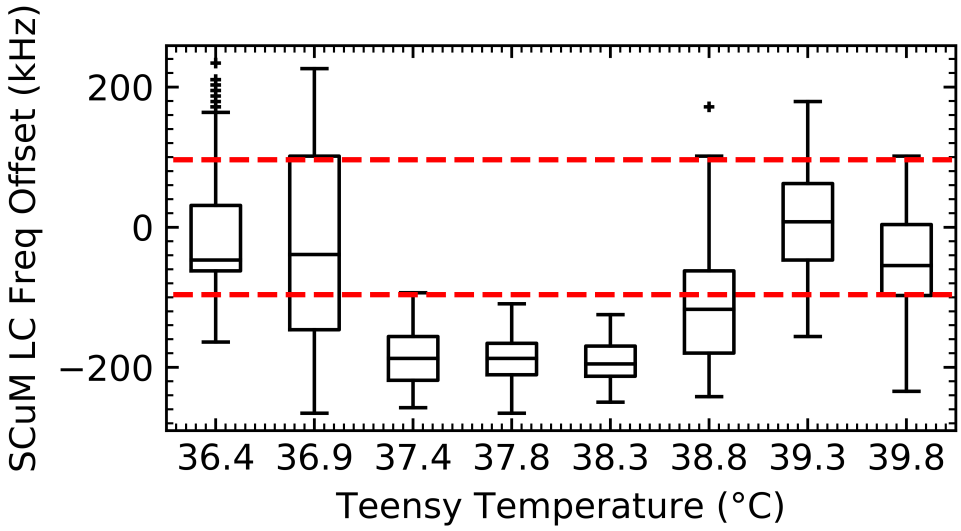

Figure 2.7: SCµM frequency error during LC temperature compensation (Lines show ±40 ppm accuracy for 802.15.4 standard).

taken by a TMP102 digital temperature sensor. A linear regression is calculated between the 2 MHz and 32 kHz clock ratio and the reference temperature measured by the Teensy (Figure 2.8). SCµM then measures the clock ratio and uses this model to produce temperature estimates. This calibration is chip specific.

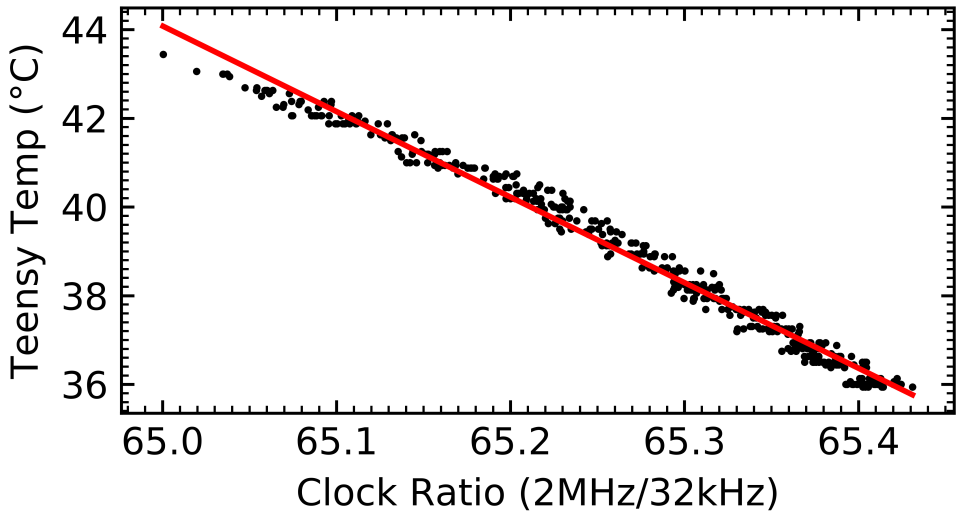

Figure 2.8: SCµM temperature estimate calibration

Temperature Estimate Operation and Accuracy

SCµM is programmed with the following procedure to test the accuracy of the temperature estimates:

1. Measure 2 MHz and 32 kHz clock counts over 100 ms using the RF timer and compute the ratio.
2. Use the model in Figure 2.6 to update the LC fine code.
3. Use the model in Figure 2.8 to estimate the temperature.
4. Decrease the CPU clock rate to 78 kHz for 1 s to charge the VBAT capacitor.
5. Increase the CPU clock up to 5 MHz to transmit a single 10-byte packet containing the temperature estimate. Repeat from step 1.

We show that SCµM can successfully send packets to a ±150 ppm (±360 kHz) tolerant OpenMote CC2538 [99] in a temperature range between 35.5 °C and 40.0 °C. Although some of the packets were outside the ±40 ppm range for 802.15.4 standard as shown in Figure 2.7, the OpenMote was able to attain a 95.8% packet receive rate across this temperature range. This is what we refer to by standards-compatible. The accuracy of SCµM's temperature estimates is shown in Figures 2.9 and 2.10. The standard deviation of the temperature error relative to the Teensy measurement is 0.28 °C.

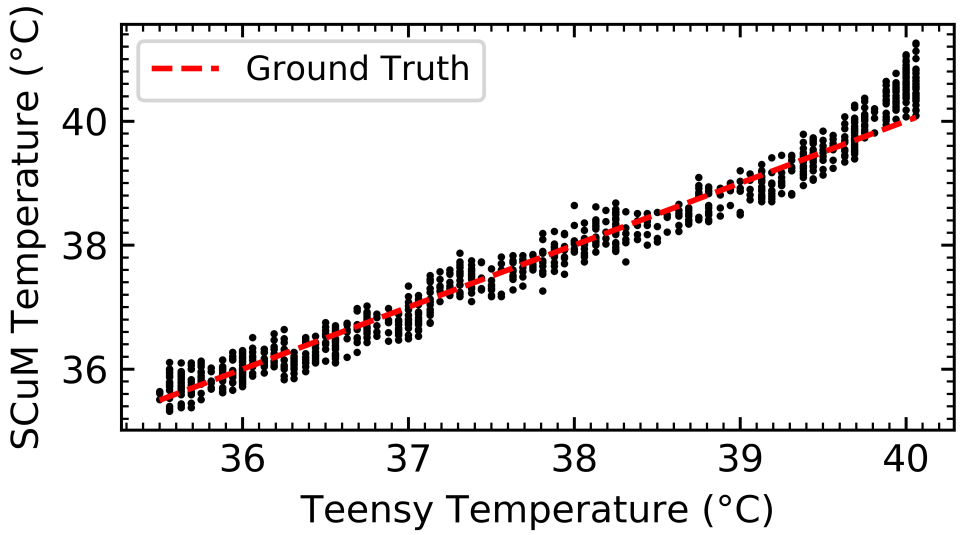

Figure 2.9: SCµM's temperature estimate vs. Teensy TMP102 measured temperature

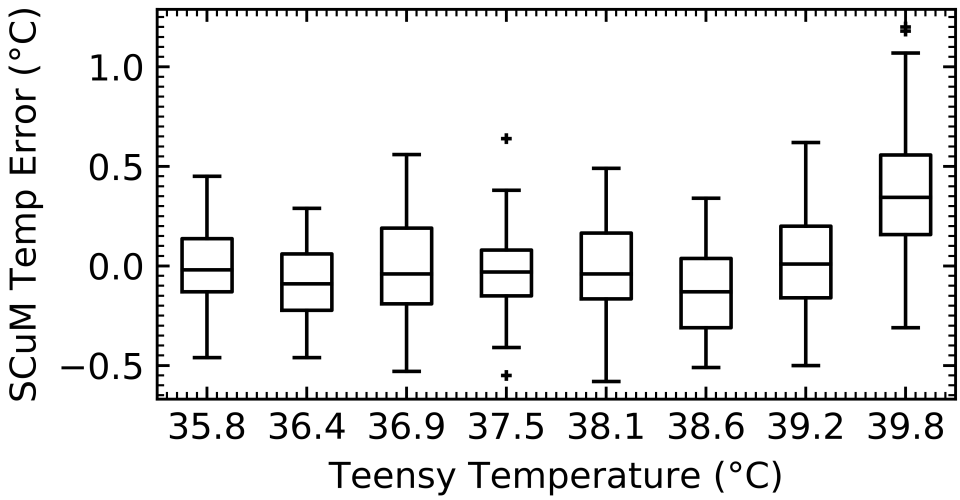

Figure 2.10: SCµM's temperature estimate error

Temperature Compensation Results

An autonomous micro-system that integrates SCµM, Zappy2 and a 100 µF capacitor under 200 mW cm^{-2} irradiation was demonstrated to transmit 802.15.4 packets with temperature estimates between 35.5 °C and 40 °C. Specific applications include fire detection and human temperature measurement. Further improvements could be made with a voltage-compensated clock correction using the on-chip ADC. Further integration with MEMS devices will allow this system to function as an RF-controlled autonomous actuator.

2.3 Compensating Frequency Variation During Transmission for Crystal-Free Radios

For Section 2.2, it was only possible to send 10B 802.15.4 packets by SCµM while solar-powered the remaining data would become corrupted. The hypothesis was because the transmit current was much higher than the current provided by Zappy2's solar cells resulting in f_{LO} being pushed out of the channel frequency. This section goes into why more than 10B can't be transmitted on a solar-powered SCµM, how to compensate the frequency during transmission and how the changes resulted in the full size 125B 802.15.4 packets being transmitted.

The System and Considerations

This section also uses SCµM, Zappy2 and the capacitor as shown in Fig. 2.2. SCµM's two critical oscillators for transmitting and receiving packets are the 2 MHz RC oscillator

chipping clock and the 2.4 GHz LC oscillator referred to as the local oscillator (LO). The LO has a 15-bit capacitive DAC that is made up of three 5-bit capacitor banks, coarse, mid and fine (CMF). The chipping clock and LO both have separate low-dropout voltage regulators (LDO) and an on-chip band gap reference (BGR). Each fine code bit tunes between 90-100 kHz [51, 52].

Why Do Packets Bigger Than 10B Get Corrupted?

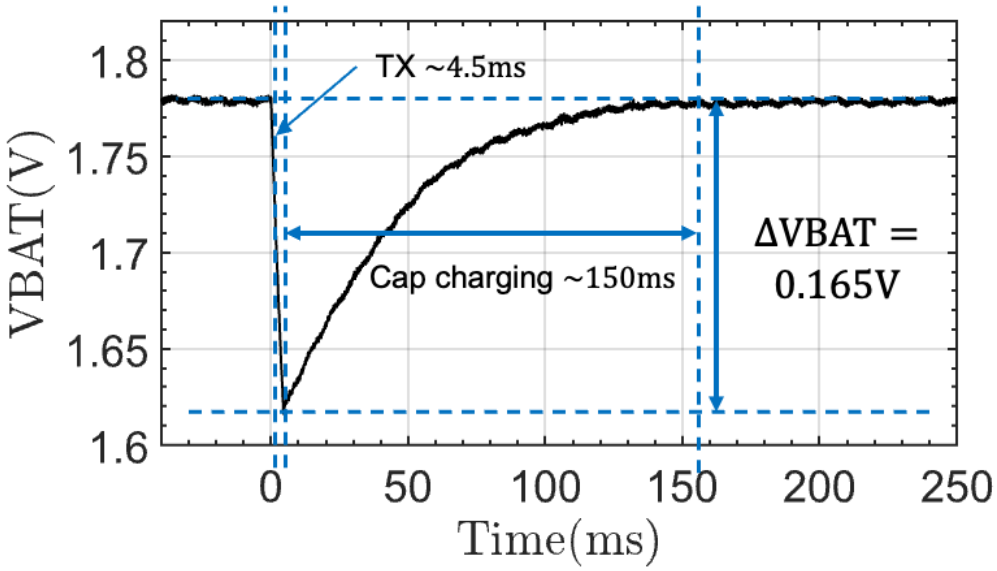

Figure 2.11: VBAT vs Time

A starting point to answer this question is that $I_{\text{VBAT}} > I_{\text{sc}}$ during transmission. To verify that our system is behaving as described in Section 2.1 VBAT vs Time was measured. As seen in Fig. 2.11, ΔVBAT = 165mV while SCµM is transmitting 125B packets. The time to charge C_{decap} to Zappy2's open circuit voltage, V_{oc}, takes $\Delta t_{\text{charge}} = 150\text{ms}$. From this value the maximum packet rate can be derived $f_{\text{packet}} = \frac{1}{\Delta t_{\text{charge}}} = 6\text{Hz}$. As discussed in Sec. 1.2, ceramic capacitors may be rated for 100 µF but their actual capacitance can be less than half of that value. Since $I_{\text{VBAT}} = 1600\mu\text{A}$, ΔVBAT = 165mV and $\Delta t_{\text{transmit}} = 4.5\text{ms}$ are known, C_{decap}'s effective capacitance can be estimated using Eq. 2.8. This gives a $C_{\text{decap}} \approx 38.7\mu\text{F}$ less than half of its 100 µF capacitance rating. The VBAT vs Time plots, Fig. 2.11 and 2.12, agree with the theory in Sec. 2.1. Specifically, during the transmission period shown in Fig. 2.12, VBAT's slope follows the expected linear relationship, $\frac{\Delta\text{VBAT}}{\Delta t} = \frac{I_{\text{VBAT}}}{C_{\text{decap}}}$.

$$C_{\text{decap}} \approx \frac{I_{\text{VBAT}} \Delta t_{\text{transmit}}}{\Delta\text{VBAT}} \tag{2.8}$$

However, how does the change in VBAT and I_{VBAT} relate to f_{LO}? To answer this question the setup in Fig 2.13 was used to mix f_{LO} down by 2.3719 MHz (arbitrarily chosen) to

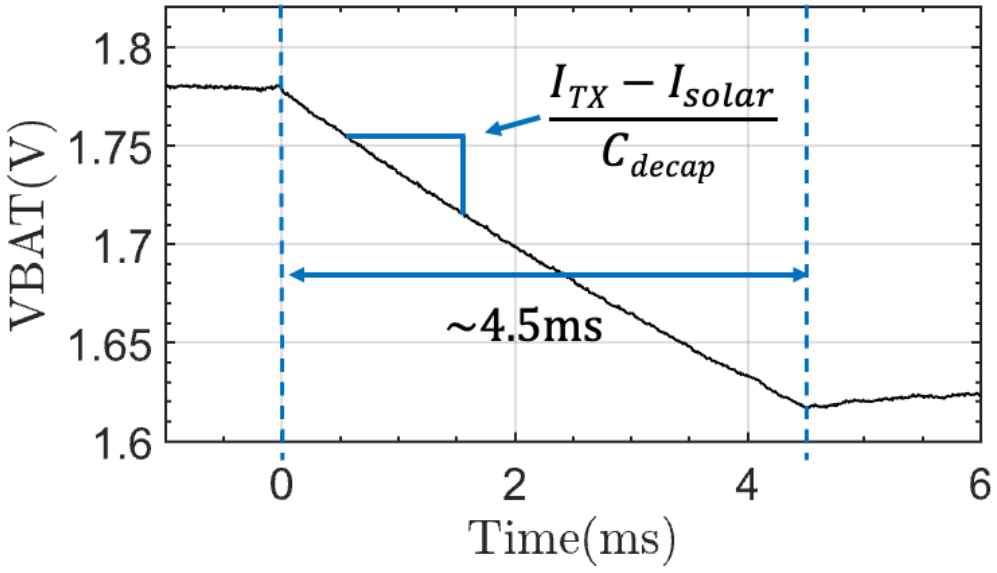

Figure 2.12: VBAT vs Time zoomed into the transmission period. The sharp drop corresponds to the transmission period which is ~4.5 ms. The 100 µF capacitor was charged in ~150 ms. This sets the limit to 6 packets per second.

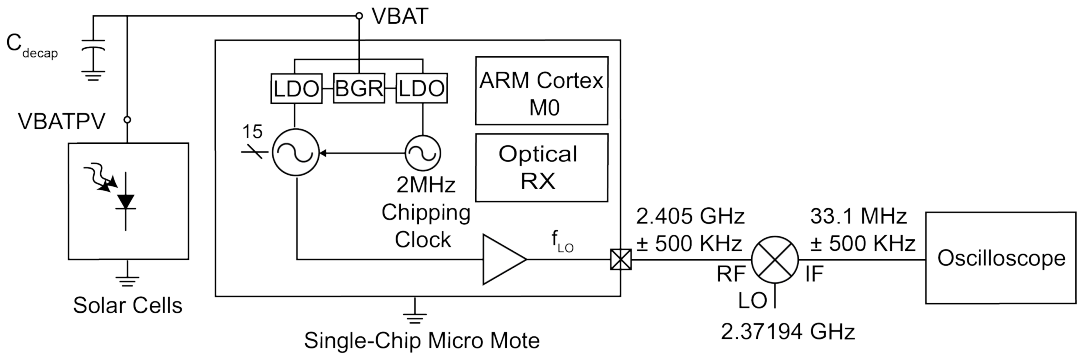

Figure 2.13: f_{LO} was mixed down by 2.3719 MHz to f_{IF} = 33.1MHz. This means that $\Delta f_{\mathrm{LO}} = \Delta f_{\mathrm{IF}}$.

f_{IF} = 33.1MHz. Because mixers are able to shift frequencies, $\Delta f_{\mathrm{LO}} = \Delta f_{\mathrm{IF}}.f_{\mathrm{LO}}$. The data was then collected by an oscilloscope and a matlab script was used create a waterfall plot that resulted in Fig. 2.14. As can be seen from this diagram f_{LO} shifts by about 2.7 MHz while transmitting. Notice the blue line for the 40 ppm 802.15.4 requirement, the yellow line for the 150 ppm requirement for OpenMote's CC2538 and the green line for the desired frequency of 33.1 MHz. From this plot, it can be estimated that within ~100 µs of transmission f_{LO} is outside the 40 ppm requirement and within ~350 µs f_{LO} is outside the 150 ppm requirement. This is the answer to the packet corruption problem.~350 µs is about the amount of time that it takes for SCµM to generate the 4B preamble, the 1B start of frame delimiter (SFD),

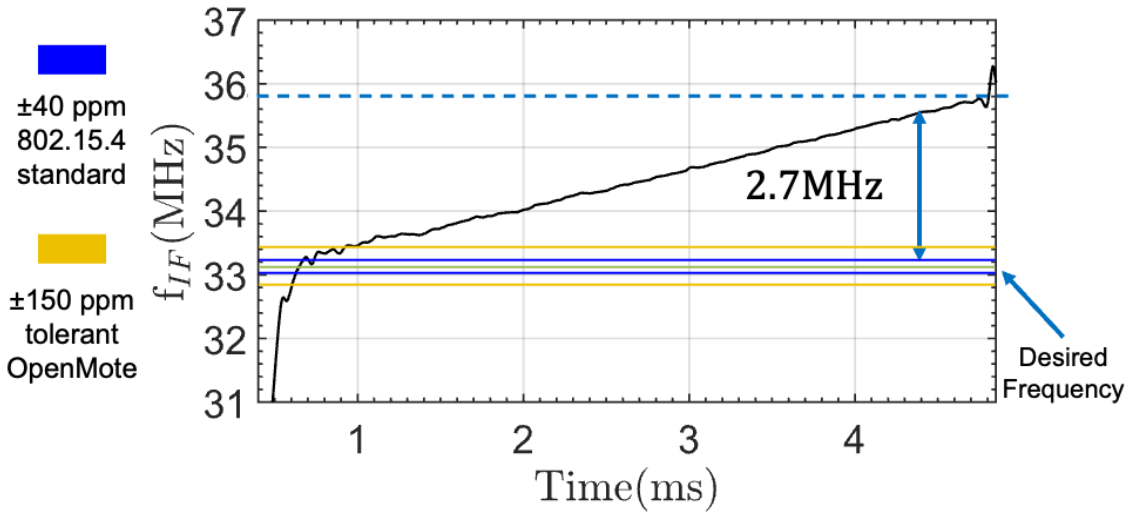

Figure 2.14: f_{IF} vs Time shows that

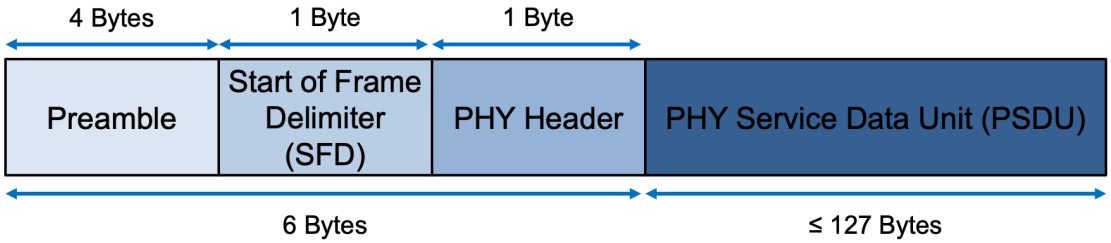

Figure 2.15: The packet structure of a 802.15.4 packet

the 1B PHY Header and 5B of the PSDU. The structure of an 802.15.4 packet is shown in Fig. 2.15 and it takes about 32 µs to send 1B of data. Therefore, any data after ~350 µs is likely to be corrupt since the OpenMote can't demodulate it because f_{LO} is outside of the 150 ppm requirement.

Frequency Shift Compensation

Now that it is clear that f_{LO} is varying with VBAT the following steps were taken to compensate for this $\Delta t_{\mathrm{LO}} = 2.7\mathrm{MHz}$.

1. Optically Program and Calibrate
2. Characterize f_{LO} vs time
3. Create local oscillator DAC codes vs VBAT look up table (LUT)
4. Estimate $\Delta t_{\mathrm{update}}$

Optically Program and Calibrate

SCµM is initially optically programmed and all the on-chip oscillators are calibrated using the methods described in [97, 99]. This includes the 2 MHz chipping clock, the cortex clock and RF timer. SCµM is connected to a 1.8 V VBAT source during this phase since the current draw is higher than what Zappy2 can deliver and is disconnected after. SCµM's LO CMF codes were initially manually calibrated to transmit 802.15.4 packets on channel 11, $f_{\mathrm{LO}} =$ 2.405GHz. Assuming temperature were stable, f_{LO} would stay within the 802.15.4 standard's LO requirement, ±40 ppm, over several several hours and could be updated through the network [52].

Characterize f_{LO} vs time

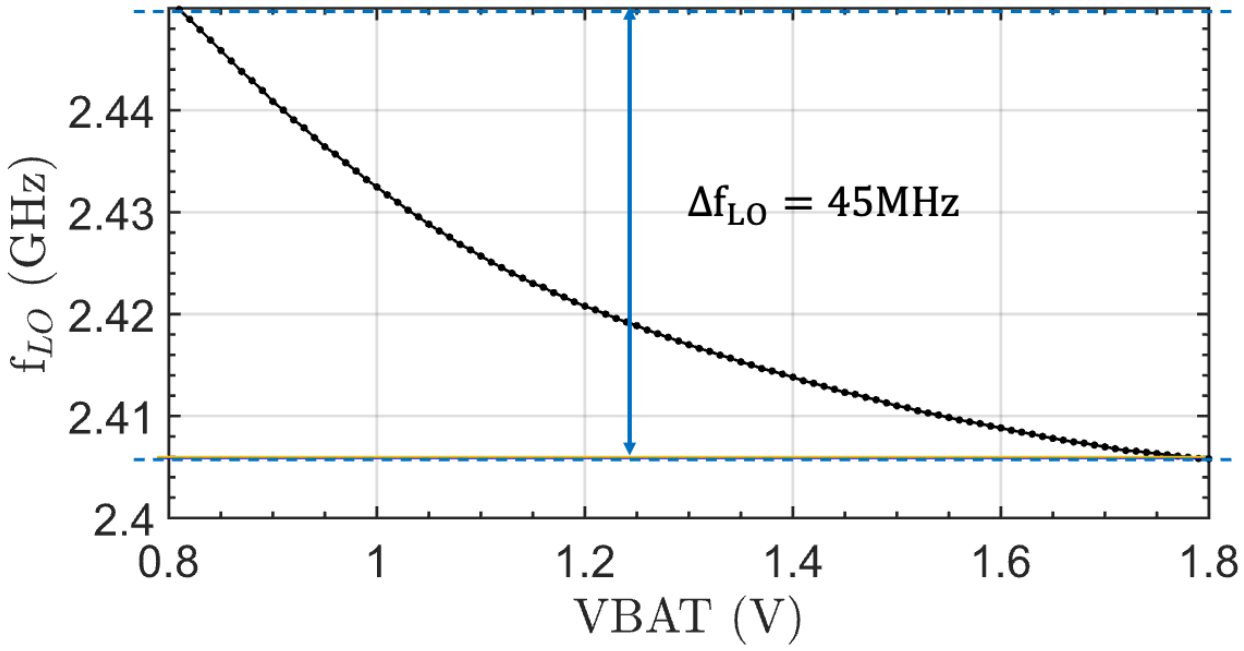

Figure 2.16: f_{LO} vs VBAT ±15 mV and ±55 mV are the max ΔVBAT while staying within ±40 ppm and ±150 ppm, respectively

The second phase of the compensation is understanding how f_{LO} varies with VBAT. The LO was calibrated to channel 11, $f_{\mathrm{LO}} \approx$ 2.405GHz, at 1.8 V. Then VBAT was swept from 1.8 V to 0.8 V at 10 mV steps and f_{LO} was measured with a spectrum analyzer. Fig. 2.16 demonstrates how for one CMF code f_{LO} varies by 45 MHz over ΔVBAT $= -1$V which is far away from the ±40 ppm requirement. Ideally, variation in VBAT would have no impact on f_{LO}. However, as can be seen in Fig. 2.16 with only a 15 mV drop in VBAT f_{LO} varies by 40 ppm. The OpenMote's CC2538 can tolerate up to ±150 ppm which means a 55 mV drop

is tolerable. Now that the max ΔVBAT is known for the 40 ppm and 150 ppm the look up table can be created.

Create a LUT for LO DAC codes vs VBAT

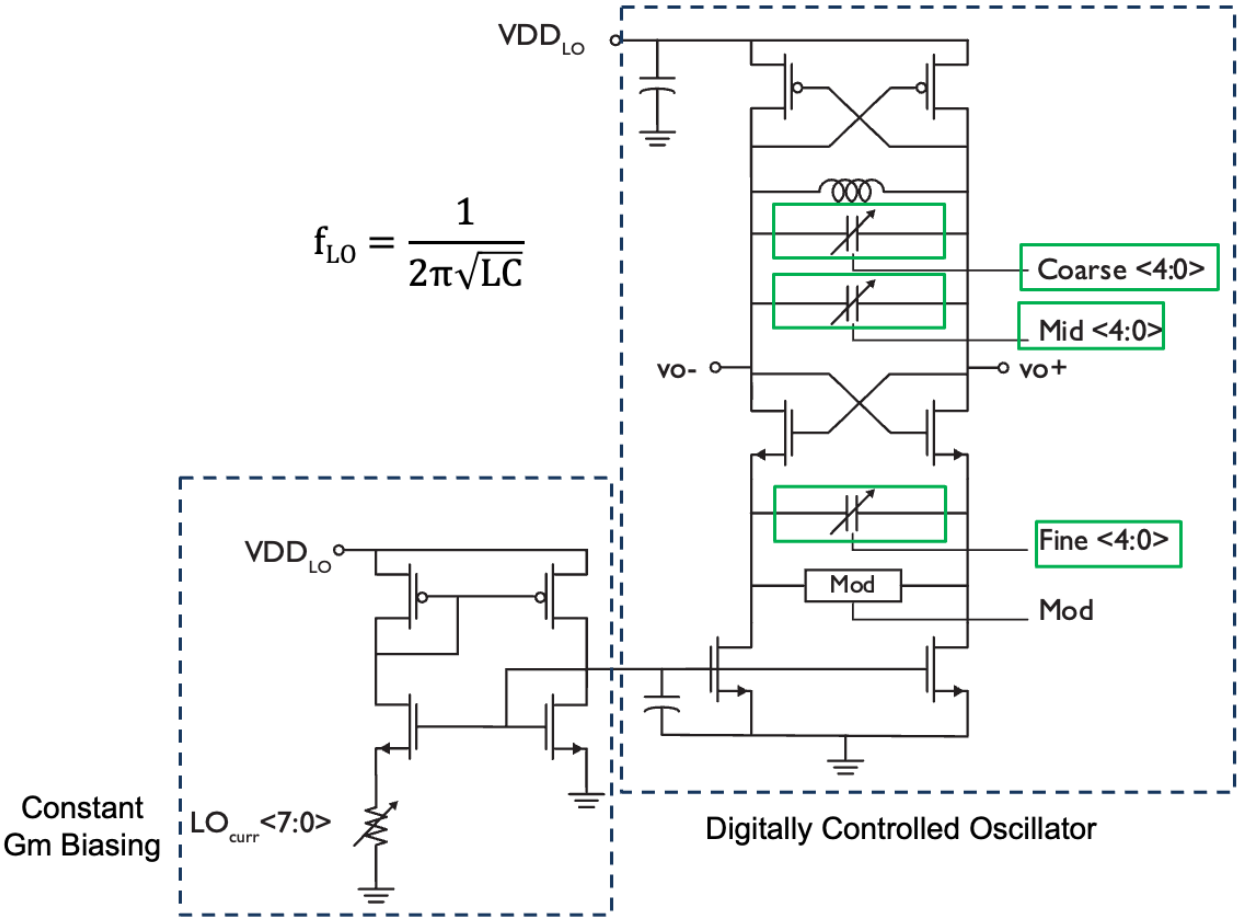

Figure 2.17: SCµM's LO is a class-B CMOS LC tank architecture that has a 15-bit capacitive DAC that is made up of three 5-bit capacitor banks, coarse, mid and fine (CMF). The very fine tuning resolution of 90-100 kHz is possible because of capacitive degeneration [52, 28]

Identifying what CMF code corresponds to what frequency as VBAT is dropping is nontrivial. This is because a single CMF code can vary by 45 MHz when ΔVBAT = -1 V. Fortunately, SCµM's LO has a 15-bit capacitive DAC that is made up of three 5-bit capacitor banks, coarse, mid and fine (CMF) as shown in Fig.2.17. To achieve the 802.15.4 ±40 ppm requirement, f_{LO} must be within ±96kHz at 2.4 GHz. SCµM's cap DAC is able to achieve a very fine tuning resolution of 90-100 kHz [51, 52]. This is possible because unlike the coarse and mid cap DAC the fine cap DAC is capacitively degenerated [28]. This means the effective

		100 uF	
VBAT	Coarse	Mid	Fine
1.81	22	17	18
1.8	22	17	17
1.79	22	17	16
1.78	22	17	14
1.77	22	17	12
1.76	22	17	11
1.75	22	17	9
1.74	22	17	8
1.73	22	17	6
1.72	22	17	5
1.71	22	17	3
1.7	22	17	0
1.69	22	16	8
1.68	22	16	6
1.67	22	16	4
1.66	22	16	2
1.65	22	16	0
1.64	22	15	5
1.63	22	15	3
1.62	22	15	1
1.61	22	14	7
1.6	22	14	5
1.59	breaks here		

Figure 2.18: SCµM's CMF DAC codes vs VBAT

capacitance seen by the inductor and capacitor (LC) tank is reduced by a factor of $\frac{1}{g_m^2}$. The effective capacitance change is as low as ≈9.4 aF, something impossible to do with single minimum-sized capacitor in a 65nm process. This occurs because the fine code Cap DAC is placed below the NMOS cross-coupled pair seen in Fig. 2.17. Crystal based radios typically don't have this fine of a tuning resolution because they use a phased locked loop (PLL) to tune to the right frequency channel. With SCµM's fine tuning capability, it is possible to find a DAC code that is within ±40 ppm of f_{LO} = 2.405GHz. Thus, a CMF code look up table versus VBAT was created using the steps below:

1. The Cap DAC coarse, mid, and fine (CMF) code is swept and included in the payload

while transmitting 802.15.4 packets.

2. The CMF code is swept until the OpenMote CC2538 receives a packet on channel 11, f_{LO}, with a low IF offset.
3. Once the CMF code is found it is added to a look up table for the respective VBAT
4. Decrease VBAT by 10 mV and repeat 1-3 until the look up table is complete

The creation of the look up table begins with SCµM's CMF codes being swept and included in a 125B 802.15.4 packet. With a wide enough CMF frequency sweep range, the OpenMote CC2538 eventually receives a packet[93]. Typically, there are a handful of CMF codes that are received but the packet with the lowest IF offset is selected. OpenMote's reported lowest IF offset means that CMF code is the closest to $f_{\text{LO}} = 2.405$GHz. Thus, that CMF code is added to the look up table. Then, VBAT is decreased by 10 mV and steps 1-3 are repeated until the table is complete as shown in Fig. 2.18. Notice that for for each ΔVBAT=10 mV the fine code changes by roughly one fine code which agrees with a ΔVBAT= 15mV causing a 40ppm/96 kHz change and the fine code having a tunig resolution of 90-100 kHz.

Estimate Δt_{update}

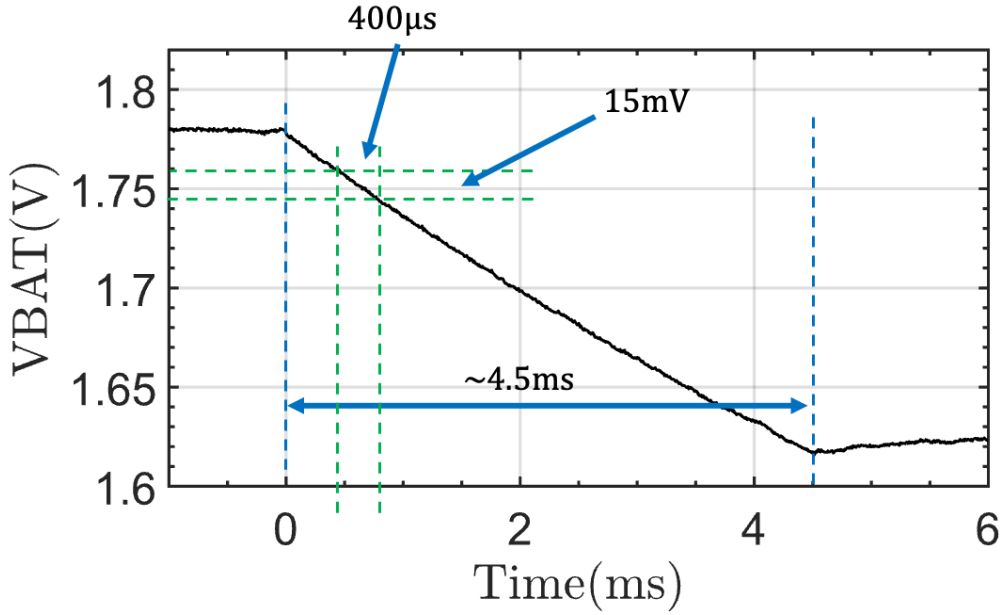

Figure 2.19: VBAT vs Time zoomed into the the transmission period which is ~4.5 ms.

The next step is to estimate the time between CMF code compensation updates. This is estimated by measuring VBAT versus time across C_{decap}. In Fig. 2.19 between t = 0 to

~4.5 ms, a 165 mV drop is seen due to the high current draw during packet transmission. The capacitance of C_{decap} determines how fast the voltage drops thus a bigger capacitor is desirable based off of $\frac{I_{\text{VBAT}}}{C_{\text{decap}}} = \frac{\text{dVBAT}}{\text{d}t}$. Δt_{update} can be estimated by using Fig. 2.16 and 2.19. To stay within ±40 ppm, a ~±100 kHz shift, a ΔVBAT =±15 mV is needed which corresponds to a $\Delta t_{\text{update}} \leq 400\mu$s. The OpenMote has a ±150 ppm tolerance, a ±360 kHz shift, thus a CMF code update would be needed for every 55 mV which corresponds to a $\Delta t_{\text{update}} \leq 1.4$ms. It takes about 4.5 ms to transmit a 125B 802.15.4 packet thus to meet the 150ppm requirement for the OpenMote at least 3 CMF updates would be required. Similarly, to meet the 40 ppm requirement for the 802.15.4 standard at least 11 updates would be required.

Frequency Compensation Results & Discussion

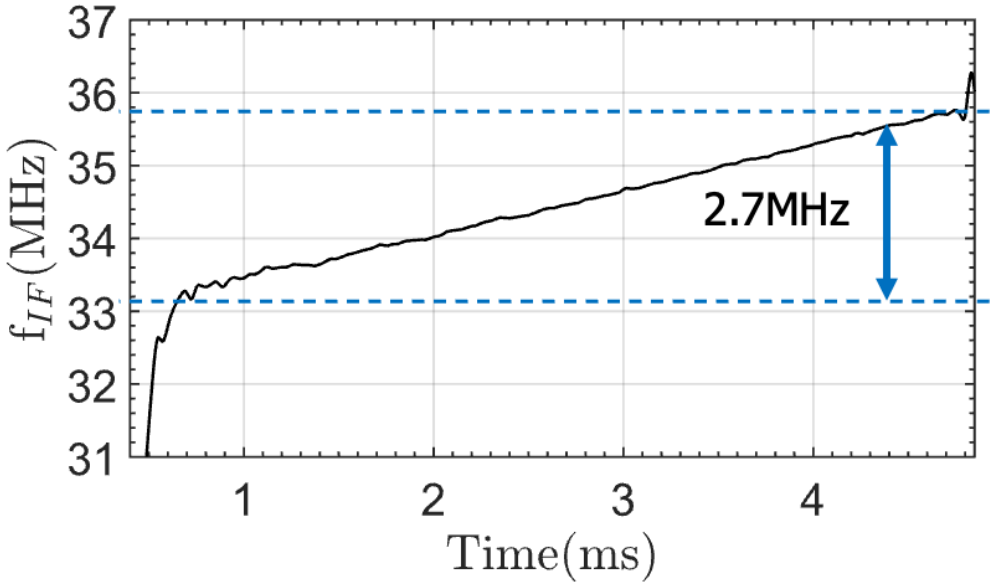

Figure 2.20: Frequency vs time with no compensation. During the transmission period the f_{IF} drifted 2.4 MHz from the initial frequency.

In order to capture the frequency shift due to VBAT, f_{LO} was mixed down by 2.3719 MHz to $f_{\text{IF}} = 33.1$MHz. This means that $\Delta f_{\text{LO}} = \Delta f_{\text{IF}}$. As can be seen in Fig. 2.20 f_{IF} drifts by 2.7 MHz during the transmission period, ~4.5 ms, thus at least 3 CMF updates are required to properly receive a full length packet on an OpenMote. In Fig. 2.21, 14 CMF code compensation updates with a $\Delta t_{\text{update}} \approx 300\mu$s were used resulting in only a $\Delta f_{\text{IF}} = 300$kHz. As a result, SCµM powered from solar under200 mW cm^{-2} of irradiation and a 0805 capacitor is no longer limited to sending smaller packets like the 10B packets in [62, 63] and can send full 125B length packets.

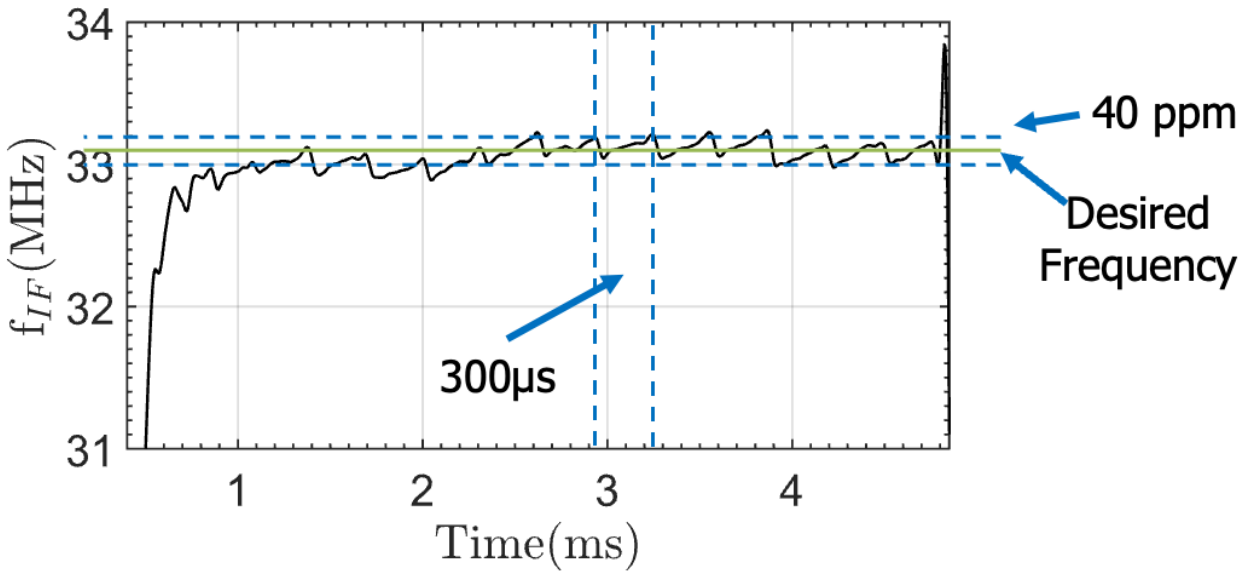

Figure 2.21: Frequency vs time with 14 CMF code compensation updates. As a result, there was only a shift of ~300 KHz from the desired frequency.

Another solution to this problem could have been using a bigger solar cell with a $I_{sc} \geq I_{VBAT}$ or an enormous capacitor with a ΔVBAT of only 15mV during transmission. However, the main objective for this work is to miniaturize the electronics so they can be used for building microrobots. Being able to compensate frequency while a packet is being transmitted means that smaller capacitors can be used such as an 0603 and an 0402 to offset the ΔVBAT and still be able to transmit an uncorrupted packet. To get a sense of scale the 0805 capacitor used for C_{decap} is 2x1.25x1.25 mm and weighs 26.2 mg. While 26.2 mg might not sound like much to a microrobot every single mg needs to be accounted for. How much does an 0805 differ from an 0402 capacitor? An 0402 capacitor is 1x0.5x0.5 mm and weighs 3.2 mg which translates to a reduction in volume by 12x and in weight by 8x in comparison to an 0805 capacitor. Initial work was done to show that compensation was possible on 0603 and 0402 capacitors. There are three potential limitations to consider:

1. Δt_{update}'s minimum resolution on SCµM is limited by the 500 kHz RF timer+code execution
2. CMF compensation currently only works for VBAT≥ 1.6V
3. LO settling time

How small can these capacitors theoretically be before things break down? To begin, the limits of Δt_{update} will be explored. To get an estimate of Δt_{update}, $I_{VBAT} = 1.6$mA during, a ΔVBAT $\leq \pm 15$mV to stay within 40 ppm and the effective capacitance of C_{decap} can be used. For an 0402 capacitor with the biggest capacitance possible, 22 µF, the effective capacitance

can be estimated $C_{\text{decap}} \approx 40\%22\mu\text{F} \approx 8.8\mu\text{F}$. Using Eq. 2.7 and plugging in the values, a $\Delta t_{\text{update}} \approx 82.5\mu\text{s}$ is calculated and translated to 55 CMF code updates being required to stay within ± 40 ppm. The CMF code updates were implemented using a timer that is based on a 500 kHz RF timer, which gives the timer a resolution of 2 µs. However, the CMF code update requires a few cycles from the 5 MHz Cortex clock to update the LO. Given that it takes 200 ns for one Cortex clock cycle it is very likely 400 clock cycles should be sufficient to update the CMF code. With an effective capacitance of $C_{\text{decap}} \approx 40\%22\mu\text{F} \approx 880\text{nF}$, an 0201 capacitor has a requirement of $\Delta t_{\text{update}} = 8.25\mu\text{s}$ thus approximately 31 Cortex clock cycles to update the CMF codes. This is likely approaching the limit of SCµM's update capabilities given the power constraints. However, further analysis needs to be done to understand the precise number of clock cycles required with optimization.

The second limitation is that VBAT$\geq$ 1.6V must hold true for this method to work, at least in its current state. Using $\Delta t_{\text{transmit}} = 4.5\text{ms}$, $I_{\text{VBAT}} = 1.6\text{mA}$, $C_{\text{decap}} = 8.8\mu\text{F}$ for an 0402 cap and 880 nF for an 0201 cap, VBAT would drop to 0.99 V and 0 V, respectively, if a full 125B packet were to be sent. Based on this it is not theoretically possible to transmit full 125B packets with these small capacitors with frequency compensation unless I_{VBAT} is reduced or I_{sc} is increased. However, a certain amount of bytes can be transmitted before VBAT drops below 1.6V. Using Eq. 2.7, $I_{\text{VBAT}} = 1.6\text{mA}$, $\Delta\text{VBAT}= 200\text{mV}$, $C_{\text{decap}} = 8.8\mu\text{F}$ for an 0402 cap and 880 nF for an 0201, the time valid data is being transmitted, Δt_{valid}, can be calculated. Δt_{valid} is 1.1 ms and 110 µs for an 0402 and 0201 cap which translates to 34B and 3B valid data, respectively. The 3B produced by the 0201 cap would not be able to transmit data since 802.15.4 packets use the first 6B for the preamble, start of packet delimiter and PHY header. However, there was some preliminary work done that demonstrates the VBAT $\geq$ 1.6V limitation might be based on the 2 MHz chipping clock going out of the ± 1000 ppm requirement for the OpenMote's CC2538. In Fig. 2.22, the 2 MHz Chipping Clock's frequency, $f_{2\,\text{MHz}}$, was measured as VBAT was decreased. The blue lines indicate that around 1.5 V $f_{2\,\text{MHz}}$ is outside of the 1000 ppm requirement which is close to the VBAT frequency compensation stopped working. If the 2 MHz chipping clock is indeed the issue and it were to be compensated, it could extend the compensation to range to 1.3 V. Thus, 85B and 8B packets could theoretically be transmitted with an 0402 and 0201 capacitor, respectively. The last issue to take into account is how long it takes for the LO to settle when switching CMF codes. The LO's cold start settling time was measured to be roughly 50 µs [52, 51]. It is unlikely the same amount of settling time is required for changes in frequency ~100 kHz versus the startup frequency change that goes from 0 Hz to 2.4 GHz. It is critical this is understood before attempting any of the techniques above for an 0201 capacitor.

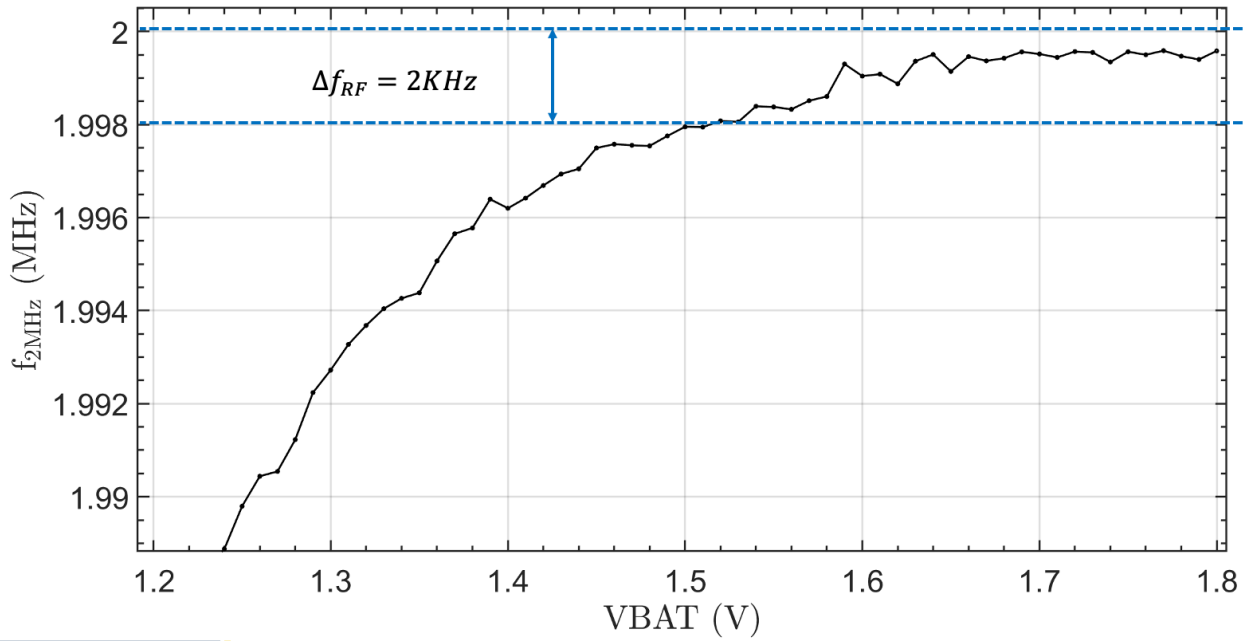

Figure 2.22: 2MHz Chipping Clock $f_{2\,\mathrm{MHz}}$ vs VBAT. The blue line demonstrate the 1000 ppm deviation, a $\Delta f_{2\,\mathrm{MHz}} = 20\mathrm{kHz}$

Chapter 3

Integrated Low Power Systems: Microrobots, Tracking Hornets and the Invisible Keyboard

3.1 The Small Autonomous Robot Actuator (SARA)

Introduction

One ideal for an autonomous microrobotic system is one composed of motors, mechanisms, sensing, computation, communication, and power, which is able to interact with its environment and the internet in an intelligent manner. Much progress has been made in the development of all of the required components, and in the integration of full systems. This section reports a modest level of autonomy in a modular combination of a small number of components, with application to a broader set of microrobots. The motor and mechanism used here is a MEMS gripper described in [81]. The gripper is a single degree-of-freedom actuator, very simple from a robotics perspective. But it is made in a MEMS fabrication process which has been used to fabricate more complicated robot structures, such as jumpers [82] and a twelve degree-of-freedom hexapod [22], as well as a quadthruster ionocraft [26]. The jumper and walker use the same basic electrostatic inchworm motor as the gripper. The high voltage chip used here, Zappy2, was designed to drive this type of motor.

Previous work on untethered systems has shown that small robots are able to accomplish interesting tasks in healthcare and bioengineering [85], and construction [34]. In many cases these untethered robots might benefit from a wireless microgripper attachment, as would some of the autonomous robots below.

There are many small autonomous robot systems in the multiple cubic inch size range [77, 76, 11]. Communication is a key enabler in several of these systems [77, 23]. Indeed, communication may be the only area in which man-made microrobots can outperform their natural counterparts. While IR communication is simple and useful for local operations, RF communication allows longer-range, multi-hop mesh networks, and easier integration into

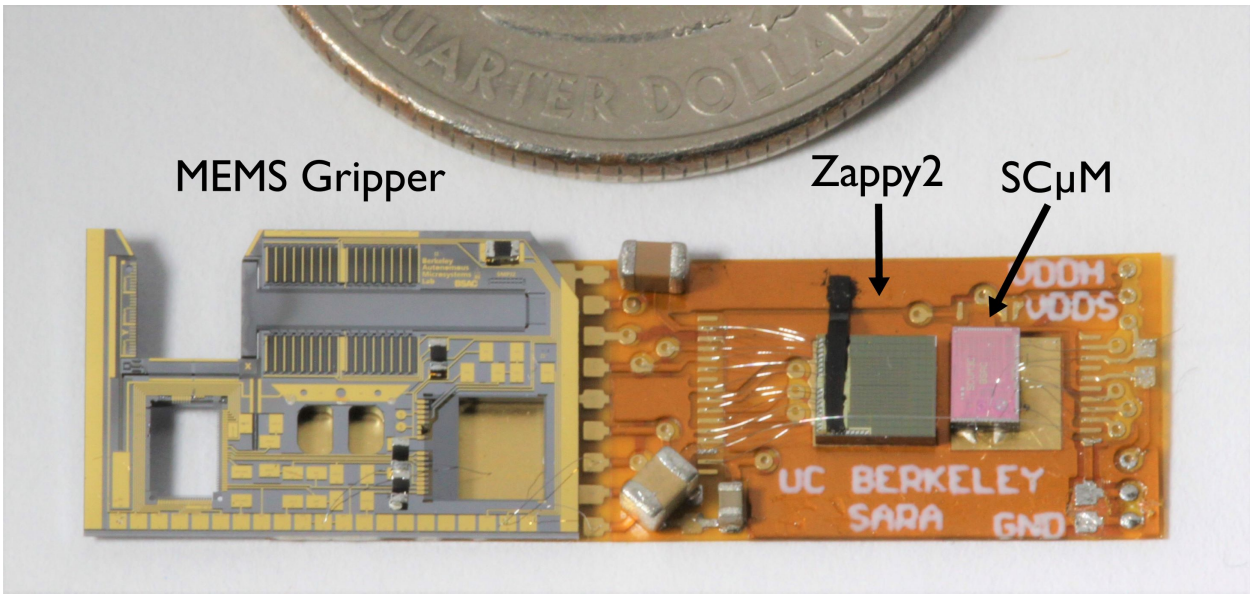

Figure 3.1: MEMS Gripper, HV Buffer & Solar Cell Array Chip, Single Chip Micro Mote (left to right). Two SCμM chips are stacked due to initial SCμM malfunctioning. The dimensions of SARA are 9.5 mm×31.55 mm

existing networks and infrastructure. The Bluetooth chip used by Iyer, et al. [37] allowed them to send images over 120 meters. The radio used by Sabelhaus et al. [77] speaks the 802.15.4 PHY and MAC protocol natively. This protocol is the basis of a highly reliable low power mesh networking communication stack, OpenWSN [96]. The Single Chip micro Mote, SCμM, was designed to perform the computation and communication required by swarms of simple microrobots, and is able to run the OpenWSN stack [14]. It has some features in common with the chip developed by Zhang et al. [103].

There have been several autonomous microrobots in the sub-gram size range, mostly aerial vehicles. The 10 mg robot built by Hollar et al. [33] used inchworm motors and a solar cell array and was able to do autonomous pushups, with a small amount of lateral motion, under roughly one sun of illumination. The controller was a simple CMOS finite state machine, with no sensor feedback. The 300 mg robot built by Churaman et al. [18] was able to jump 11 body lengths when triggered by an on-board light sensor. The logic was hard-wired. James et al. [39] were the first to achieve takeoff, however briefly, of a 190 mg robot under 200 suns of illumination. The 259 mg robot built by Jafferis et al. [38] achieved many body lengths of autonomous flight under only a few suns of illumination. Both of these last two flapping wing robots used open-loop control, but included a digital microcontroller, indicating that future sensor integration will be possible.

Previous work has demonstrated the operation of electrostatic inchworm motors using multi-junction solar cell arrays [78], coupled with an external silicon leg-sweeping mechanism. Bellew et al. [4] demonstrated the integration of solar cells, CMOS, and MEMS into a single

Table 3.1: SARA Weight Specifications

Item	Mass (mg)
Empty Flex PCB	71.8
SCµM (Stacked)	8.6
Zappy 2	17.3
MEMS Gripper	137.9
0402 Capacitor (22 µF VDDIO)	3.8
0805 Capacitor (100 µF VBAT)	26.2
0805 Capacitor (100 nF VDDH)	17.2
Solder and wirebonds	3.1
Total Mass	285.9

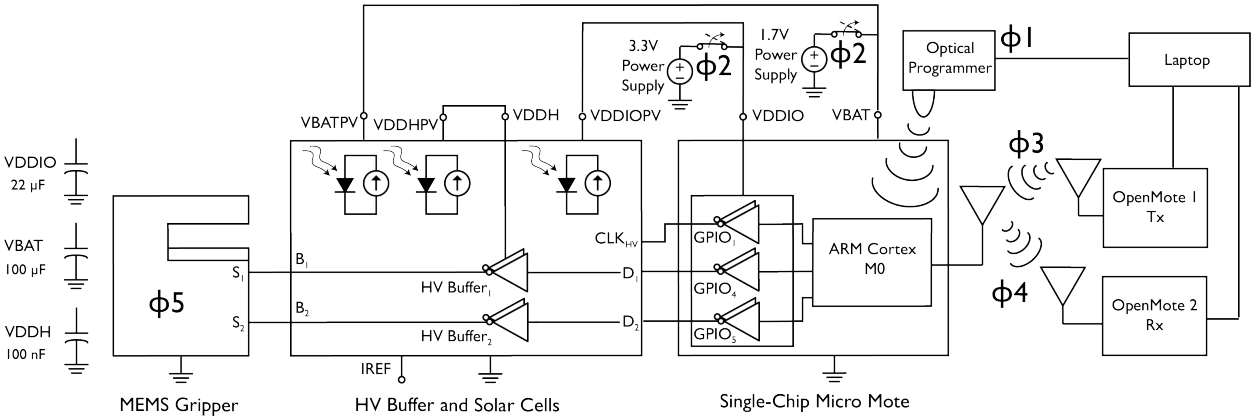

Figure 3.2: System block diagram including power domains, phases of operation, and all components.

process, pointing to a future in which the size, weight, and frustration associated with multi-chip assembly is minimized.

The work described here is a step toward demonstrating standards-compatible mesh-networked swarms of centimeter-scale microrobots.

System Description

The SARA robot consists of three chips and three capacitors. In addition, two OpenMote B CC2538 IoT devices were used for RF communication between SARA and a laptop, one for sending commands to SCµM and the other for receiving from SCµM [93]. Additionally, a

Teensy 3.6 microcontroller with an infrared LED was used to optically program and calibrate the SCµM chip [97]. The block diagram of the system can be seen in Figure 3.2.

SCµM: Crystal-Free Radio and Microprocessor

SCµM is a $3\times2\times0.3\,\text{mm}^3$ CMOS SoC featuring an ARM Cortex-M0 microprocessor, BLE transmitter, and a standards-compatible crystal-free 802.15.4 transceiver [52]. The chip also features an ADC, 16 0.8 V-3.6 V GPIOs, and an optical receiver used for optical programming and calibration. SCµM requires only one 1.2 V-1.8 V power supply connected to VBAT to operate [52], but the GPIOs may be driven from a separate supply, VDDIO. In order for SCµM to properly drive the high voltage buffers on Zappy2, the solar cell array provides VBAT = 1.8 V and VDDIO = 3.5 V.

Table 3.2: SCµM System Clocks

Clock	Purpose
20 MHz RC	Source for Cortex microprocessor
2.4 GHz LC	Dictates radio channel frequency
2 MHz RC	Radio chipping clock
64 MHz RC	Sample RF intermediate frequency
500 kHz RC (derived)	User-defined interrupts

Table 3.3: SCµM Operating Current (1.5 V)

State	Approximate Current
5 MHz Clock Rate (Normal)	350 µA
5 MHz Clock Rate (Radio on)	1.6 mA
78 kHz Clock Rate (Low power)	200 µA

By removing the crystal reference, SCµM is able to further reduce size and cost of microrobotic devices. In place of a crystal reference, SCµM uses on-chip CMOS oscillators as detailed in Table 3.2. However, this means that on-chip oscillators need to be calibrated to ensure standards compatible 802.15.4 radio operation. Notably, the 2.4 GHz LC oscillator used to set the local oscillator (LO) at the desired radio channel frequency is configured using three, 5-bit capacitive tuning DACs referred to as the coarse, mid, and fine tuning settings. Other calibrated clocks include the 20 MHz CPU clock, 2 MHz chipping clock, and 64 MHz receiver intermediate frequency sampling clock. Calibration of these clocks has been successfully demonstrated using several different approaches, including an optical programmer

[97], temperature-based calibration [101, 64], and RF-based calibration using only packets overheard [88, 89, 13]. The work reported here used the optical programmer.

During normal operation the 20 MHz RC oscillator is divided down to 5 MHz for use as the clock for the Cortex microprocessor. For lower power consumption this oscillator is divided to 78 kHz. The current consumption at these various operating conditions can be seen in Table 3.3.

Zappy 2: Solar Cell and High Voltage Buffers

Zappy2 contains the photovoltaic (PV) arrays that power the robot and high voltage buffers to drive the motors. The $3.26\times3.5\,mm^2$ chip is fabricated in a 650 V trench-isolated CMOS process and contains more than two hundred PV cells [71]. These PV cells are grouped in series to provide three voltage domains: one to power SCµM (VBATPV; 1.8 V), one as a reference for the SCµM's GPIOs (VDDIOPV; 3.5 V), and one as a high voltage rail to power the electrostatic motors on the MEMS gripper (VDDHPV; 119 V). The performance characteristics of the solar cell arrays are shown in Table 3.4. Three capacitors of size 100 µF, 22 µF, and 100 nF are used to maintain voltage across VBAT, VDDIO, and VDDH, respectively (Figure 3.2). In the SARA robot, the lowest allowable successful operating voltages of VBAT, VDDIO and VDDH were measured to be 1.3 V, 3.3 V and 40 V, respectively.

Table 3.4: Solar Output Specifications at $100\,mW/cm^2$ Irradiation

	VBATPV	VDDIOPV	VDDHPV
V_{OC}	1.8 V	3.5 V	119 V
I_{SC}	280 µA	16 µA	2.4 µA

Zappy2 also contains four high voltage (HV) buffers, two of which are needed to drive a single inchworm motor. These buffers hard switch their outputs between 0 V and VDDHPV at a rate determined by the switching of the input signals. SCµM uses two GPIOs to drive two buffers, and a third GPIO to generate the CLK_{HV}=100 kHz source needed for the Zappy2 internal digital state machine.

Hard switching the HV lines is sub-optimal for electrical to mechanical conversion efficiency, and because it requires significant capacitance on the HV supply to avoid drooping in the supply voltage. Both of these problems can be solved using an improved version of the HV chip [48], but for SARA we simply added a HV capacitor that was large compared to the load capacitance of the electrostatic actuators, roughly 70 pF.

For this SARA integration, the solar array is provided with $200\,mW/cm^2$ irradiation to provide VBATPV to SCµM with 560 µA at 1.86 V.

Figure 2.3 shows a simple model of the VBAT supply and consumption, discussed below.

Gripper: MEMS SOI 15 mN Gripper

The $14.5\times9.5\times0.6\,\mathrm{mm}^3$ MEMS gripper used in SARA is a later iteration of the design by Schindler et al. [81]. The gripper is microfabricated in a three mask silicon-on-insulator process with a 40 µm thick device layer, and in this silicon device layer is an electrostatic inchworm motor—using the motor architecture proposed in [67]—which linearly actuates the gripper jaw up to 3 mm when suitably powered. The motor consists of a shuttle and two arrays of gap closing actuator finger pairs (with 1536 finger pairs per array). Each of these arrays is a capacitive transducer connected to ground and one high voltage (>40 V) input signal. The input signals are generated by the SCµM chip and buffered to high voltage by Zappy2. When an input signal is raised to a high voltage, the corresponding array charges, closing its finger pairs, and via a compliant mechanical linkage pushes the shuttle forward 2 µm then holds it in place. If the second array is then charged and the first is released, the shuttle moves an additional 2 µm. Driving the two arrays with >50 % duty cycle square waves 180 degrees out of phase creates continuous movement. When both arrays are discharged simultaneously, the shuttle is free to move and is retracted by a silicon serpentine spring; this is how the gripper jaw returns to its original position.

As with stepper motors, since the motor moves a fixed distance every input signal period, its actuation speed is proportional to the input signal frequency f [67]. In this implementation with $d = 2\,\mu\mathrm{m/step}$ and $n = 2$ steps/period, the motor moves at speed $n{\cdot}d{\cdot}f$: $1\,\mathrm{mm\,s^{-1}}$ at 250 Hz or $4\,\mu\mathrm{m\,s^{-1}}$ at 1 Hz. This gripper has been successfully actuated at speeds up to $1\,\mathrm{mm\,s^{-1}}$ with an external power supply (likely limited by excessive friction in the integrated system) [81]. Experimental tests of the same motor architecture have demonstrated $35\,\mathrm{mm\,s^{-1}}$ movement [20].

Each of the two capacitive transducer arrays has approximately 40 pF maximum (closed) capacitance (and a parasitic 30 pF in parallel for total capacitance $C \approx 70\mathrm{pF}$). When its input signal is raised high, the array charges with energy $\frac{1}{2}CV^2$ and puts an additional $\frac{1}{2}CV^2$ toward mechanical work and heat. When the signal is returned to ground the stored capacitive energy is lost. Thus the power draw of the entire motor on the drive electronics is approximately $2{\cdot}\frac{1}{2}CV^2{\cdot}n{\cdot}f$, e.g., 0.35 mW at $1\,\mathrm{mm\,s^{-1}}$ and 100 V, or 56 µW at $1\,\mathrm{mm\,s^{-1}}$ and 40 V. Note that at zero speed, i.e., holding position without movement, the motor theoretically draws negligible power. In reality, leakage current due to parasitics, especially parallel resistance when the array fingers are closed, can dominate; we explore this in later sections (see Figure 3.7). The advantage of higher voltage is that the motor force is proportional to voltage squared: this motor, after inefficiencies, provides up to 15 mN at 100 V or 2.4 mN at 40 V [81]. Motor efficiency as defined by [67] is $\eta \approx 15\mathrm{mN}{\cdot}2\mu\mathrm{m}/\frac{1}{2}CV^2 \approx 9\%$ (and parasitics—see Figure 3.7—reduce this further). This could be increased significantly by using a variable-voltage driving waveform to reduce both nonlinearities in the capacitive transducer and RC charging losses [67, 48].

System Operation

The integrated SARA microsystem operates in 5 phases indicated in Figure 3.2 and detailed in this section.

Phase 1: Optical Calibration

A Teensy 3.6 microcontroller with an IR LED is used to send signals to the optical receiver on SCµM in order to bootload a program [97]. After programming, SCµM enters an optical calibration phase. This calibration is needed to calibrate the CMOS oscillators on SCµM since the chip lacks a crystal reference. The same IR programmer sends 20 pulses of an optical signal at 10 Hz to trigger optical interrupts on SCµM [97]. Upon receiving an interrupt, SCµM uses the time between interrupts as an absolute reference for calibrating its oscillators. The calibrated clocks include a 20 MHz HF CPU clock, a 2 MHz RC chipping clock, and an IF radio clock.

During bootup, SCµM has the following VBAT current transient: 300 µA unprogrammed/idle, 350 µA for 0.5 s while programming and initializing, 1.6 mA optical calibration for 2 s, and lastly idle at 350 µA. The 1.6 mA exceeds the 560 µA provided by the solar cells at 200 mW/cm^2. Thus, while calibrating, SCµM is connected to an external 1.7 V VBAT. Additionally, an external 3.3 V VDDIO source is connected during calibration to ensure that the Zappy2 FSM is properly initialized.

Phase 2: Solar Power and LC Calibration

Once calibrated, the external 1.7 V and 3.3 V power sources are disconnected and SCµM operates autonomously on solar power from Zappy2. Under 200 mW/cm^2 irradiation (2 suns) provided by a fiber optic light illuminator, the solar cells provide 560 µA at 1.86 V. This provides power to operate SCµM at a reduced 78 kHz clock rate (I_{VBAT}=200 µA) between periods of full speed operation at 5 MHz (I_{VBAT}=350 µA). The 2 suns illumination was chosen as the 560 µA current provided exceeds the I_{VBAT}=350 µA idle current. Additionally, it provides enough current along with the 100 µF VBAT capacitor to operate SCµM with radio-on I_{VBAT}=1.6 mA for ~2 ms periods while still maintaining 802.15.4 standard compatibility. Further justification is provided in section 3.1.

Additional calibration is required to set the radio local oscillator frequency to properly transmit 802.15.4 packets at 2.405 GHz for channel 11 as well as receive packets at 2.410 GHz on 802.15.4 channel 12. This additional calibration is needed as the optical programming phase is not able to accurately calibrate the local oscillator. This occurs because when calibrating the local oscillator the divider chain is required to be turned on which increases the current consumption from 1.6 mA to more than 2 mA. Attempts to turn the divider chain off after calibration resulted in the local oscillator shifting it's frequency. Thus, to calibrate, SCµM sweeps across tuning settings with the divider chain off for each of the three 5-bit capacitive DACs used to set the frequency for the LC local oscillator (coarse, mid, and fine settings). The LC codes are swept until a packet is properly transmitted on channel 11 to an

RX OpenMote. Next, the LC codes are again swept until SCµM properly receives a packet on channel 12 from an TX OpenMote (Figure 3.2). The TX and RX LC configuration codes are then fixed and SCµM is now properly calibrated to transmit and receive on those specific channels.

The LC is calibrated with the goal of maintaining 802.15.4 standard compatibility. This standard defines a ±40 ppm maximum local oscillator frequency error which is difficult to achieve without a crystal reference. This is especially challenging in an energy-constrained and solar-powered system due to large voltage drops across the 100 µF VBAT capacitor that occur during radio operation which shift the frequencies of the CMOS oscillators (see section 3.1).

Furthermore, this calibration is complicated by the 160 ppm/°C [99] and −40 ppm/°C [52] temperature dependence of the 2 MHz radio chipping clock and 2.4 GHz radio local oscillator, respectively.

In prior work, SCµM and Zappy2 have been integrated into a wireless temperature sensing node featuring temperature based LC compensation across a temperature range of 35.5 °C to 40.0 °C [64]. For this integration the LC codes are fixed as previously described rather than continuously calibrated. Future work could integrate this continuous LC calibration into the SARA robot.

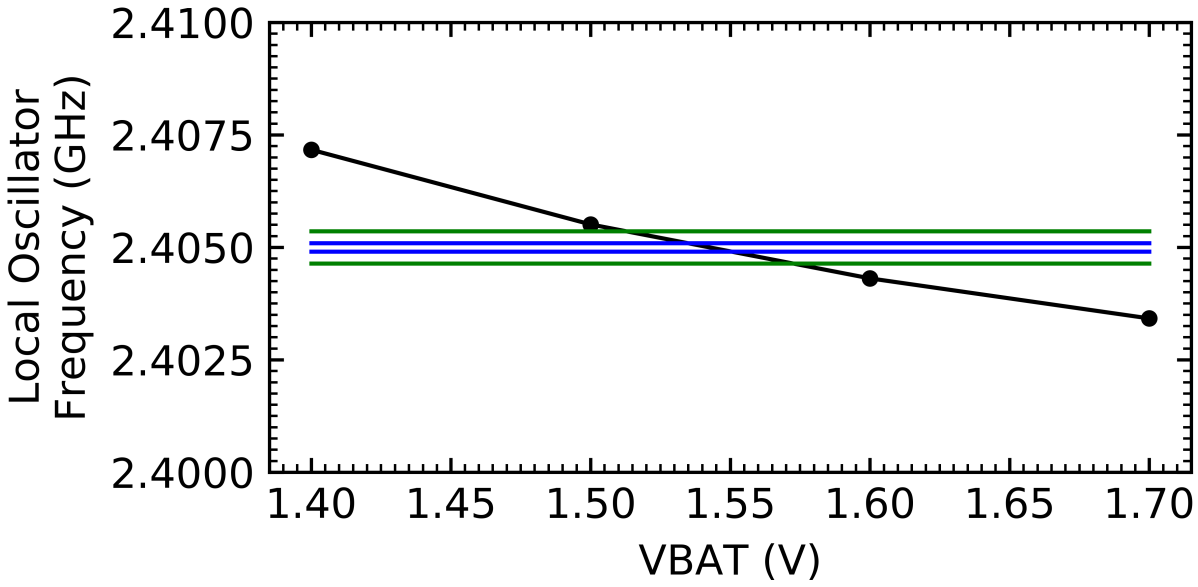

Figure 3.3: Crystal-free radio local oscillator frequency vs. VBAT voltage at a fixed LC tuning setting. The blue lines shows the ±40 ppm tolerance band of the 802.15.4 standard and the green lines shows the ±150 ppm tolerance of the OpenMote.

Phase 3: Receive Packets

While operating, the radio is enabled for 1 ms to attempt to receive an 802.15.4 packet from a TX OpenMote (Figure 3.2). This requires 1.6 µC of charge for I_{radio_on}=1.6 mA. The transient current of SCµM during radio operation under solar power can be seen in Figure 3.4. The 1 ms radio on period was chosen to minimize voltage drop on VBAT while the radio is on. The TX OpenMote is continuously transmitting 6 byte packets with a command to actuate the gripper. Phase ϕ_3 is repeated approximately every second until a command is received. The time in between repetitive Phase ϕ_3s could be reduced.

With the solar cell array under 200 mW/cm^2 irradiation and the 100 µF bypass capacitor across VBATPV, SCµM receives 560 µA at 1.86 V. This can power SCµM at I_{radio_on} of 1.6 mA for 25 ms before VBAT drops from 1.86 V to the operating minimum of 1.3 V. Additionally, SCµM has been shown to send and receive packets under solar with a 20 µF capacitor which can keep the radio on for 11 ms.

In practice, however, such a large voltage drop across VBAT shifts the local oscillator frequency and prevents proper radio operation (Figure 3.3). The slope of the LO frequency vs. VBAT curve (Figure 3.3) at VBAT=1.8 V is approximately 5 MHz V^{-1}. To maintain ±40 ppm stability (±100 kHz), the VBAT supply must be stable to less than ±20 mV variation. A 20 mV VBAT drop limit permits the radio to be enabled for at most 1.92 ms to maintain standards compatibility.

Specifically, based on the frequency shift from 2.4028 GHz at I_{VBAT}=1.8 V to 2.4023 GHz at I_{VBAT}=1.9 V (Figure 3.3), the VBAT voltage on SCµM must shift at most ±20 mV during a period of radio operation to ensure the frequency stays within the ±40 ppm frequency tolerance.

Phase 4: Transmit acknowledgement

After receiving a command to close the gripper, SCµM enables its radio for 4 ms to transmit a 10 byte packet to an OpenMote to confirm that the command was received. The current consumption during the 4 ms transmission period is presented in Figure 3.6. It should be noted that the transmitter should theoretically take closer to 0.4 ms to transmit a 10 byte packet. However, in practice the packet received by the OpenMote would be corrupt if the radio-on time was reduced too much. Transmitting packets is difficult due to high radio-on current draw which causes a drop in VBAT voltage as charge is pulled from the 100 µF VBAT bypass capacitor. The challenges of maintaining the proper local oscillator frequency are similar to those described in section 3.1, but now the radio is on for a longer period of time (4 ms TX vs. 1 ms RX). Despite this increased radio on period, SCµM was able to properly send packets as the transmission completes within the first 1 ms (corresponds to ~40 mV VBAT drop; see Figure 3.5). Further development has decreased the total radio on time to 1 ms. The OpenMote device used for these tests has a higher ±150 ppm frequency tolerance [99] over the ±40 ppm tolerance in the 802.15.4 standard. This increased tolerance was leveraged to help receive packets from SCµM.

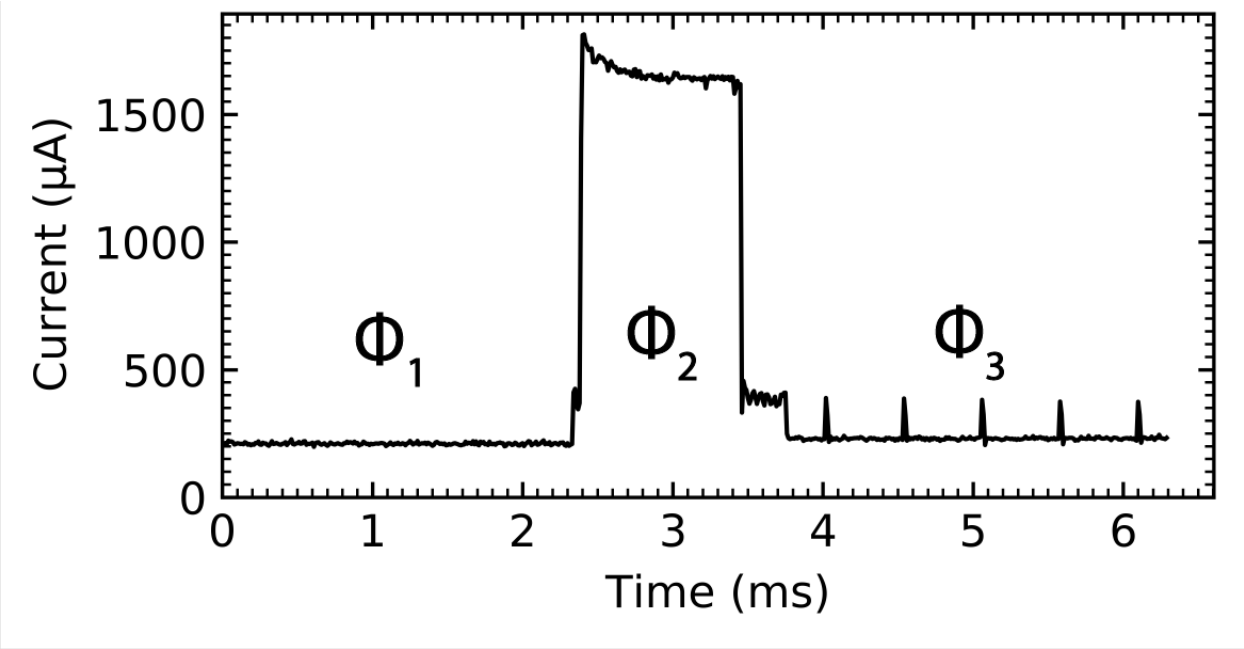

Figure 3.4: VBAT current during wireless 802.15.4 receive (200 mW/cm^2 irradiation; 47 µF VBAT bypass capacitor). ϕ_1: Low power (F_{cortex}=78 kHz), ϕ_2: RX with radio on, ϕ_3: periodic wake up to F_{cortex}=5 MHz

Phase 5: MEMS Gripper Actuation

After sending the acknowledgement that the command to close the gripper was received, SCµM begins sending three control signals through GPIO pins 1, 4, and 5 (powered by VDDIOPV) to Zappy2 (Figure 3.2). The GPIO output specifications can be seen in Table 3.5. The first signal originates from the SCµM 500 kHz RF timer and is passed through GPIO 1 (Figure 3.2) as the CLK_{HV} clock source for the Zappy2 digital state machine. GPIO pins 4 and 5 are fed into two of the four high voltage (HV) buffers on Zappy2, which in turn connect the gripper to the Zappy2 VDDHPV HV source. Toggling these pins from 0 V to 3.5 V (with a 60 % duty cycle) and 180 degrees out of phase with each other actuates the electrostatic inchworm motor of the gripper as described in section 3.1.

The current provided by the VDDHPV source on the solar cell and the current consumption of the gripper while held at a DC voltage can be seen in Figure 3.7. The GPIO signals and the corresponding buffered HV signals used for gripper actuation can be seen in Figure 3.8.

We can use Figure 3.7 to determine the maximum speed operating points of the gripper. Because the gripper is capacitive, its speed, as in section 3.1, is determined solely by its driving frequency while it charges to the maximum voltage (and thus force) available. At fast speeds, however, insufficient power is supplied to charge the gripper each signal period so the voltage across its capacitance decreases. Once the voltage falls below the minimum

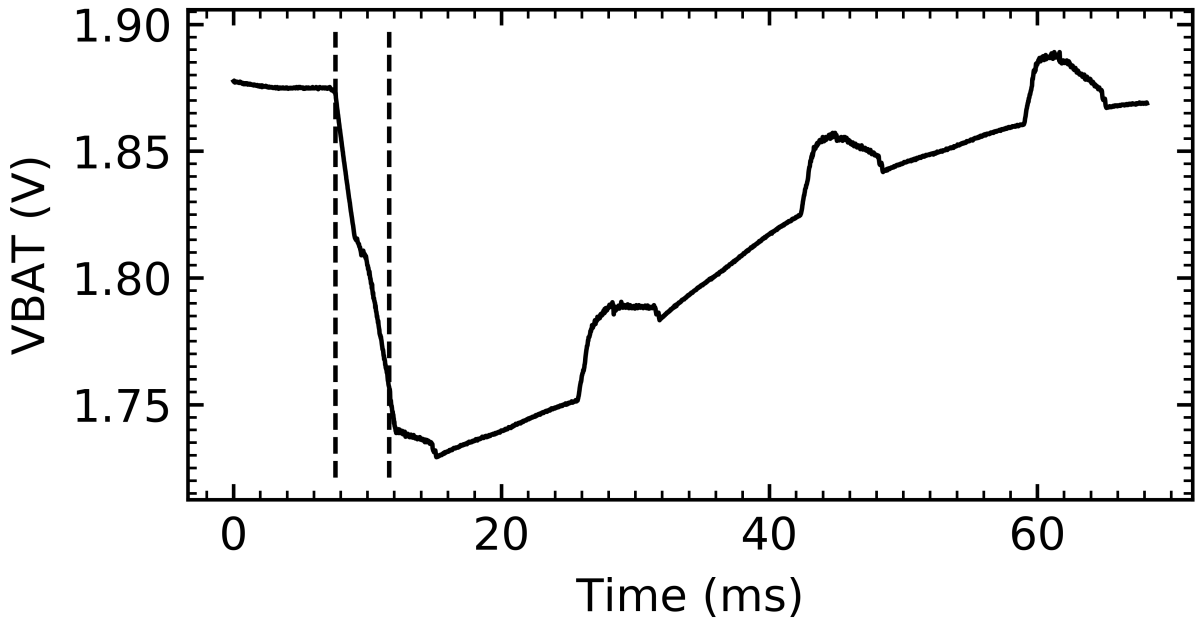

Figure 3.5: VBAT voltage vs. time during wireless 802.15.4 transmit (200 mW/cm^2 irradiation; 100 µF bypass capacitor). The dashed lines indicate the 4 ms period when the radio was enabled.

Table 3.5: $GPIO_{output}$ Specifications

Specification	Value
VDDIO	0.8-3.6 V
VDDAUX	0.8-1.2 V
F_{max} @ HCLK = 10 MHz	734.25 KHz
$I_{VDDIOleakage}$ @ VDDIO = 3.3 V	4.37 nA
$I_{sink/source}$ @ VDDIO = 3.3 V	19 mA

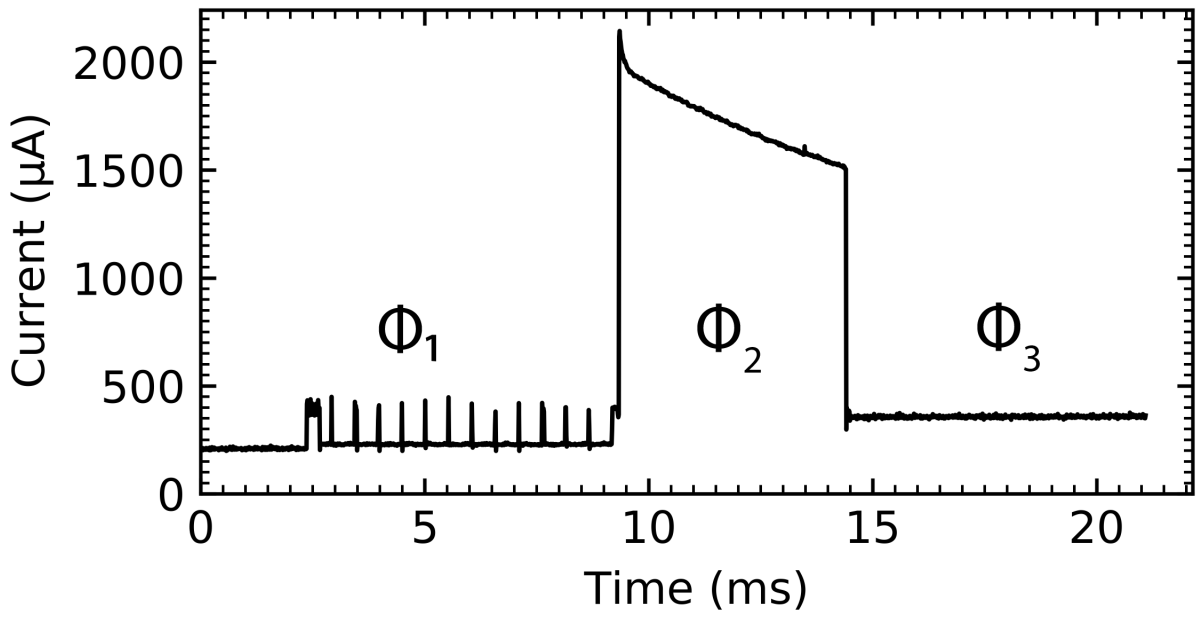

Figure 3.6: VBAT current during wireless 802.15.4 transmit (200 mW/cm^2 irradiation; 20 µF bypass capacitor). Phases: ϕ_1: F_{cortex}=78 kHz low power mode and UART logging before transmit, ϕ_2: Transmit 10 byte packet, ϕ_3: F_{cortex}=5 MHz idle state

40 V, the gripper fails to move. In this implementation, however, the gripper also has non-negligible leakage current draw under DC input. This sets the minimum power draw of the gripper at a given voltage as its speed approaches zero and duty cycle approaches 100%.

Thus, under 200 mW/cm^2 irradiation, the operating point of the HV buffers and the gripper (for slow speeds and high duty cycles) is ~4.75 µA at ~59 V (Figure 3.7). According to section 3.1, at this voltage, the force of the gripper is approximately 5.2 mN. If we assume the leakage current graphed in Figure 3.7 only appears across the gripper when a motor array is charged (i.e., the gap closing actuators are closed, which makes sense if their fingers are touching and causing a high-resistance short), then the proportion remaining power available to actuate the gripper is 1 minus the duty cycle (here, 60%), for 4.75µA·59V·0.4 = 0.11mW, which is sufficient for up to 920 µm s^{-1} speed. While testing the integrated SARA system at 200 mW/cm^2 irradiation, GPIO toggling speeds up to 160 Hz resulted in movement, corresponding to a maximum speed of 640 µm s^{-1} closing the full 3 mm distance under solar power in ~4.7 s (the slower-than-theoretical maximum achievable speed implies some of the gripper leakage is always present, reducing power available for movement, and friction may also play a role).

Each of the three Zappy2 voltage domains (VBATPV, VDDIOPV, and VDDHPV) must maintain a minimum voltage during actuation of the MEMS gripper. During gripper actuation, SCµM operates at a F_{cortex}=78 kHz with I_{VBAT}=200 µA. This is within the 560 µA

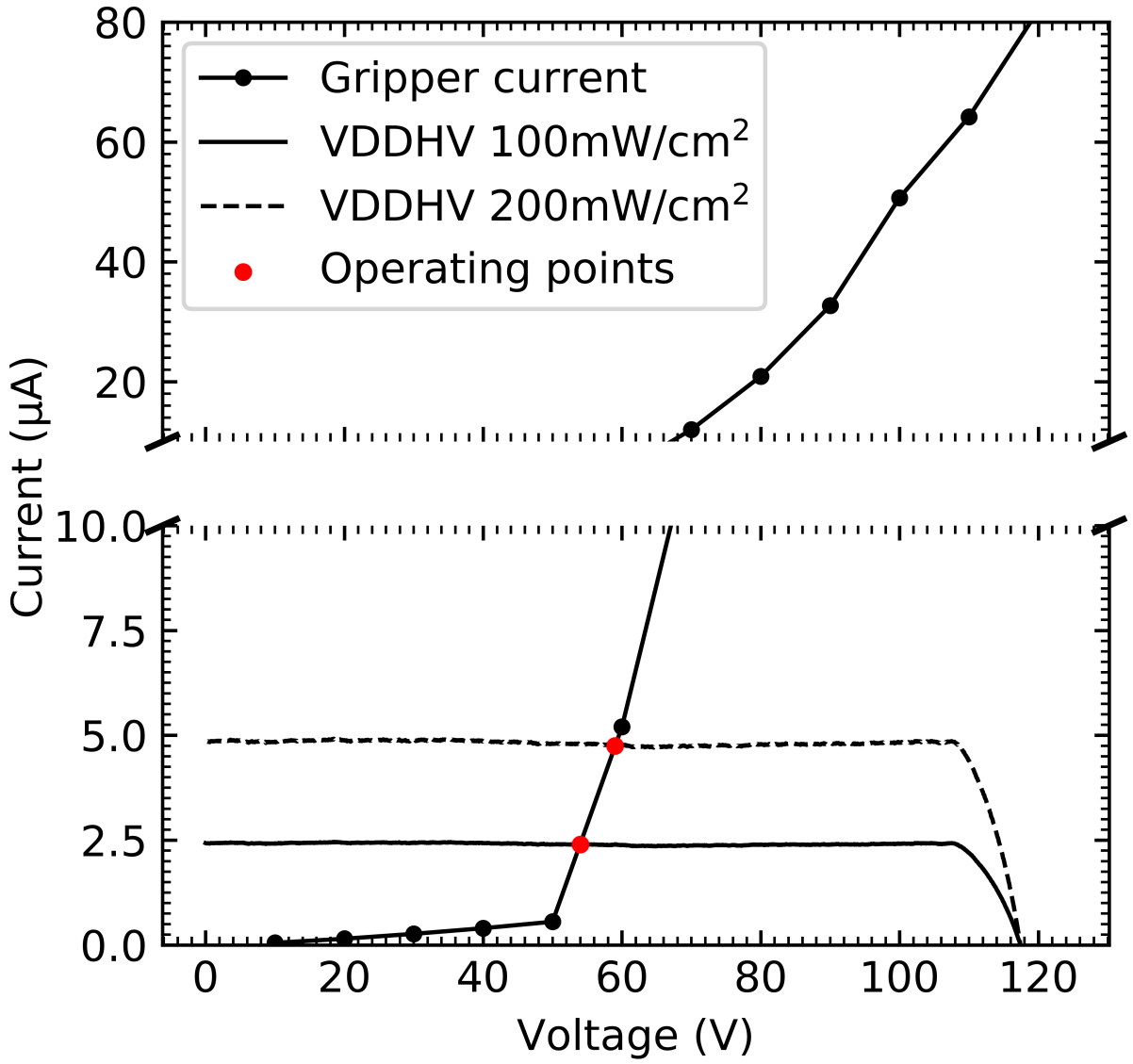

Figure 3.7: Measured gripper leakage current under DC supply vs. HV buffer DC voltage, and Zappy2 VDDHPV supply current vs. VDDHPV voltage under 100 mW/cm^2 (measured) and 200 mW/cm^2 irradiation (estimated). Red intersections represent operating points of the system at 100 mW/cm^2 and 200 mW/cm^2 irradiation while closing the gripper at very slow speeds approaching zero and duty cycles approaching 100 %.

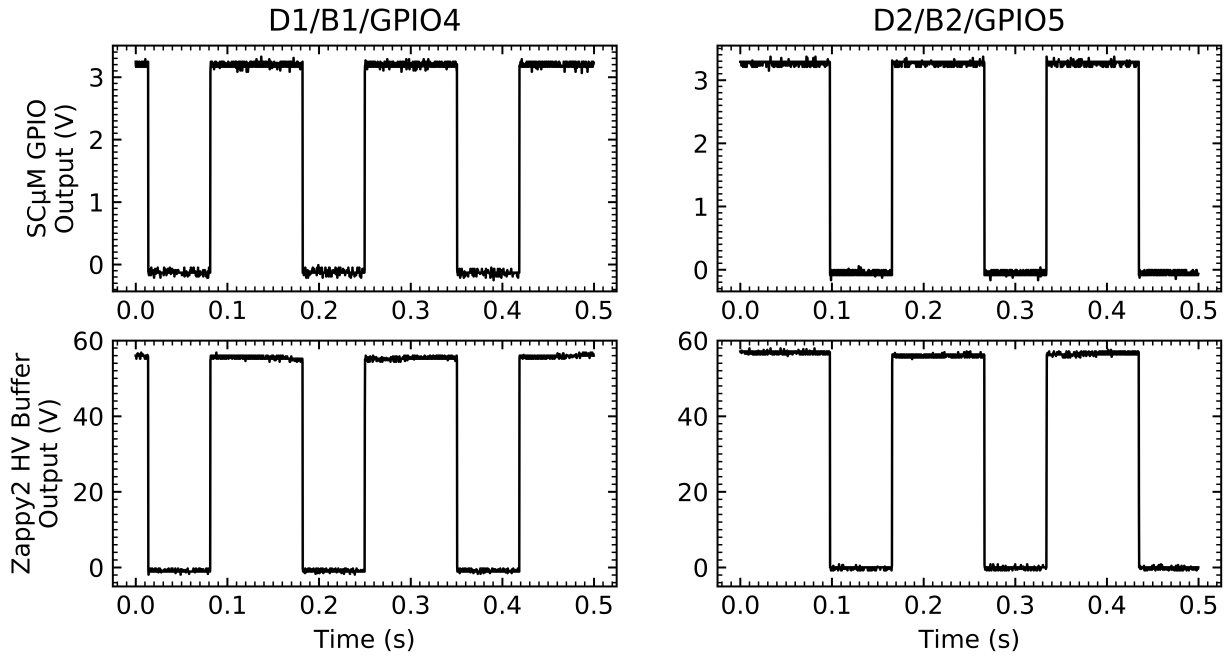

Figure 3.8: Toggling of HV buffers driving MEMS gripper at 200 mW/cm^2 irradiation. SCµM GPIO pins 4 and 5 are enabling/disabling 59 V HV buffered outputs D1 and D2 (respectively) on Zappy2. GPIOs toggling at 5.9 Hz with a 60 % duty cycle at a 180 degree phase offset from each other.

provided by the VBATPV supply. The I_{VDDIO}=1 µA consumed while toggling the GPIO pins at 160 Hz is well under the ~32 µA provided by the VDDIOPV source. Lastly, the VDDHPV current while toggling and actuating the gripper is on average ~4.75 µA, smoothed by a 100 nF capacitor.

Finally, SCµM returns to Phase ϕ_3 and begins listening for packets with "actuate gripper" commands. The gripper has been demonstrated to repeatedly open and close after multiple iterations of the receive-acknowledge-actuate loop.

Conclusion

Under conditions of steady 200 mW/cm^2 irradiation on Zappy2 we have demonstrated full SARA system operation. This includes receiving a six byte wireless command to actuate the gripper from a standard 2.4 GHz 802.15.4 transmitter, transmitting a ten byte standards-compatible 802.15.4 packet as an acknowledgement, and autonomous microprocessor-controlled MEMS gripper actuation. The gripper has then been demonstrated to fully close at a rate of 640 µm s^{-1} to close the full 3 mm distance in roughly 4.7 s. After the gripper has closed the SARA system successfully repeated the entire receive-acknowledge-actuate procedure repeatedly without failure.

The integrated SARA microsystem with power, control, and mechanical elements provides capabilities that previously would not be possible. An autonomous MEMS gripper could be used in micro assembly and manufacturing systems that require manipulation at a µm scale. Feedback control could be obtained by using the contact sensor on the MEMS gripper which could enable a µm scale caliper device to make size measurements of objects. Further developments will allow the integration of new jumping [80], walking [19], and fiber crawling [104] MEMS devices. For example, a MEMS inchworm motor could pull the SARA microsystem along a cord strung across an interior space to use SCµM as an autonomous, battery-free sensor. Multiple devices with SCµM and MEMS chips integrated could also be used in mesh networking systems for micro-scale robotic exploration.

3.2 Tracking Murderous Hornets with SCµM

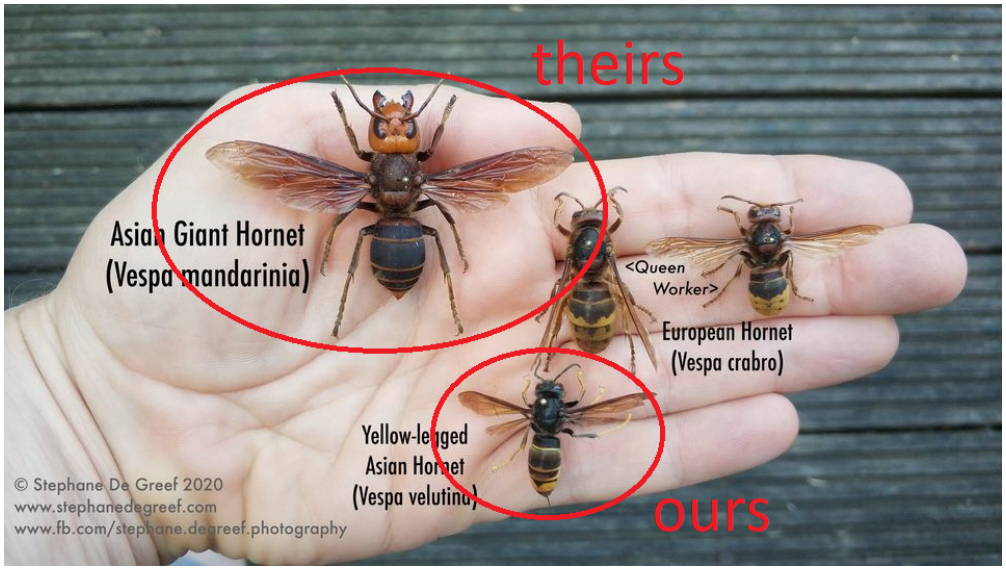

Figure 3.9: Comparison between various hornets [94]. [50] used Bluetooth tags developed by [35] to track the Asian giant hornet which is 2x bigger than the Asian hornet. However, this tag's size doesn't work well for tracking the Asian hornet. Thus, a BLE SCµM-based tag was created.

By accident the Asian hornet (Vespa Velutina) was introduced into Bordeaux, France in 2004. Without a predator, the species' population grew rapidly across Western Europe. Asian hornets typically invade honey bee nests, kill all the honey bees, and eat the larvae. As a result, western honey bee's halve their flight time leading to less nutrients and a colony reduction on average of 30% in France [43]. Many municipalities employ teams to kill the nests as soon as they are reported. While finding an Asian hornet is easy, outside of the bee hives, the challenge is finding their nest. For tracking Asian hornets VHF tags have been

Table 3.6: Weight Hornet Slayer Board

Item	Weight (mg)
Blank PCB	12.7
SCµM	4.3
Battery	162.8
Antenna	31.2
Wire for Battery & Solder	15.3
Epoxy	10
Solder for Antenna & Copper Tape	7.8
Total	244.1

used [43], however this requires special equipment. Bluetooth tags were used to track Asian giant hornets in [36, 35, 50] but the size difference does not work well for the 2x smaller Asian hornet.

In collaboration with Inria's EVA research team and Berkeley's Autonomous Microsystems Lab (BAMLAB), a BLE SCµM based hornet tracker came to life. Instead of requiring specialized readers or external RF sources to initiate backscatter communication SCµM hornet tracker could communicate with a wider range of existing devices like smartphones, tablets and computers. This led to building a tracker consisting of SCµM, a SR421SW silver oxide coin cell battery and a antenna as shown in Fig. 3.10.

Table 3.7: Specs for Hornet Slayer Board

Spec	Value
Dimensions	5x8mm
Weight	244.1 mg
Range	190 m
Battery Life	1.5 h

The fully assembled Hornet Tracker can be seen in Fig. 3.10. The 5x8 mm 2-layer flexible orange PCB has SCµM and its wirebonds in the middle enclosed with clear epoxy. The antenna can be see on the top right hand side with a length $\lambda/4$. The SR421SW coin cell battery can be seen at the bottom. A soldered wire seen sticking out on the left and right hand side of the board in combination with the copper tape was used to keep the battery in place. Originally, a battery holder was going to be used but according to [43] the weight requirements dictate it be under 280 mg. The weight breakdown can be seen in Table 3.6. The battery takes up the majority of the weight budget, followed by the antenna. After removing the battery holder, the total weight the Hornet Tracker was 244.1 mg which is well under the ideal 280 mg. The tracker has a battery life of 1.5 h and RSSI of -60 dBm within a meter of an OpenMote with a standard ducky antenna.

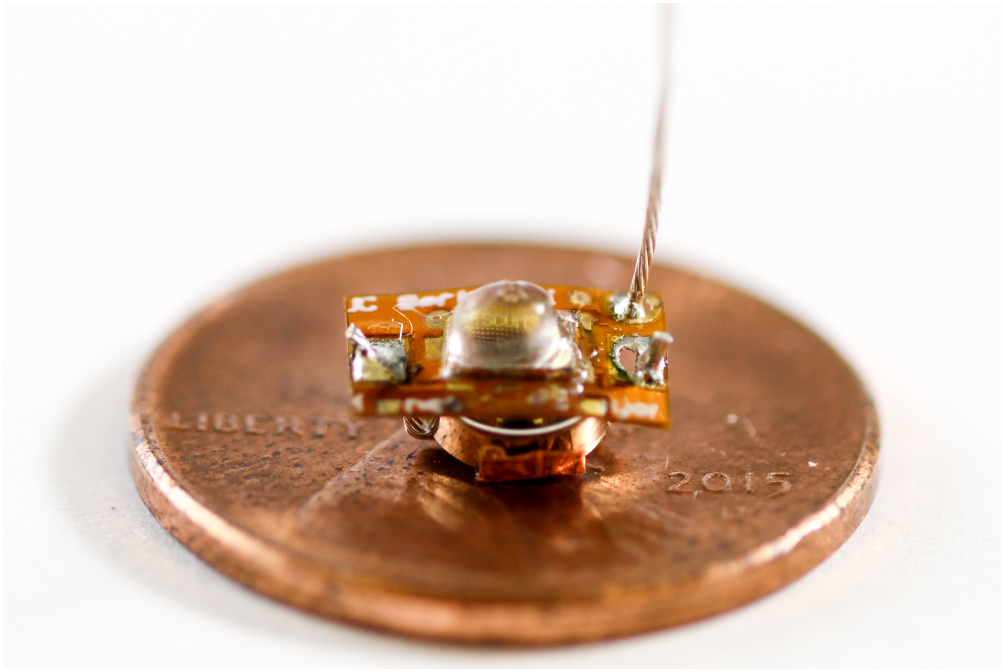

Figure 3.10: A fully assembled Hornet Tracker. The flexible lightweight orange PCB has SCµM in the middle under the clear epoxy bump and the antenna on the far right. The SR421SW coin cell battery was attached at the bottom by a soldered wire and copper tape.

The receiver for the Hornet Tracker was designed by the EVA team. The SCµM Hornet Tracker sends BLE beacon packets every 500 ms. The hardware for the receiver consisted of a Nordic nRF5340, a directional antenna with a gain of 14.5 dBi, and a speaker. For each frame that was received the speaker would play a beep. The pitch of the beep would depend on the signal strength of the frame (RSSI). The EVA team also began testing a drone based solution that could chase the hornet down.

With the fully assembled hornet tracker and receiver, the EVA team went to field to capture Asian hornets and attach the trackers. Fig. 3.11 shows the Hornet Tracker attached to the Asian hornet. For future work, a smaller weight profile and improved antenna design would be explored. The 68 mg battery discussed in [35] would be a good option to reduce the weight. An optimized antenna design could significant improve range and battery life considering SCµM is capable of outputting a -10 dBm RF signal from a standard rubber ducky antenna.

Figure 3.11: Tracker attached to Hornet [94]

3.3 Towards the The Small Autonomous Robot Actuator V2

After the completion of the compensation techniques in Section 2.2 and 2.3, the SCµM and Zappy2 integration was understood and could reliably communicate wirelessly to off-the-shelf components. SARA V1 was the next step in the integration effort which demonstrated reliable wireless actuation of a 15 mN MEMS gripper. With both of those initial challenges overcome, the next step was SARA V2 with a focus on designing even more compact microrobots.

SARAV2 is made of the same two core components SCµM and zappy2 and leverages the system operations $\phi_1 - \phi_5$ described in Sec. 3.1. The key difference is a MEMS Fiber Crawler (MFC) is the new mechanical component.

The MFC's original design was for inserting carbon fiber microelectrodes into brains for neural recording [105, 104]. The MFC was microfabricated in a two-mask silicon-on-insulator process with a 550 µm silicon substrate, a 2 µm buried oxide layer and a 40 µm device silicon layer. The MFC is 4.5x4.5 mm and the actuator area is approximately 1.5 mm^2. However, for SARAV2 the MFC was repurposed with the vision of having a microrobot that can crawl

Table 3.8: Weight comparison between SARA V1 vs SARA V2. There was a 61% reduction in weight. The biggest weight reduction came from replacing the MFC with the gripper. The new PCB's weight was also reduced by 50%. The last weight reduction came from replacing the 26.2 mg 0805 100 µF VBAT cap with an 3.2 mg 0402 22 µF cap since the compensation techniques in Sec. 2.3 made this possible. Note that the stacked SCµM weight mentioned in Table 3.1 was removed, and the 0402 capacitors are slightly lighter. The Solder&Wirebonds section was meant to account for any remaining weight. For SARA V1, it was roughly 3.1 mg including the small electrical tape that was used. The weight for SARA V2's Solder&Wirebonds section is likely lower because it didn't include the tape when measured.

Item	SARA V1 (mg)	SARA V2 (mg)
Blank PCB	71.8	36.1
SCµM	4.3	4.3
Zappy2	17.3	17.3
Fiber Crawler	X	22
Gripper	137.9	X
0402 Cap (22 µF)	3.8	3.2x2
0805 Cap (100 µF)	26.2	X
0805 Cap (100 nF)	17.2	17.2
Solder&Wirebonds	3.1	0.9
Total	281.6	104.2

Table 3.9: Size comparison between SARA V1 vs SARA V2 with a 55% reduction in area.

Item	SARA V1	SARA V2
Length (mm)	23.14	17.15
Width (mm)	9.0	5.44
Area (mm^2)	208.26	93.3

forward or backwards along a fiber.

In Table 3.9, SARA V2 is 55% smaller than SARA V1. A lot of that has to do with using a MFC and optimization for area. SARA V2's PCB is also 61% lighter than SARA V1 as shown in Table 3.8. Using a MFC instead of the Gripper provided a significant reduction in weight. SARA V2's PCB weight was cut by almost half. One last difference is the 0805 100 µF capacitor is no longer needed because of the compensation techniques discussed in Sec. 2.3. Thus, a 0402 22 µF capacitors was used instead

In Fig. 3.13, the fully assembled SARA V2 is shown. The individual pieces have been tested, SCµM, zappy2 and the MEMS device. Considering that SCµM and Zappy2 have already been shown to drive MEMS devices in SARA V1. The remaining piece is debugging SARA V2 fully integrated, demonstrating a fiber being pushing and last but not least the

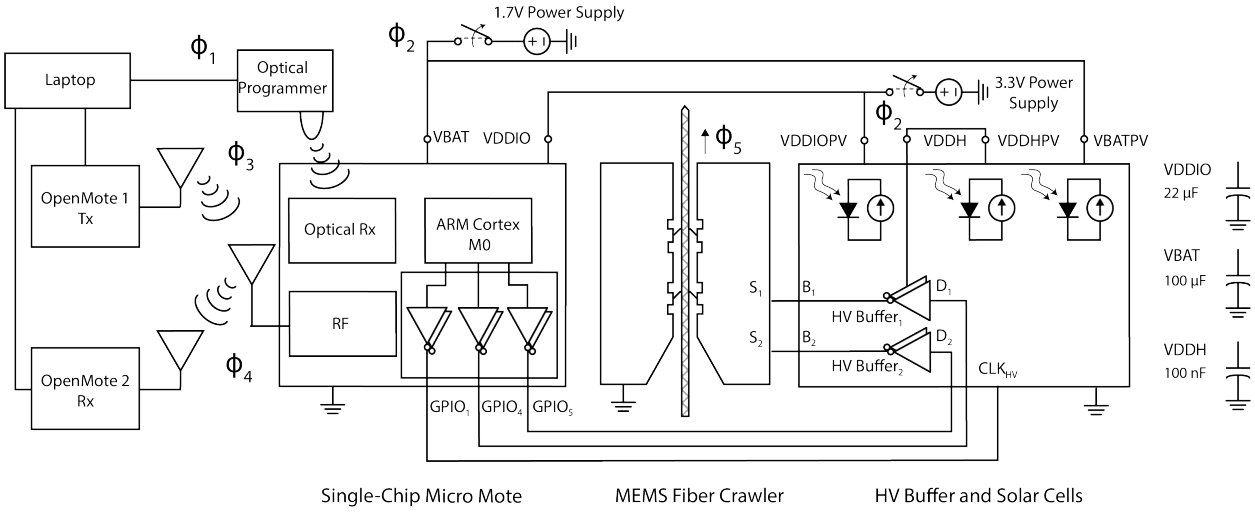

Figure 3.12: Schematic of SARAV2. From left to right, SCµM, the MFC, and Zappy2. SARAV2 uses the same $\phi_1 - \phi_5$ system operation used for SARAV1

entire microrobot crawling along a fiber. One last thing worth considering, MEMS electrostatic inchworm motors are prone to debris causing malfunction thus a cover would be ideal for this MFC.

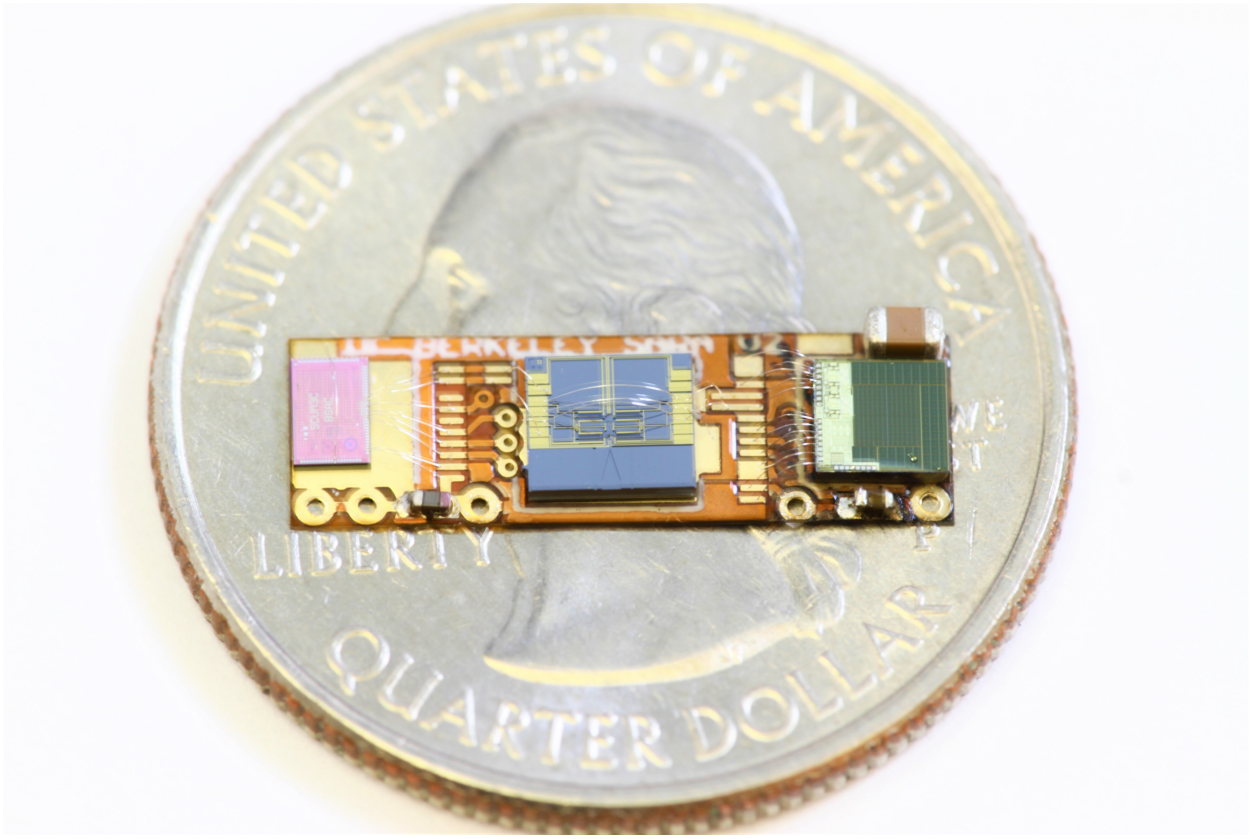

Figure 3.13: Assembled SARAV2. SCµM is the pink rectable on the far left, the MFC is in the middle and Zappy2 is on the far right. The 0805 100 nF capacitor is on the top right, and the two 0402 22 µF capacitors are seen on the bottom left and right.

3.4 Towards the Invisible Keyboard Invisible Keyboard

Shole's QWERTY keyboard was first created in 1873 and over the last 150 years it has dominated how people interact with computers, cellphones and tablets. Similarly, Engelbart created the first computer mouse in 1964 an for the past 59 years the form factor remains the same. There have been many attempts within the Berkeley Sensor and Actuator Center (BSAC) to change human computer interaction. One example is the Acceleration Sensing Glove from 1999 [68] seen in 3.14. The Ring GINA project from 2014 was another attempt [29]. It used off-the-shelf components to create a wireless ring sensor that registered gestures. Both of these were an evolution in technology to replace keyboards and mouse. However, due to the technology at that time they were bulky in size thus limiting mass adoption. This is where the next generation of IoT technology like SCµM, zappy2 and printed batteries can be used to create the Invisible Keyboard and push the the envelope for human computer interaction. As seen in Fig. 3.14, these components fit nicely on a penny.

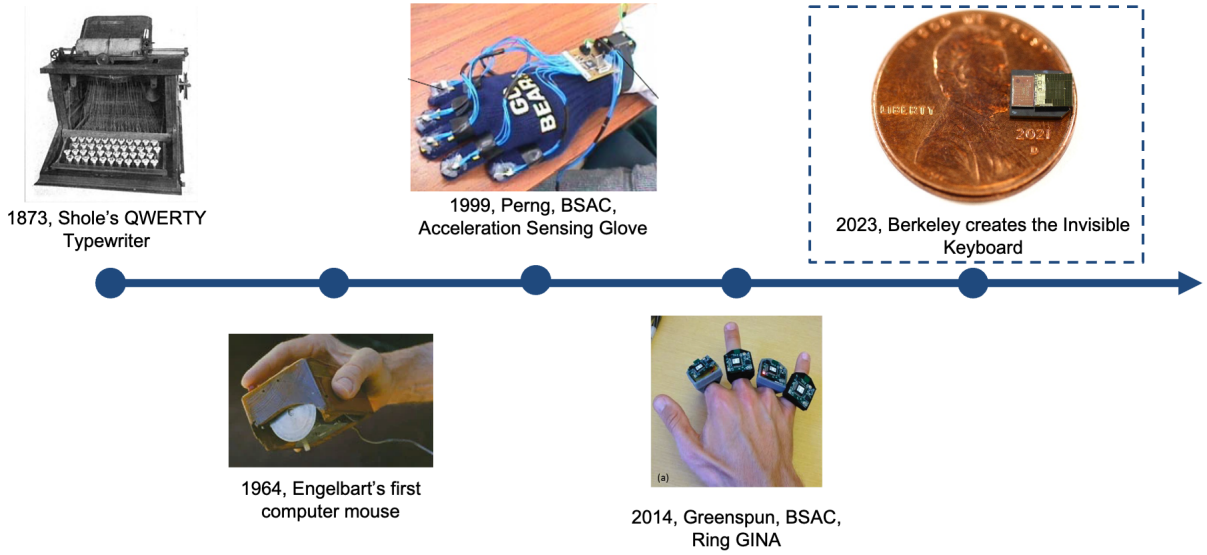

Figure 3.14: The vision for the Invisible Keyboard. Traditionally, keyboards and mice have been the main way to interface with computers. There have been many efforts to introduce new gesture-based technology to replace them such as the Acceleration Sensing Glove [68] and the Ring GINA project [29] but they were limited by the technology of the time. The creation of next-generation technology like SCµM allow those complex capabilities to fit on the tip of your fingernail paving the way for the Invisible Keyboard.

To begin, the Invisible Keyboard specifications are defined for the wireless sensor that would sit on each fingernail. The dimensions are based on [41] which states the smallest nail for a female is 9.8x8.8 mm with a standard deviation of 0.8 mm. Thus, the target size was set to 8x9 mm. For the weight, 100 mg is the target since acrylic nails can weigh anywhere from 200-500 mg. In 1.2, the printed lithium ion battery was shown to power SCµM for 13.6 h. Thus, the target battery life is 12 h. [45] discusses SCµM's 3D position tracking capabilities and position accuracy, which was was 15.4 mm, 15 mm and 51 mm for X, Y, Z, respectively. Thus, the target 3D position resolution is 50 mm.

Fig. 3.15 demonstrates a mock-up of the Invisible Keyboard's sensor. The observed dimensions measure roughly ~5.5x4 mm, significantly smaller than the target. Within the design the pink square indicates the placement of SCµM, while the blue square specifies where Zappy2 would go. The large gray square indicates where the printed LiPo battery would go assuming miniaturized packaging were complete.

Various pieces of this project have already been validated such as lighthouse localization [45], SCµM powered by a LiPo battery Sec. 1.2, energy harvesting from zappy2 [62, 63, 61]. Thus, the main challenge that remains for this project is miniaturizing the packaging for the LiPo battery, validating a miniaturized version of the sensor and optimizing the lighthouse localization algorithm. A stepping stone could be to use the 68 mg battery discussed in [35] and would require the DC-to-DC converter that was used in Sec. 1.2. However, given that

SCµMV2023 has an on-chip 4.1 V to 1.8 V switched capacitor converter, there may be no need for the external DC-to-DC converter. Whoever picks up this project, consider yourself lucky.

Table 3.10: Specs for Invisible Keyboard

Spec	Units	Value
Dimensions	mm	8x9
Weight	mg	100
Battery Life	h	12
Position Res	cm	<5

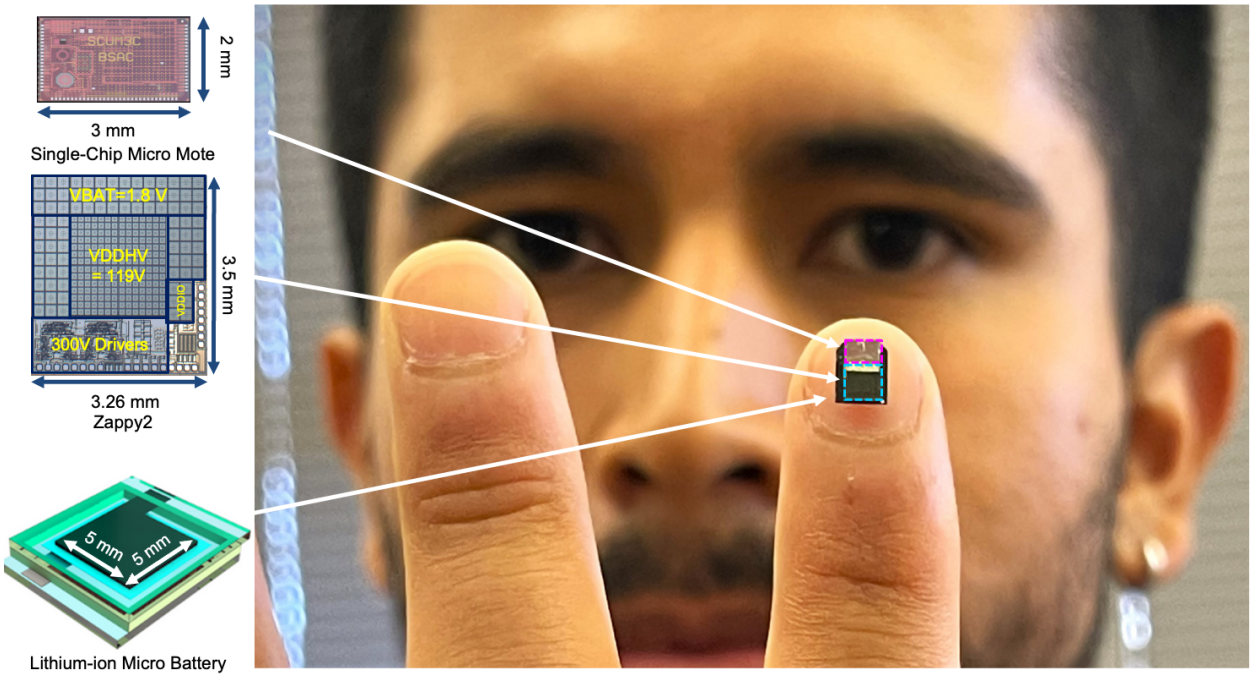

Figure 3.15: A mock up of how the Invisible Keyboard would look like.

Chapter 4

Towards MEMS Mirrors for Lighthouse Localization

This work aimed to design a resonant MEMS mirror (RMM) to be used in lighthouse localization which is able to locate objects in 3D space with millimeter precision. The RMM would be a replacement to the HTC Vive Lighthouse Beacon. A millimeter scale lighthouse beacon is desirable because microrobitic applications are limited by size, weight and power (SWaP) as shown in the untethered Small Autonomous Robot Actuator (SARA) [62] and the 10 mg robot built by Hollar et al. [32]. The RMM would be paired with a 3×2 mm, 4.2 mg crystal-free low power wireless SoC, the Single Chip micro Mote (SCµM), [53] which has demonstrated centimeter-resolution 3D localization [98, 45, 10]. The use of SCµM and RMMs would allow for the localization and navigation of swarms of millimeter scale walking [21], jumping [84], crawling [32], and flying [27] microrobots.

This chapter will discuss: what lighthouse localization and RMMs are (Section 4.1), how to design RMMs and the driving circuits (Section 4.2), how to operate the mirror (Section 4.3), and how three different RMM designs compare (Section 4.4).

4.1 Background

Lighthouse Localization

Lighthouse localization was originally designed for localizing smart dust [74]. Recently, HTC Vive's millimeter precision 3D lighthouse localization is used for virtual reality but has many other applications such as robotics, film, medicine and engineering [6]. The two main components in lighthouse localization are the lighthouse beacon and the photodiode detector. The lighthouse beacon's purpose is to emit infrared sync pulses and sweep in azimuth and elevation with a planar laser. The photodiode detector is meant to measure the time between the detected sync pulse and planar laser sweep pulse to find its azimuth and elevation relative to the lighthouse beacon. Two base stations are required to triangulate and

calculate the depth location of the photodiode detector [45]. The fundamentals of lighthouse localization are discussed in more detail in [98, 44, 45]. Assuming there is still a line of sight, lighthouse localization is attractive for locating swarms of microrobots because the computational complexity does not increase with the number of photodiode detectors. With SWaP in mind, a RMM would allow for microrobots to locate relative to one another with millimeter precision.

MEMS Micromirrors

Electrostatic MEMS micromirrors [66] have been demonstrated to have power consumption < 1mW in contrast to electrothermal and electromagnetic mircromirrors that consume power > 100mW [60, 102]. One of the first electrostatic mirrors [69] used electrodes under the mirror to create the out-of-plane motion but this limited the deflection angle due to the small gap between mirror and the electrode. For high deflection angles, it is essential to etch out the back substrate to not limit the deflection angle. There are many approaches to achieving out-of-plane torque, such as the angular comb drivers (AVC) [66] and comb drivers with upper and lower beams [57, 58].

[66] discusses the novel AVC drive actuator which allows for low power consumption, and $\pm 18^\circ$ of optical deflection for MEMS mirrors. In contrast to typical staggered vertical comb drivers, the angular vertical comb driver is self-aligned and can achieve a 50% higher scan angle. In order to create the AVCs the authors had to use thick photoresist to create hinges (9.5µm) for the moving comb. The MEMS mirror has one torsion bar and two AVCs on both sides along the x-axis. The moving comb of the AVC is attached to the torsion bars. When a large bias is applied the moving comb is pulled down. DC voltage is not sufficient to get the large deflections above, thus the MEMS mirror must be driven at resonance. They were able to get $\pm 18^\circ$ of optical deflection with a 21V sinusoidal input at 1.4kHz.

[59] discusses their two-axis gimbal-less 600µm MEMS mirror that uses comb drivers with upper and lower beams. Four orthogonally arranged vertical comb drivers were used to create the rotation. They connect to the MEMS mirror via mechanical linkages and mechanical rotation transformers, which allow up to 3 times more angle rotations. For their one-axis MEMS mirror they achieved optical deflection angles $> 50^\circ$ peak-to-peak at a resonant frequency of 4.447 KHz. For the two-axis MEMS mirror they achieved $\pm 20^\circ$ of optical deflection with a 20V pulsed waveform at resonant frequencies > 4.560 KHz.

While both of these approaches achieve both low power consumption and large deflection angles, they are designed with custom processes that are not easily replicated. RMMs offer similar optical deflection angles, scanning frequency and low power consumption needed for lighthouse localization while using a simple three mask process and a backside etch [79, 46].

4.2 System Design

The FOV, θ_{max} and f_{n} specs below are are based off of the HTC Vive lightouse beacon. The target power consumption is based off of the max power a miniature solar cell like Zappy2 [72] could deliver under one sun of illumination. The dimension specs were set to match the size of the 5x5 mm high capacity printed batteries [91] that have been shown to power SCµM while transmitting RF signals.

Table 4.1: Target Specifications

Spec	**Units**	**Value**
Power	µW	<240
Field of View (FOV)	deg	120
θ_{max}	rad	$\frac{\pi}{6}$
f_{n}	Hz	>120
Area	mm^2	$< 5\times5$
s_{res} @ $\rho = 1\text{m}$	mm	1

Fabrication

The RMM is designed for a simple three mask silicon on insulator (SOI) process. The device layer, oxide and substrate are 40µm, 2µm, and 550µm thick, respectively. In order to achieve the 60° of peak-to-peak mechanical deflection, the substrate layer below the comb fingers and MEMS mirror is etched out.

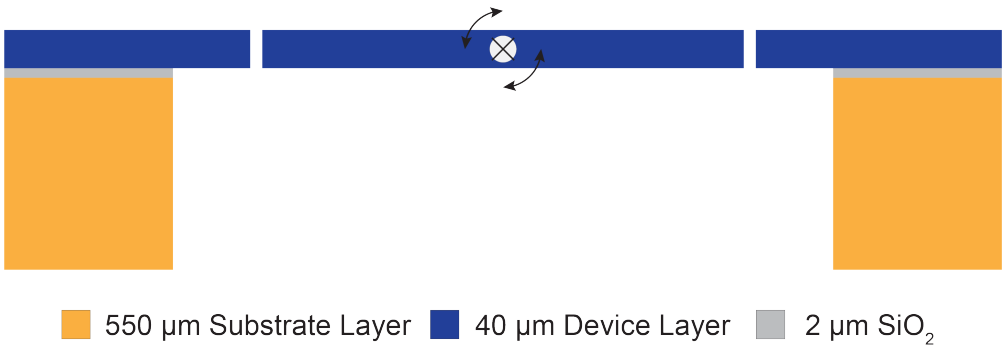

Figure 4.1: The RMM was designed in a 3 layer SOI process with a 40 µm device layer and 550 µm substrate layer. A backside deep reactive ion etch would be used to remove the substrate under the mirror and comb fingers to allow the mirror to rotate.

Resonant MEMS Mirror Theory and Design

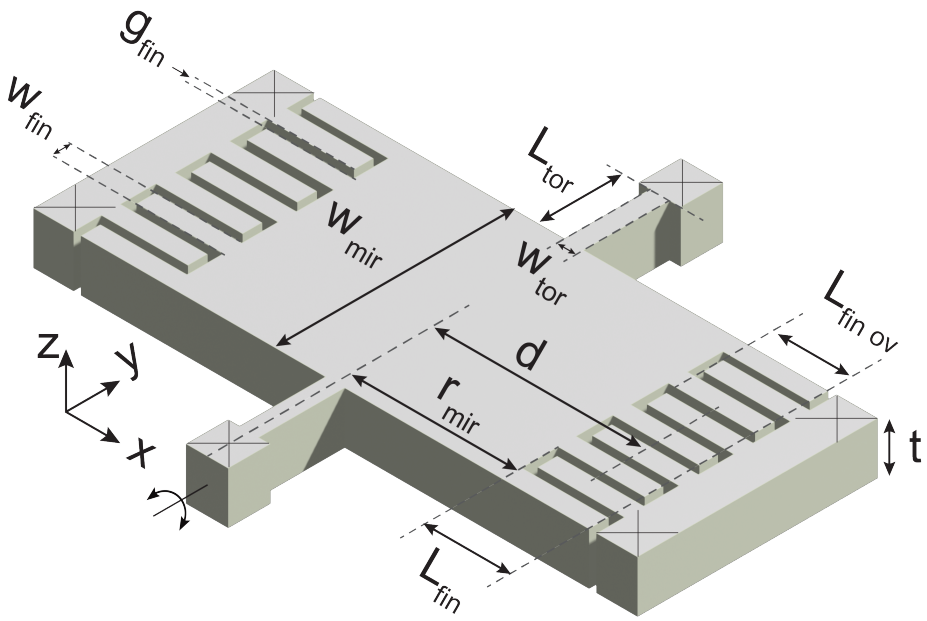

Figure 4.2: Resonant MEMS mirror diagram with labels

Moment of Inertia

Since the plate is significantly bigger than the comb fingers they will be ignored for the mass moment of inertia calculations.

$$I_{\text{mir}} = \frac{m((2r_{\text{mir}})^2+t^2)}{12} \tag{4.1}$$

Damping

Based on [46] the dominant form of damping should be through the fluidmechanical interaction in the comb fingers. Thus for this model, only couette flow is considered as a first order approximation of the damping moment. The damping not included, squeeze film and drag damping of the mirror plate, is discussed in [46]. While A_{ov}, the overlapping area of the comb fingers, does vary with θ for this first order approximation calculation it is assumed to be constant. As a result τ_{damping} will be more pessimistic and the energy lost per cycle will be higher as seen in Eq. (4.16). All input variables below are defined in Table 4.2.

Table 4.2: Description of variables. The top section is for input variables and constants while the bottom is for calculated values

Variable	Units	Description
L_{tor}	m	The length of the torsion spring
w_{tor}	m	The width of the torsion spring
r_{mir}	m	Radius of the MEMS mirror from the axis of rotation
w_{mir}	m	Width of the MEMS mirror
t	m	Thickness of the device layer
g_{fin}	m	The gap between two comb fingers
w_{fin}	m	The width of a comb finger
L_{fin}	m	The length of a comb finger
$L_{\text{fin ov}}$	m	The overlapping length between two comb fingers
E	Pa	The Young's modulus of silicon in the 110 orientation
G	Pa	The shear modulus of silicon in the 110 orientation
ε	F m^{-1}	The permittivity of free space
μ	Pa s	The viscosity of the fluid, viscosity of air in this case
I_{mir}	kg m^2	Mass moment of inertia of the MEMS mirror about the axis of rotation
m	kg	Mass of the MEMS mirror
τ_{inertia}	N m	Torque from the mass moment of inertia and angular acceleration
$\ddot{\theta}$	rad s^{-2}	Angular acceleration of the MEMS mirror about the axis of rotation
A_{ov}	m^2	The overlapping area of the comb fingers
d	m	The distance between the axis of rotation and the middle of the overlapping comb finger length
$\dot{\theta}$	rad s^{-1}	Angular velocity of the MEMS mirror about the axis of rotation
τ_{damping}	N m	Torque due to damping occurring at the comb fingers due to couette flow
k_θ	N m rad^{-1}	The torsion spring constant
J_{tor}	m^4	The area moment of inertia of the torsion spring
θ	rad	The angle between the x-axis and the MEMS mirror
τ_{tor}	N m	Torque due to the torsion spring
C_{comb}	F	The total capacitance for all the comb fingers on one side
N_{g}	unitless	The total number of gaps on one side of the mirror
θ_{c}	rad	The angle at which the comb fingers no longer overlap
V_{ext}	V	Voltage between the comb fingers
τ_{ext}	N m	Torque due to the electrostatic forces
ω_{n}	rad	The resonant frequency

$$b(\theta) = \frac{\mu A_{\text{ov}}(\theta)}{g_{\text{fin}}} \tag{4.2}$$

$$d = \left(r_{\text{mir}} + L_{\text{fin}} - \frac{L_{\text{fin ov}}}{2} \right) \tag{4.3}$$

$$\tau_{\text{damping}} = N_g b d^2 \dot{\theta} \tag{4.4}$$

Torsion Spring

J_{tor} is the polar moment of inertia for the torsion spring rotating about the y-axis (Fig. 4.2).

$$\tau_{\text{tor}} = k_\theta \theta \tag{4.5a}$$
$$= \frac{J_{\text{tor}} G}{L_{\text{tor}}} \theta \tag{4.5b}$$
$$= \frac{1}{12}(t^3 w_{\text{tor}} + t w_{\text{tor}}^3) \frac{G}{L_{\text{tor}}} \theta \tag{4.5c}$$

Electrostatic Torsion

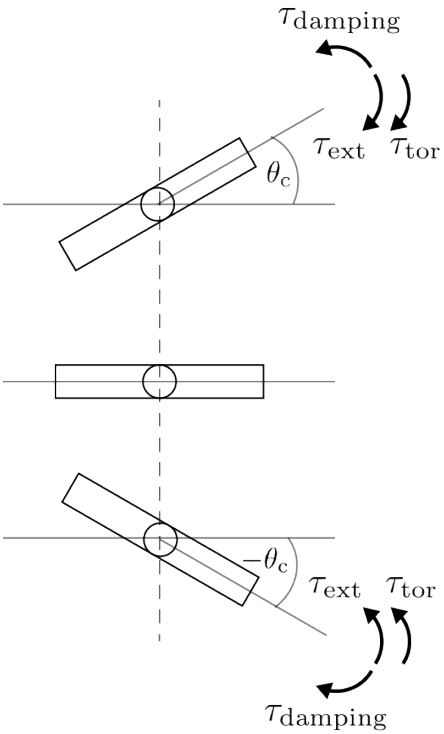

Figure 4.3: Free-body diagram of the RMM. $+\theta$ is counterclockwise. The top diagram shows the mirror plate entering the comb fingers from the top, $\theta \leq \theta_{\text{c}}$ and $\dot{\theta} < 0$, while the bottom diagram shows it entering the comb fingers from the bottom, $\theta \geq -\theta_{\text{c}}$ and $\dot{\theta} > 0$.

In order to stay at resonance this system needs an external torque to compensate for energy lost due to damping. This torque is generated through the electrostatic forces between the comb fingers when voltage is applied between them. Thus, the torque is dependent on the total capacitance in the comb structure. At $\theta = 0$, as can be seen in Fig. 4.2, the maximum capacitance, C_{max}, occurs because $A_{\text{ov}}(0)$ reaches its maximum. A pair of fingers

can be viewed as a standard parallel plate capacitor where the area is defined by the fingers' overlap, L_{ov}, and device layer thickness, t (Fig. 4.2). To calculate the total capacitance for one side of the RMM the capacitance of pair of comb fingers is multiplied by the number of gaps on one side resulting in Eq. (4.6). To approximate how A_{ov} varies with θ we assume a linear relationship between C_{comb} and θ which results in Eq. (4.7). Neglecting fringing forces, θ_c is defined as the angle where the fingers no longer overlaps, $A_{\text{ov}} = 0$, thus $C_{\text{comb}} = 0$ for $|\theta| > \theta_{\text{c}}$. θ_c can be calculated using geometry and trigonometry resulting in Eq. (4.8).

$$C_{\max} = \frac{\varepsilon L_{\text{fin ov}} t}{g_{\text{fin}}} N_g \tag{4.6}$$

$$C_{\text{comb}}(\theta) = \begin{cases} 0 & |\theta| > \theta_{\text{c}} \\ \frac{C_{\max}}{\theta_{\text{c}}}(\theta + \theta_{\text{c}}) & -\theta_{\text{c}} \leq \theta \leq 0 \\ \frac{C_{\max}}{\theta_{\text{c}}}(-\theta + \theta_{\text{c}}) & 0 \leq \theta \leq \theta_{\text{c}} \end{cases} \tag{4.7}$$

Using D'Alembert's principle, τ_{ext} can be calculated resulting in Eq. (4.10). Eq. (4.12), shows the moments acting on the mirror for various θ and $\dot{\theta}$ conditions. This equation is a piecewise function because of $C_{\text{comb}}(\theta)$ and $V_{\text{drive}}(\theta)$ are both functions of θ. $V_{\text{drive}}(\theta)$ is only supposed to be applied when the mirror is approaching $\theta = 0$ as seen in Fig. 4.5.

$$\theta_c = 2\arctan\frac{\frac{1}{2}t}{r_{\text{mir}} + L_{\text{fin}} - L_{\text{fin ov}}} \tag{4.8}$$

$$U(\theta) = \frac{1}{2} C(\theta) V_{\text{ext}}^2 \tag{4.9}$$

$$\tau_{\text{ext}} = \frac{\mathrm{d}}{\mathrm{d}\theta} U(\theta) = \frac{1}{2} V_{\text{ext}}^2 \frac{\mathrm{d}C_{\text{comb}}(\theta)}{\mathrm{d}\theta} \tag{4.10}$$

$$\tau_{\text{total}} = I_{\text{mir}} \ddot{\theta} = \sum_{\text{i}} \tau_{\text{i}} = -\tau_{\text{damping}} - \tau_{\text{tor}} - \tau_{\text{ext}} \tag{4.11}$$

$$I_{\text{mir}} \ddot{\theta} = \begin{cases} -k_\theta \theta & |\theta| > \theta_{\text{c}} \\ -b(\theta) d^2 \dot{\theta} - k_\theta \theta - \frac{1}{2} V_{\text{ext}}^2 \frac{C_{\max}}{\theta_c} & 0 \leq \theta \leq \theta_{\text{c}},\ \dot{\theta} < 0 \\ -b(\theta) d^2 \dot{\theta} - k_\theta \theta & -\theta_{\text{c}} \leq \theta < 0,\ \dot{\theta} < 0 \\ -b(\theta) d^2 \dot{\theta} - k_\theta \theta + \frac{1}{2} V_{\text{ext}}^2 \frac{C_{\max}}{\theta_c} & -\theta_{\text{c}} \leq \theta \leq 0,\ \dot{\theta} \geq 0 \\ -b(\theta) d^2 \dot{\theta} - k_\theta \theta & 0 < \theta \leq \theta_{\text{c}},\ \dot{\theta} \geq 0 \end{cases} \tag{4.12}$$

Resonant Frequency

The resonance frequency can be calculated using Eq. (4.13) since this is a torsion spring mass system.

$$\omega_{\text{n}} = \sqrt{\frac{k_\theta}{I_{\text{mir}}}} \tag{4.13}$$

Energy per cycle

Energy gain and loss calculations below are calculated for one period of time where the mirror travels from $\theta_{\max} \rightarrow -\theta_{\max} \rightarrow \theta_{\max}$.

$$\frac{\mathrm{d}U}{\mathrm{d}\theta} = \frac{\mathrm{d}C_{\mathrm{comb}}}{\mathrm{d}\theta}\frac{V_{\mathrm{ext}}^2}{2} \tag{4.14}$$

$$U_{\mathrm{gain}} = \frac{V_{\mathrm{ext}}^2}{2}\left(\int_{\theta_c}^{0}\frac{-C_{\max}}{\theta_c}d\theta + \int_{-\theta_c}^{0}\frac{C_{\max}}{\theta_c}d\theta\right) = V_{\mathrm{ext}}^2 C_{\max} \tag{4.15}$$

$$U_{\mathrm{loss}} = \frac{4\theta_c \mu A_{\mathrm{ov}}(\theta) d^2}{g_{\mathrm{fin}}}\dot{\theta} \tag{4.16}$$

We assumed $\dot{\theta} = \theta_{\max}\omega_n$ is constant for $-\theta_c < \theta < \theta_c$ and set $U_{\mathrm{gain}} = U_{\mathrm{loss}}$ to solve for $\theta_{\max}$, Eq. (4.17). This equation is likely off from the actual value since we assumed angular velocity was constant and that A_{ov} was constant.

$$\theta_{\max} = \frac{V_{\mathrm{ext}}^2 \varepsilon}{2\mu d^2}\frac{1}{2\theta_c \omega_n} \tag{4.17}$$

Thermal Noise

To calculate the RMS angular deflection due to the thermal noise in the torsion springs, $\overline{\theta}_{\mathrm{n}}$, we assume that the resonance quality factor, Q, is large and use the equipartition resulting in Eq. (4.18). We are interested in finding $\overline{\theta}_{\mathrm{n}}$ to know how much deflection is occurring in the mirror without V_{ext} and to calculate the the current due to thermal noise, $\overline{i}_{\mathrm{n}}$ that will show up in the sensing circuit.

$$\overline{\theta}_{\mathrm{n}} = \sqrt{\frac{k_B T}{k_\theta}} \tag{4.18}$$

Power Estimate

Energy required to charge one comb finger pair in one period is calculated in Eq. (4.19). C_{p} is the parasitic capacitance between the device layer and the substrate. We acknowledge C_{p} will increase power consumption but we ignore it since this is a first order approximation. A factor of 2 is introduced in Eq. (4.20) because there are two comb finger pairs.

$$U_{\mathrm{drawn}} = 2(C_{\max}+C_p)V_{\mathrm{ext}}^2 \tag{4.19}$$

$$\begin{aligned} P &= 2\frac{U_{\mathrm{drawn}}}{t_{\mathrm{per}}} \\ &= \frac{4(C_{\max}+C_p)V_{\mathrm{ext}}^2}{t_{\mathrm{per}}} \\ &= 4(C_{\max}+C_p)V_{\mathrm{ext}}^2\frac{\omega_n}{2\pi} \end{aligned} \tag{4.20}$$

Arc Length Resolution

Assuming the motion of the mirror will be sinusoidal the worst angular resolution will occur at $\theta = 0$ when $\dot{\theta}_{\max} = \theta_{\max}\omega_n$. As seen in Table 4.1, the target arch length resolution is $s_{\text{res}} = 1\text{mm}$ at a radius of $\rho = 1\text{m}$. This assumes that the optical receiver such as SCµM and this RMM would be spaced by one meter. f_{sample}, Eq. 4.22, specifies the minimum sampling frequency the optical receiver would need to achieve at least $s_{\text{res}} = 1\text{mm}$ at a radius of 1 m.

$$s_{\text{res}} = \rho\theta_{\max}\omega_n t_{\text{sample}} \tag{4.21}$$

$$f_{\text{sample}} = \frac{\theta_{\max}\omega_{\text{n}}}{\theta_{\text{res}}\rho} \tag{4.22}$$

Torsional Fracturing

The torsion springs are at risk of fracturing from the FOV target spec of 120° thus $\theta_{\text{max fracture}}$ was calculated, Eq. (4.23). $\epsilon_{\max} = 0.01$ is the max strain for silicon in the 110 orientation.

$$\theta_{\text{max fracture}} = \frac{\epsilon_{\max} L_{\text{tor}}}{w_{\text{tor}}} \tag{4.23}$$

Lateral and Vertical Fracturing and Displacement

Since the torsion springs are free to bend along the x and z axis, the maximum g-force, $g_{\max}$, the springs can tolerate was calculated, Eq. (4.26). $g = 9.8\text{m}\cdot\text{s}^{-2}$

$$I_{\text{x}} = \frac{t_{\text{tor}}^3 w_{\text{tor}}}{12} \tag{4.24}$$

$$I_{\text{z}} = \frac{t_{\text{tor}} w_{\text{tor}}^3}{12} \tag{4.25}$$

$$g_{\max} = \frac{2\epsilon_{\max} EI}{g\frac{L_{\text{tor}}}{2}\frac{t}{2}} \tag{4.26}$$

Comb Clearance

The clearance between the comb fingers, $L_{\text{fin}} - L_{\text{fin ov}}$, was checked so that they did not collide as the RMM rotated out of plane.

$$r_{\text{mir h}} = \sqrt{r_{\text{mir}}^2 + \frac{t}{2}^2} \tag{4.27}$$

$$L_{\text{fin}} - L_{\text{fin ov}} > L_{\text{clearance}} = r_{\text{mir h}} - r_{\text{mir}} \tag{4.28}$$

Driving Circuit Theory and Design

Given the symmetry of the RMM, startup is a concern which leads to RMMs typically having a startup electrode [79]. However, according to [79] oscillation can be started if the mirror is driven by a fixed frequency voltage signal near resonance since the asymmetries introduced through fabrication processes are enough to allow the RMM to be kicked out of equilibrium.

While the RMM can be driven by an external fixed frequency voltage signal, this does not work well as resonant frequency changes with environmental factors. [92]. To resolve this issue, synchronized excitation[75, 92] is used to sense when the mirror is at $\theta = 0$ and turn off the driving voltage.

For the driving circuit for this RMM, two separate ways were included to drive the mirror with either fixed driving frequency or synchronized excitation. The fixed driving frequency circuitry is at the top of Fig. 4.4. It is composed of an oscillator, f_{LO}, followed by a frequency divider that connects to a MUX that can route it to a high voltage buffer that drives the RMM. The synchronized excitation circuitry is designed to sense current to determine when the mirror is at $\theta = 0$ and can be seen at the bottom section of Fig. 4.4. A current, i_{pulse}, would be converted into a voltage by the transimpedance amplifier (TIA). The output is followed by a buffer that drives the Sample & Hold (S&H) circuits in the store and threshold branch. The store branch is meant to find the maximum voltage generated by the mirror and the accompanying local oscillator tuning setting, $\mathrm{TN}_{\mathrm{LO}}$. The threshold branch is supposed to set its DAC settings such that $\mathrm{FL}_{\mathrm{threshold}}$ goes high only when i_{pulse} is positive as seen in Fig. 4.5.

To calculate i_{pulse} we assume $\dot{\theta} = \theta_{\max}\omega_n$ is constant for $-\theta_c < \theta < \theta_c$ and that the RMM is at resonance. This allows us to calculate t_{pulse} which is how long i_{pulse} is expected to stay high as the mirror travels from $\theta_c \to 0$ or $-\theta_c \to 0$ as depicted in Fig. 4.5.

$$t_{\mathrm{pulse}} = \frac{\theta_{\mathrm{c}}}{\theta_{\max}\omega_{\mathrm{n}}} \tag{4.29}$$

$$i_{\mathrm{pulse}} = V\frac{\mathrm{d}C}{\mathrm{d}t} = \frac{2VC_{\max}\theta_{\max}\omega_n}{\theta_c} \tag{4.30}$$

$$\bar{i}_{\mathrm{n}} = \frac{2VC_{\max}\bar{\theta}_{\mathrm{n}}\omega_n}{\theta_c} \tag{4.31}$$

4.3 System Operation

The RMM will be driven at startup by the divided down oscillator signal until the resonant frequency is found. Once the RMM is resonating and the initial calibration is complete, the finite state machine will drive the RMM in synchronized excitation mode. The MUX is used to switch between the fixed frequency and synchronized excitation signals.

Startup

D_{mode} will be set such that the MUX outputs the divided down f_{LO}, the frequency of the local oscillator, to drive the high voltage buffer that drives the mirror as seen at the top of Fig. 4.4. Note that all of the S&H circuits and comparators are reset to GND at the beginning and i_{pulse} is converted to V_{pulse} by the TIA. To kick the RMM out of equilibrium, it will be driven at a fixed frequency higher than the expected resonant frequency and swept down to find f_n as described in [79]. TN_{LO}, the frequency tuning bits of the oscillator, will be swept from its max frequency setting to its lowest. During this sweep, the comparator in the store branch in Fig. 4.4 will be used to determine if latest V_{pulse1} is bigger than the V_{max} currently stored in the sample and hold circuit (S&H). If $V_{pulse1} > V_{max}$ is true then the output of the comparator, FL_{store}, will go high. Because FL_{store} connects to the clock of the bottom S&H in the store branch, V_{pulse1} will be clocked in as the latest V_{max}. TN_{LO} values will also be stored as the current best tuning bits for maximum deflection. After the swept is complete the TN_{LO} values are assumed to be driving the mirror at $\sim f_n$ and $\sim\theta_{max}$.

Calibration for $V_{threshold}$

We are interested in finding $V_{threshold}$ so we can synchronize when to turn V_{drive} on and off with $\theta > \theta_c$ and $\theta = 0$, respectively, as shown in 4.5. To find $V_{threshold}$, the TN_{LO} settings that were found in section 4.3 are used to set RMM at $\sim f_n$ which causes $V_{pulse} = \sim V_{max}$ every cycle. The TN_{DAC} values will then be swept from their max output voltage setting down until $V_{pulse} > V_{threshold}$. This will cause the comparator's output, $FL_{threshold}$ to go high meaning we found the TN_{DAC} values for $V_{pulse} > V_{threshold}$. Now that we have found $V_{threshold}$, $FL_{threshold}$ can be used to trigger V_{drive}.

Synchronization Mode

Switching between fixed driving frequency to synchronization mode is done through the D_{mode} MUX control signal. While D_{mode} can technically be switched whenever $|\theta| > \theta_c$, it is switched on the falling edge of $FL_{threshold}$ because it provides timing headroom of roughly $t_{headroom} = t_{period} - t_{pulse}$.

Calibration for t_{drive}

If the system were to be left as is V_{drive} would follow the positive step of i_{pulse}, thus setting $t_{drive} = \frac{t_{per}}{2} - t_{pulse} + t_{error}$. However, since the synchronization of the system is limited by a finite response and rise time having the rising edge of V_{drive} before the rising edge of i_{pulse} is desirable. This can be achieved by putting a counter following $FL_{threshold}$. Assuming the mirror is at resonance there should be a repeating set number of 1s and 0s that are spaced by the clocking period. The number of 0s in between 1s can be used to set t_{drive} such that

V_{ext} goes high one clock period before i_{pulse} is expected to go high. t_{drive} can tuned such that V_{ext} goes high approximately where $\theta_{\max}$ occurs as demonstrated in Fig. 4.5.

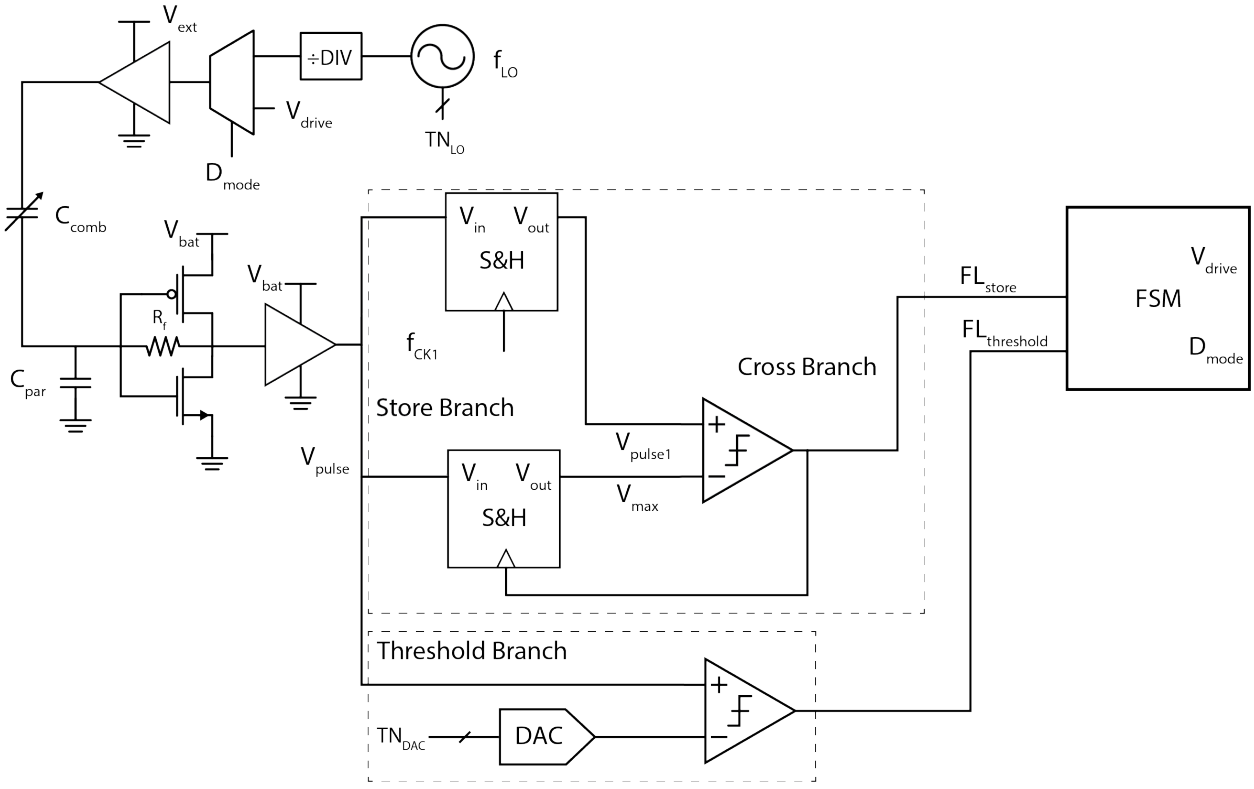

Figure 4.4: Drive Circuit

4.4 Simulation Results

All simulations were done using MATLAB's ordinary differential solver 45. Layout was automated using a MATLAB script to sweep L_{tor}, $L_{\text{fin ov}}$, r_{mir} and w_{mir}. The code can be found at the link that follows if you don't have access feel free to email me `moreno@berkeley.edu`

`https://berkeley.box.com/s/btuh0n4jv0bqhzd5xdilaixe6han84bz`

Below are the specs for three different voltage designs, 20V, 50V and 100V. While these [79, 59, 66] electrostaic MEMS mirrors were designed for $V_{\text{ext}} = 20$V, these RMMs were designed for $V_{\text{ext}} = 20$V, 50 V and 100 V since [62] demonstrated that Zappy2 [72], a 3.26× 3.5mm^2 high-voltage level shifter and solar cell, could be used to drive a 15mN MEMS gripper at 60 V under 2 suns of illumination. Zappy2 could drive devices up to 300V with external power.

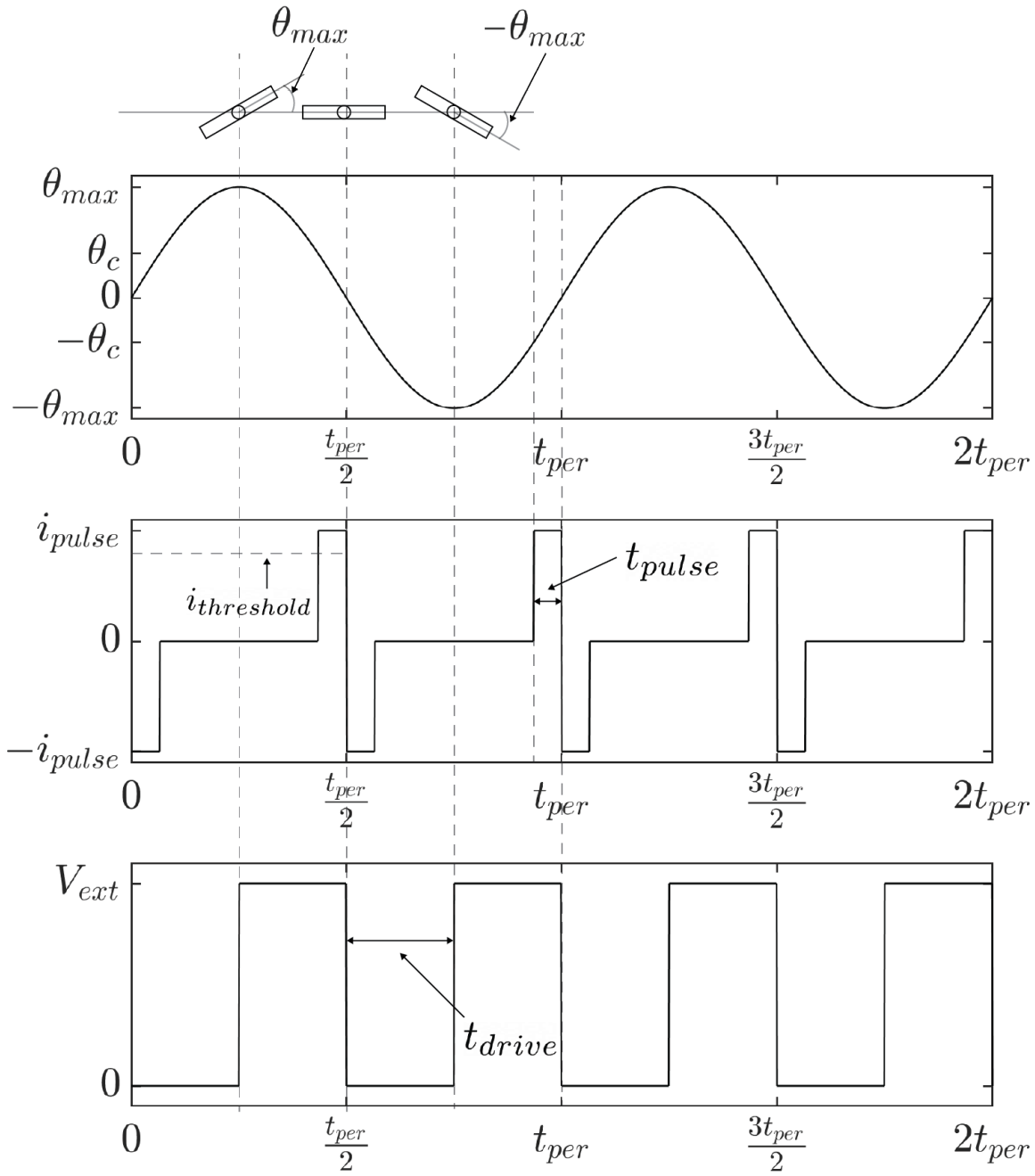

Figure 4.5: There are two key requirements: $V_{\text{drive}} = 0$ when $\theta = 0$ and $V_{\text{drive}} = V_{\text{ext}}$ when $\theta = \theta_{\text{max}}$.

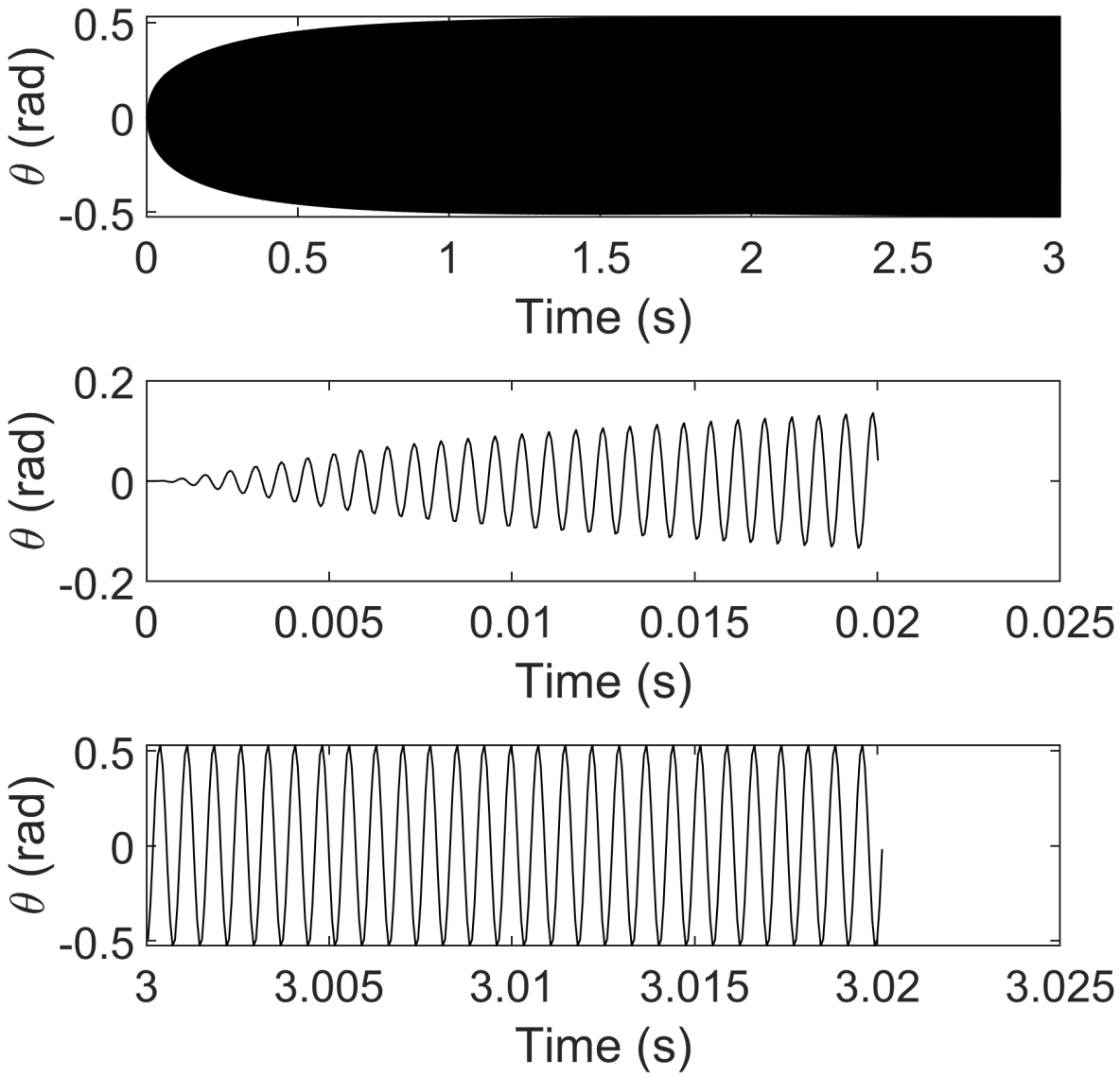

Figure 4.6: Transient simulation of the 50 V RMM Design using ODE 45

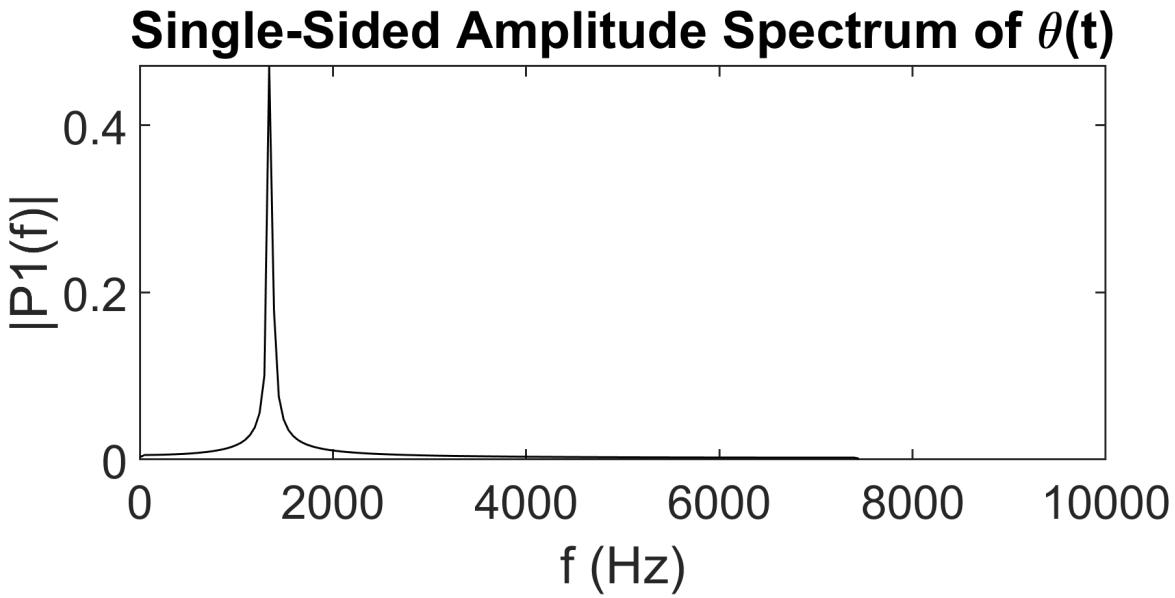

Figure 4.7: FFT of $\theta(t)$ for the 50 V RMM Design ODE 45 output. f_{n} = ~1353Hz

At V_{ext} = 20V, the mirror plate dimensions were increased until the area < 5×5mm^2 limit was reached. As can be seen in Table. 4.3, FOV = 67°, f_{sample} = 315kHz, and power = 3µW. It is not possible to reach an FOV > 120° without either increasing area > 5×5mm^2 and f_n < 120Hz. This occurs because by increasing the plate dimensions we are decreasing ω_{n} which will increase θ_{max} according to Eq. (4.17). While FOV is not greater than 120°, this design benefits from having a lower f_{sample}, f_{CK1} and power consumption compared to the two other designs. A lower f_{sample} and f_{CK1} reduces the clocking requirement for the optical receiver and driving circuit, respectively. This also means that if $f_{sampling}$ = 5MHz the 20 V design would have a s_{res} = 63µm while the 100 V design would only have a s_{res} = 7.8mm. Power consumption for this 20 V design is ~650 times lower than the 100 V design. One challenge with this design is that i_{pulse} = 0.6µA which requires higher gain in the TIA seen in Fig. 4.4.

All the comparisons below will be relative to the 20 V design. For the 50 V design, FOV > 120 was achieved while reducing the area of the mirror by ~75 %. i_{pulse} = 6.4µA which reduces the TIA gain requirement by ~10 times. Among the drawbacks, f_{n} is 8 times bigger which results in the power consumption being 27 times bigger and the minimum required f_{sample} on the optical receiver being 15 times bigger.

The 100 V design hits the desired FOV > 120° with ease since $\theta_{\text{max}} \propto V_{\text{ext}}^2$. As a result, area was reduced by ~93%. The mirror plate being smaller is a requirement because if it were any bigger then the torsional spring would fracture, $\theta_{\text{max}} > \theta_{\text{max fracture}}$. A primary concern with this design is that the power consumption increased by ~650 times almost consuming 2 mW. A few other things worth considering is that the minimum required f_{sample} = ~39MHz is ~125 times bigger. This means low power optical receiver SOCs like SCµM wouldn't be

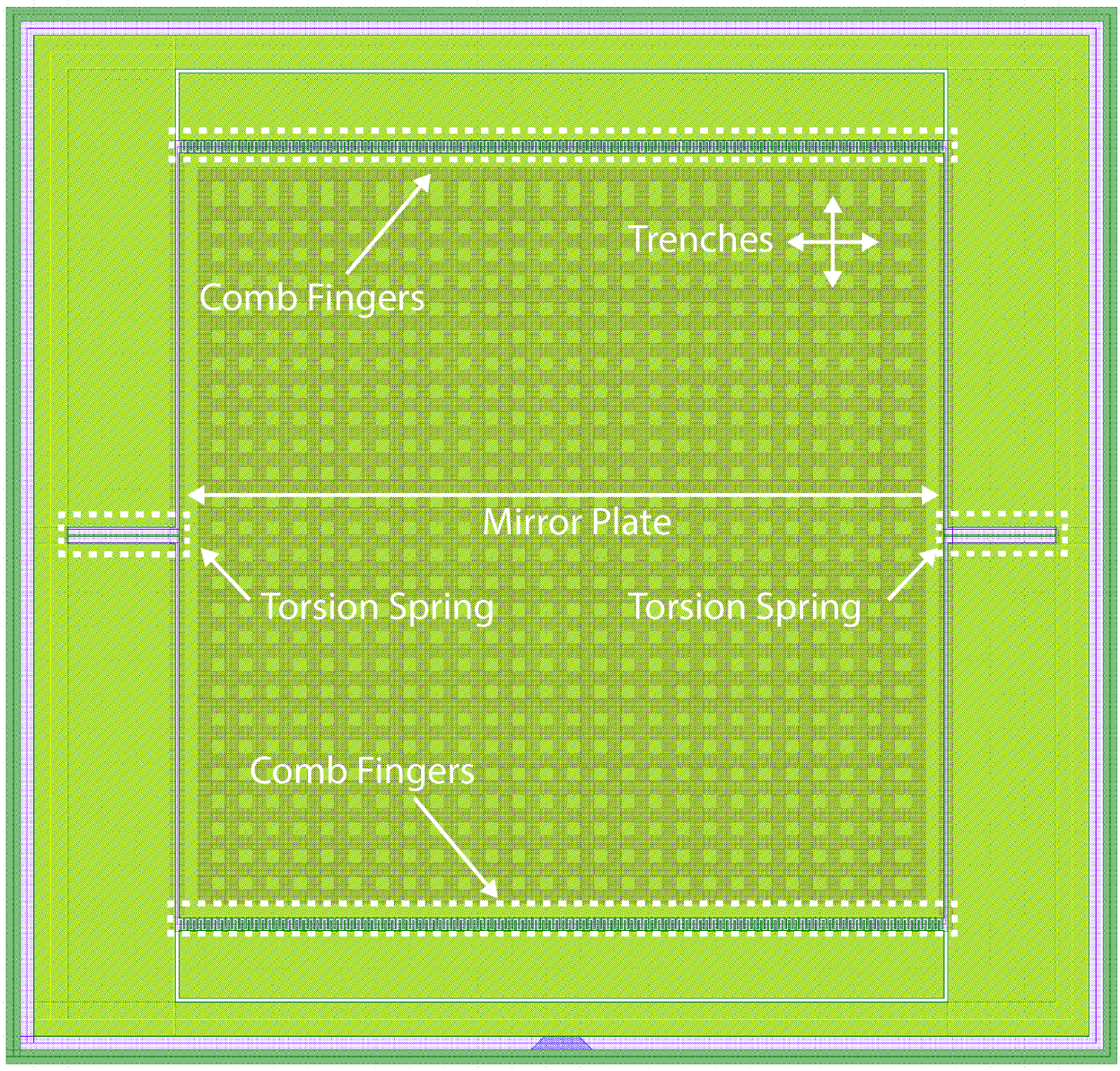

(a) MEMS mirror with HASH Trenches

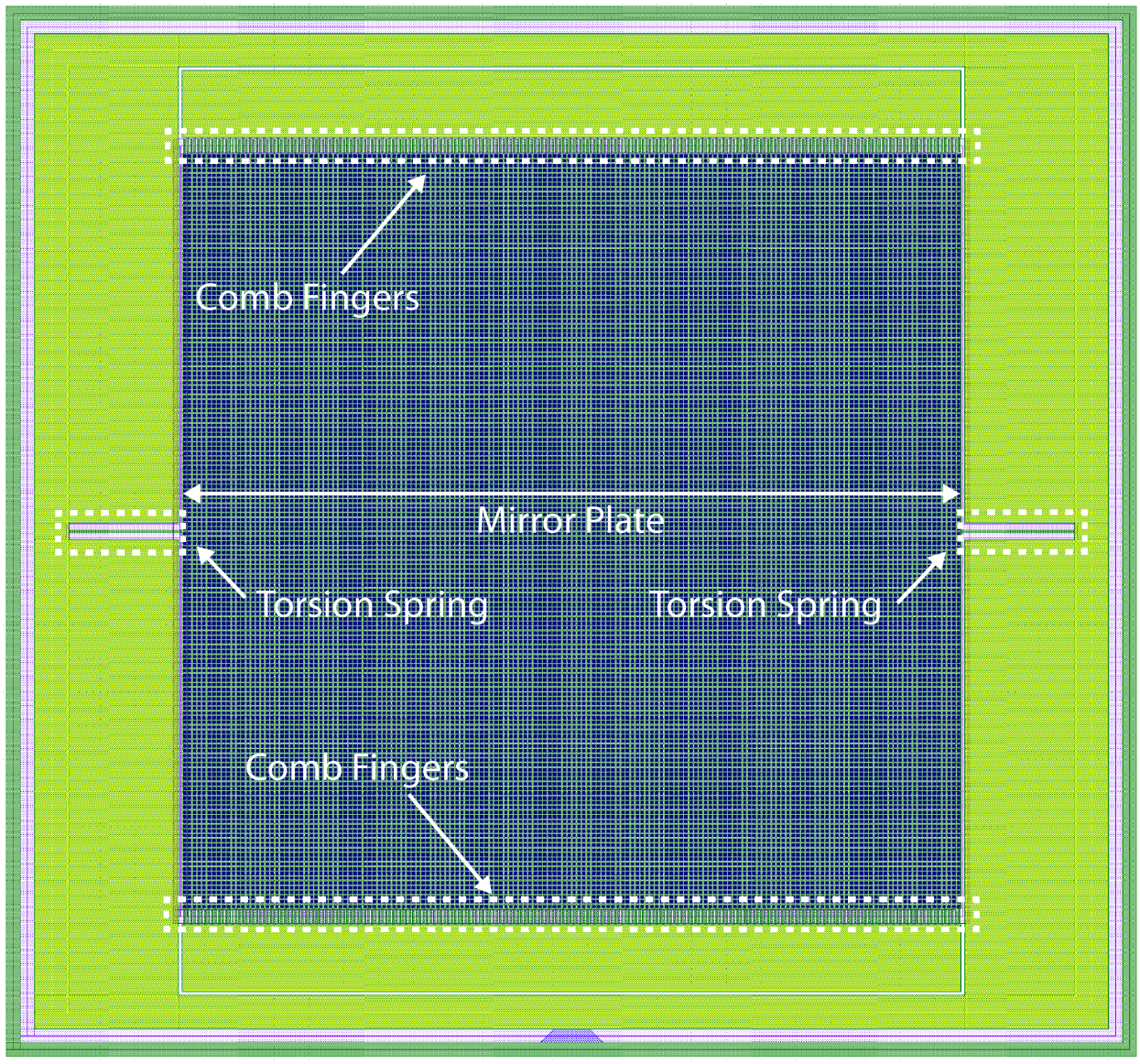

(b) MEMS mirror with SOI Holes

Figure 4.8: This is an example of the type of layouts generated by the layout script. The green areas are the device layer. The dark blue sections are the regions that will be etched. The comb fingers are located at the top and bottom. The torsion springs are located on the left and right. Ideally, the trench layout design would remove the substrate under the mirror with HF without affecting the optical properties of the RMM. The SOI hole layout was fabricated as a backup.

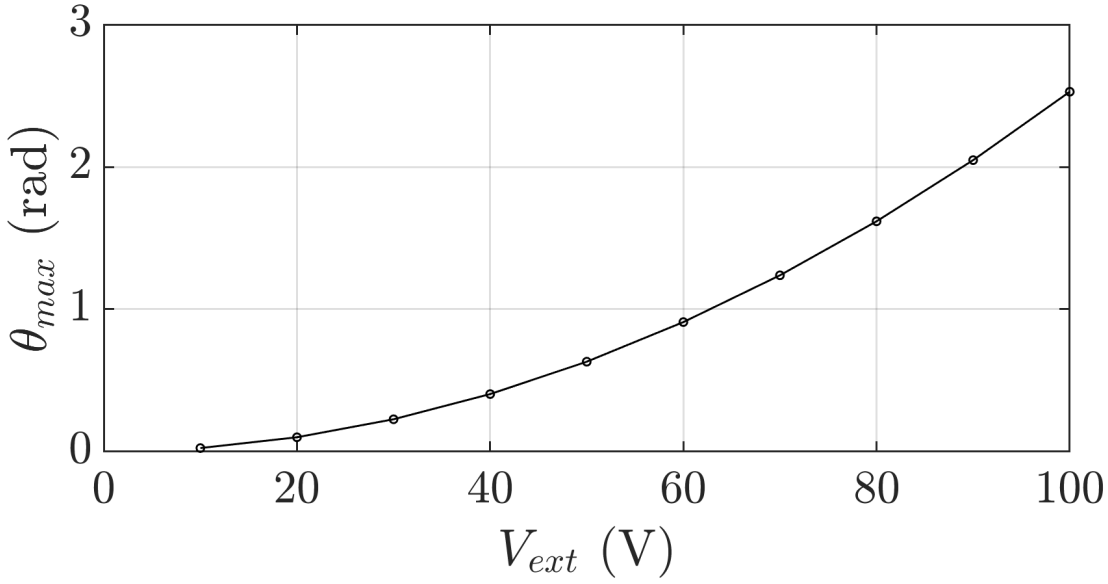

Figure 4.9: θ_{max} vs V_{ext} for the 50V design

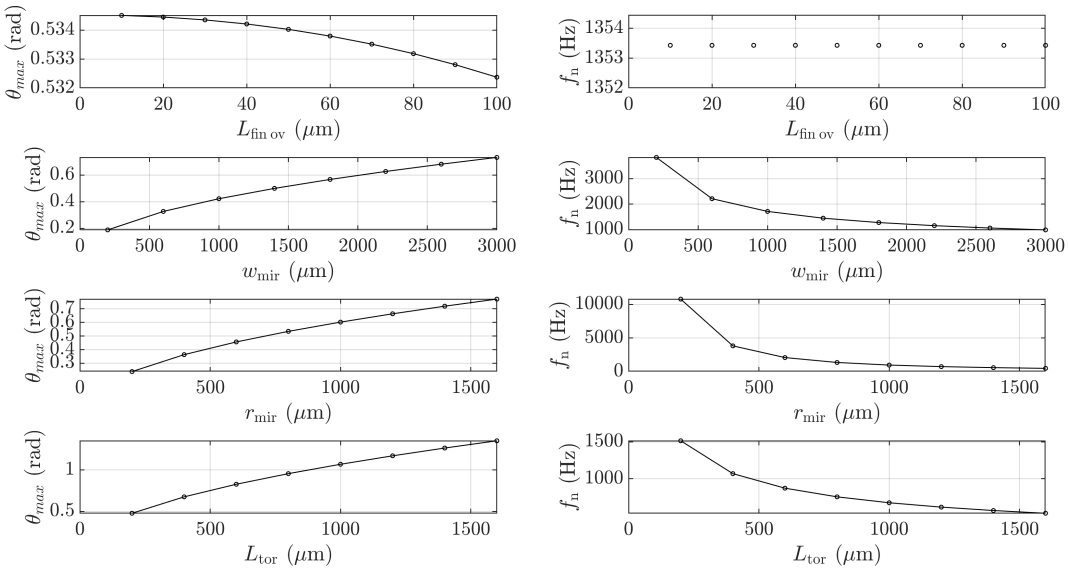

Figure 4.10: Demonstrates how $\theta_{\max}$ and f_{n} vary as L_{tor}, w_{mir}, r_{mir}, and $L_{\text{fin ov}}$ are swept

Parameter	**Units**	**Spec 1**	**Spec 2**	**Spec 3**
Voltage	V	20	50	100
w_{fin}	µm	2	2	2
g_{fin}	µm	4	4	4
$L_{\text{fin ov}}$	µm	20	30	100
L_{fin}	µm	24	34	104
N_{g}	unitless	633	266	74
L_{tor}	µm	500	250	250
w_{tor}	µm	2	2	2
r_{mir}	µm	1900	800	275
w_{mir}	µm	3800	1600	550
f_{n}	Hz	169	1353	11427
FOV	deg	67	122	124
Power	µW	3	79.4	1998
Area	μm^2	5000× 4276	2300× 2096	1250 × 1186
s_{res}	mm	1	1	1
f_{sample}	kHz	315	4544	39145
i_{pulse}	µA	0.6	6.4	24
t_{pulse}	µsec	66	10	3.6
f_{CK1}	kHz	15	92	273
$\bar{i_{\text{n}}}$	pA	0.1	0.4	1.48

Table 4.3: Design comparison for 20 V, 50 V and 100 V RMM design. The top section of the table are for the input parameters. The bottom section is for the derived parameters.

able to achieve the s_{res} = 1mm because their fastest clock is only 20 MHz.

The 50 V design is best candidate because it meets all of the target specs and can be driven by Zappy2 and SCµM. Fig. 4.6 demonstrates the simulated startup of the 50 V RMM design using Matlab's ordinary differential equation solver, ODE 45, with the initial conditions $\theta(0) = \bar{\theta}_{\text{n}}$ and $\dot{\theta}(0) = \bar{\theta}_{\text{n}}\omega_{\text{n}}$. The RMM resonates at roughly the expected f_{n} = 1353Hz and converges to an amplitude of θ_{max} = ~0.53 in Fig. 4.6. f_{n} = 1353Hz was also confirmed by the FFT of $\theta(t)$ shown in Fig. 4.7. A sample layout for RMM can be seen in Fig. 4.8. Since $\theta_{\text{max}} \propto V_{\text{ext}}^2$, θ_{max} is expected to significantly increase as V_{ext} increases. Fig. 4.9 demonstrates θ_{max} vs V_{ext} for the 50V design.

In order to compare theory with experimental results for the RMM L_{tor}, w_{mir}, r_{mir}, and $L_{\text{fin ov}}$ were swept before it was manufactured. Fig. 4.10, demonstrates how θ_{max} and f_{n} depend on the parameters that will be swept. θ_{max} has the biggest dependence on L_{tor} while $L_{\text{fin ov}}$ has a minimal one. f_{n} has as strong dependence on r_{mir}.

4.5 Conclusions

A 50V mirror design was demonstrated to meet all of the desired specs: power = 79.4µW, FOV = 122°, f_n = 1353Hz, etc. The mirror is 1600 x 1600 µm^2 with two 2 x 250 µm^2 torsion springs and 266 comb finger pairs with an overlapping area of 2 x 30 µm^2. This mirror is a viable replacement for a HTC Vive Lightouse Beacon with low power consumption and a millimeter scale footprint which would allow for the 3D localization of swarms of microrobots.

Chapter 5

Conclusions and Future Work: The Next Generation of Crystal-Free Radios

5.1 OsciBear 28 nm IoT SoC

Similar to SCµM, OsciBear(Open-source **S**o**C** for **I**oT with **BL**E, **A**ES and **R**adio) is meant for low-power wireless BLE applications. OsciBear integrates power, clocking, a 2.4 GHz BLE transceiver, digital baseband, RISC-V CPU, and an Advanced Encryption Standard (AES) accelerator. The following external references are provided VREF = 0.9 V, IREF = 10 µA, CPU Clock ref of 20 MHz, and a phased-locked loop (PLL) reference of 2 MHz.

As shown in Fig. 5.1, OsciBear is a $1\times1\text{mm}^2$ IoT SoC chip designed in TSMC 28 nm high-performance computing (technology) through the Berkeley Wireless Research Center (BWRC). This was part of the 2021 tapeout class [90] with roots dating back to 2017 [9]. The main idea is to take students with minimal tapeout experience and have them design a chip in 14 weeks. This chip leverages research infrastructure such as ChipYard [2] for generating Rocket cores and Berkeley Analog Generator (BAG) [24, 12] to generate amplifiers, Low-Drop Out regulators [65] and an analog-to-digital converter (ADC) [49].

Fig. 5.3 is a system diagram of the RF frontend. The RX has a low-IF architecture. The TX uses direct modulation and a 4.8 GHz voltage controlled oscillator (VCO) that is divided by 2 and a PA driver. A phased locked loop (PLL) was designed to tune the VCO into the frequency channel. The modulation scheme, gaussian frequency-shift keying (GFSK), was implemented through a 4-bit modulation capacitor digital-to-analog converter (DAC).

The total area used for the VCO was $0.0415\,\text{mm}^2$ with 76% of the area taken by the $170\times186\mu\text{m}^2$ inductor. As shown in Fig. 5.4, a class-B topology was used for the VCO to reduce power consumption. As discussed in [51], this topology saves power because the LC tank sees at least one $-g_\text{m}$ from the NMOS and PMOS at all points during steady state oscillation. A 4-bit coarse DAC was placed in parallel to the LC tank along with a

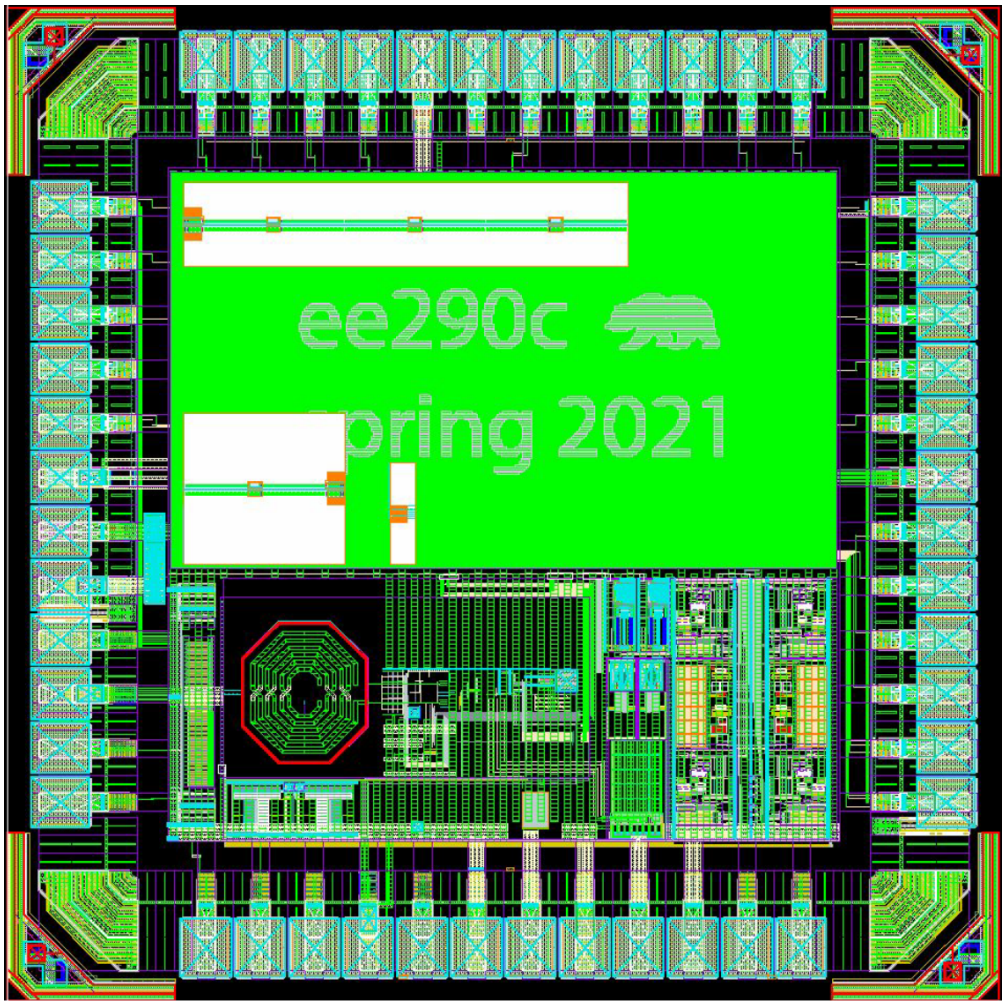

Figure 5.1: OsciBear's $1\times1\mu m^2$ Layout

varactor. The modulation requirements for BLE are $\pm250\,\text{kHz}$ with a max frequency drift of $50\,\text{kHz}$ thus fine resolution steps are needed for the 4-bit modulation DAC. To achieve this fine resolution with an inductance of $2.66\,\text{nH}$ and a desired change in frequency of $f_{\text{RF}}-\Delta f_{\text{RF}} = 2\times2.483\text{GHz}-2\times50\text{kHz}$ a $\Delta C = \sim15.5\text{aF}$ capacitor would be needed as shown in Eq. 5.1 and Eq. 5.2.

$$C = \frac{1}{L(2\pi f_{\text{RF}})^2} = \frac{1}{2.66\text{nH}(2\pi(2\times2.483))^2} \tag{5.1}$$

$$\Delta C = \frac{1}{L(2\pi(f_{\text{RF}}+\Delta f_{\text{RF}})^2} - C \approx 15.5\text{aF} \tag{5.2}$$

Minimum sized caps are limited to 1-2 fF therefore other methods are required to create a $\Delta C = 15.5\text{aF}$. Series capacitance and source degeneration are two approaches for making

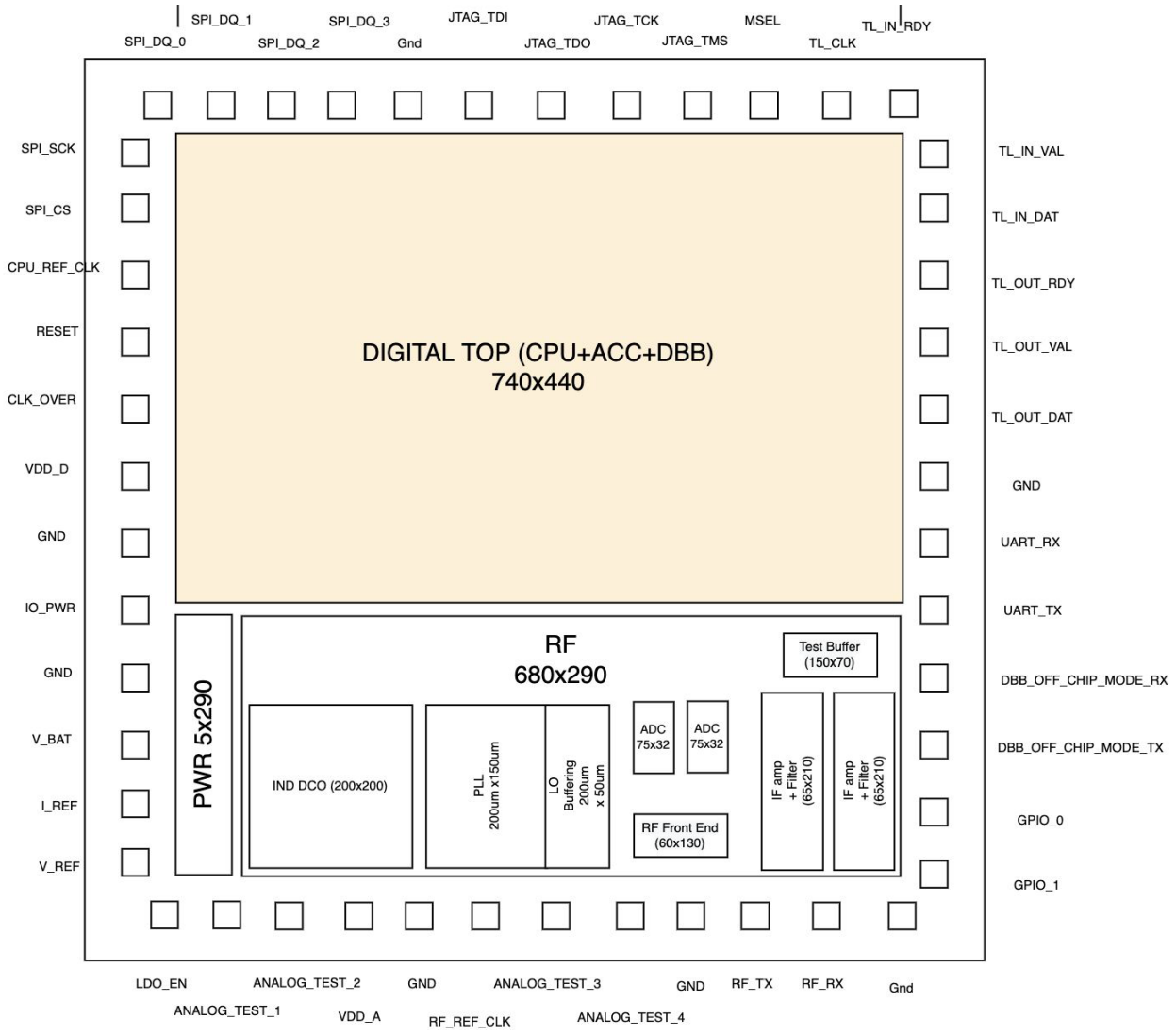

Figure 5.2: OsciBear's Block Diagram

small capacitors while maintaining digital control. Series capacitance can be used to make fine resolution steps but it would require big enough capacitor to reduce the min sized capacitor of 2 fF by a factor of 100. Source degeneration is advantageous because the 100x reduction comes from the NMOS cross-coupled pair when placing the 4-bit modulation cap dac at the source as shown in Fig. 5.4. In other words, source degeneration reduces capacitance while maintaining a small area. With the 4-bit modulation cap DAC at the source, the LC tank sees a $C_{\mathrm{eq\,mod}} \propto g_{\mathrm{m}}^2 * C_{\mathrm{mod}}$ similar to SCµM [52, 51, 28]. See Table 5.1 for the targeted specs for the VCO.

While the desired frequency bandwidth was 600 MHz, when tested the bandwidth was 474 MHz with 15 MHz coarse steps as seen in Fig. 5.6. The Bluetooth Low Energy spectrum

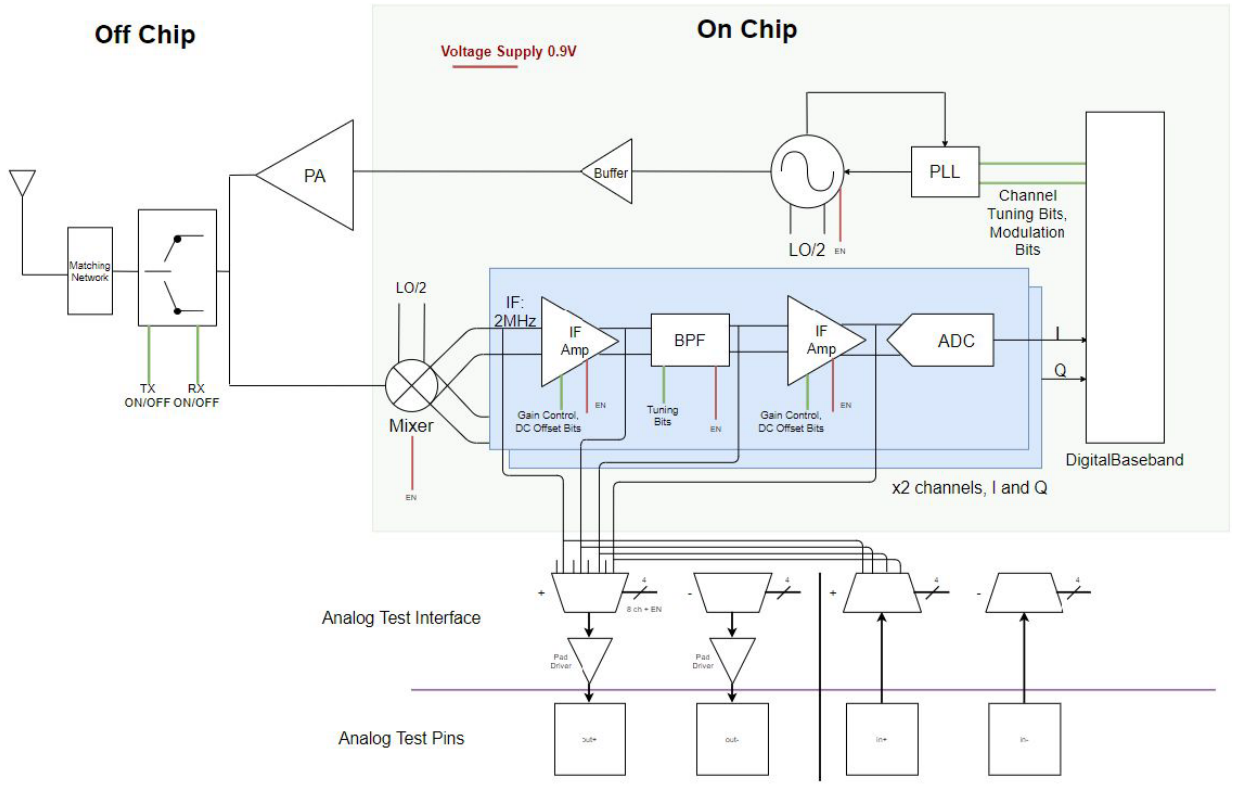

Figure 5.3: OsciBear's RF Frontend Schematic

Table 5.1: Specs for OsciBear VCO

Spec	Value
f_{LO}	4.8 GHz
VDD	0.9 V
Power	0.99 mW
Q	10.5
Inductance	2.66 nH
Bandwidth	1.2 GHz
Varactor Tuning	79 MHz

is 2.4-2.483 GHz thus the VCO covers 70% of the spectrum that is desired. However, it might be possible to extend that with varactor tuning since it has a simulated tuning range of 71 MHz as shown in Fig. 5.5.

It was questionable if Bluetooth devices pick up OsciBear's TX packets since the modulation was only able to achieve ±250 kHz. However, Daniel Lovell was able to figure out how to transmit a packet from OsciBear to an nRF52840 DK. While OsciBear tuned to BLE's advertising channel, 38, the nRF Bluetooth packet sniffer was able to demodulate the

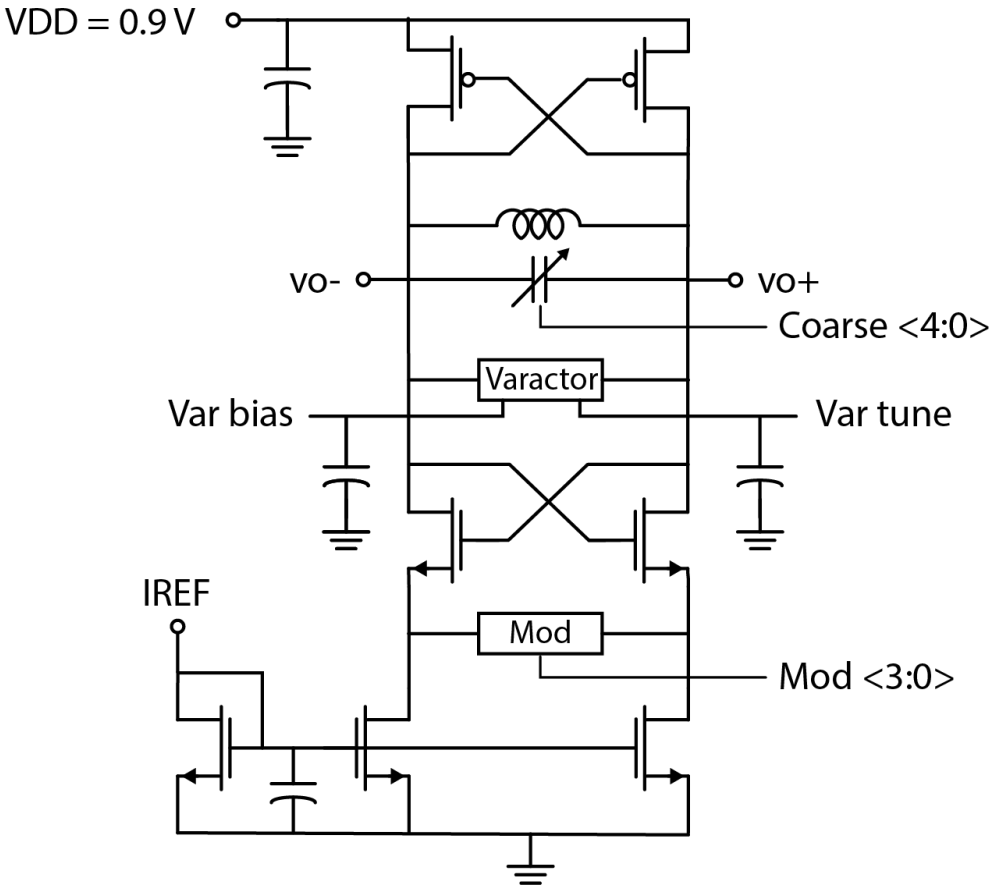

Figure 5.4: OsciBear VCO Schematic

"OSCIBEAR SAYS HELLO" packet as demonstrated in Fig. 5.7. Code can be found here: `https://github.com/ucb-ee290c/OsciBear-Bringup/tree/rf-testing-firmware`

One last thing that was worth checking is if the RF frequency shifts with respect with VBAT like it did with SCµM. Fig. 5.8a demonstrates OsciBear's setup to measure f_{RF} vs VBAT. Fig. 5.8b is meant to mimic SCµM's varying bandgap VREF. VREF was swept in increments of 8 mV from 900 $\rightarrow$ 820 mV while VBAT was swept from 1.8 $\rightarrow$ 1.5 V in increments of 50 mV. The resulting $\Delta f_{\mathrm{RF}} \approx 4.1$ MHz which is similar to SCµM in Fig. 5.9 with a $\Delta f_{\mathrm{RF}} \approx 11.1$ MHz. Fig. 5.8c measured f_{RF} vs VBAT but with an external VREF = 0.9 V. This resulted in a $\Delta f_{\mathrm{RF}} \approx 432$ kHz. This means that with a stable voltage reference the oscillator could tolerate a ΔVBAT = 200 mV without moving out of the 40 ppm requirement. Section 5.2 will discuss methods beyond those described in Section 2.3 to address frequency shift in hardware.

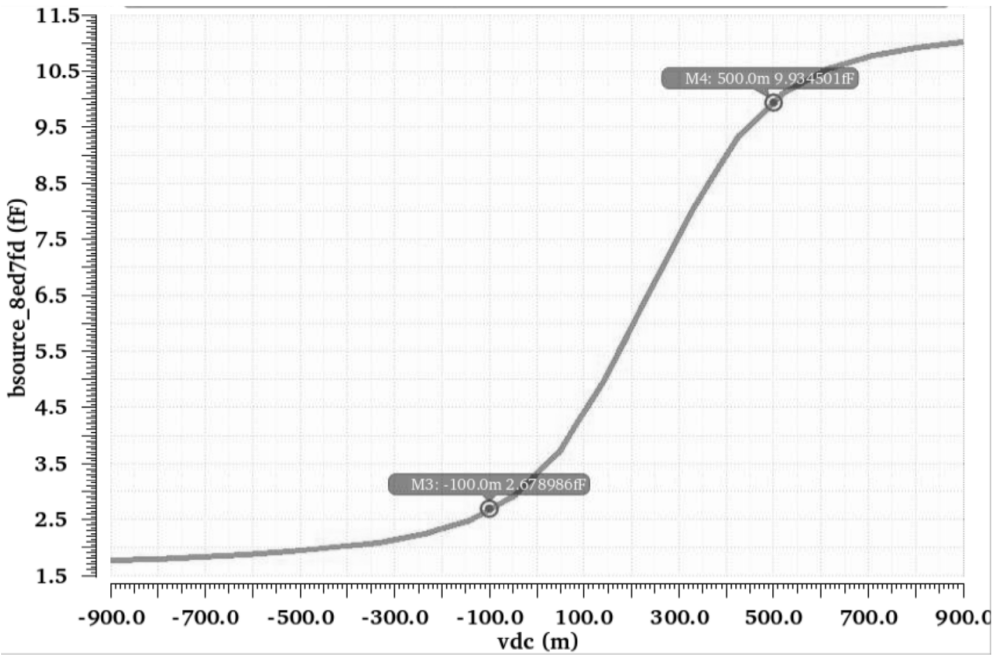

Figure 5.5: Varactor's capacitance vs Var tune. With a KVCO = 143 MHz V^{-1}, Var bias = 300 mV, and Var tune = 200-700 mV the varactor has a frequency tuning range of ~71 MHz

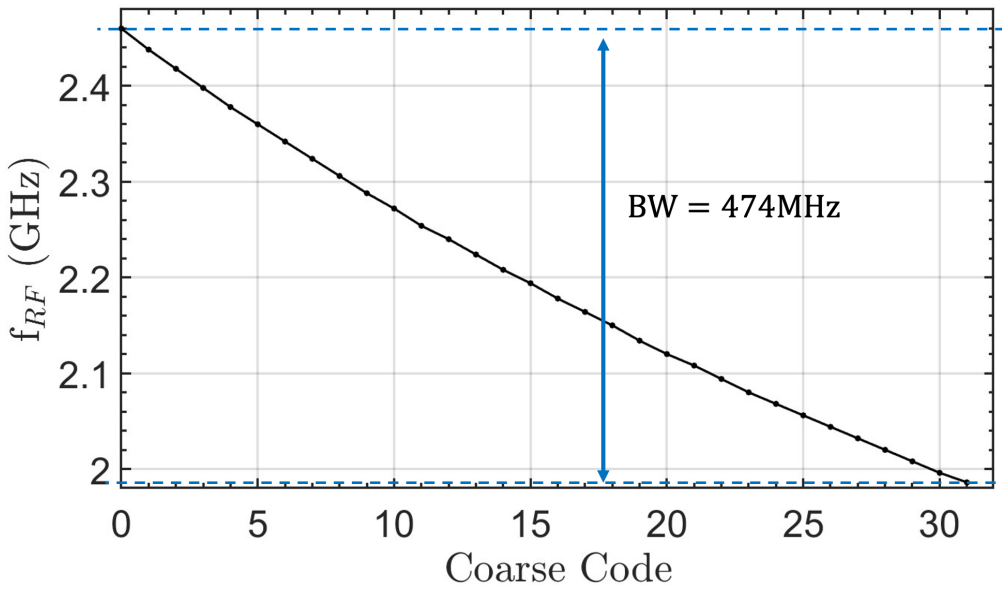

Figure 5.6: OsciBear's coarse tuning range of 474 MHz with steps ~15 MHz

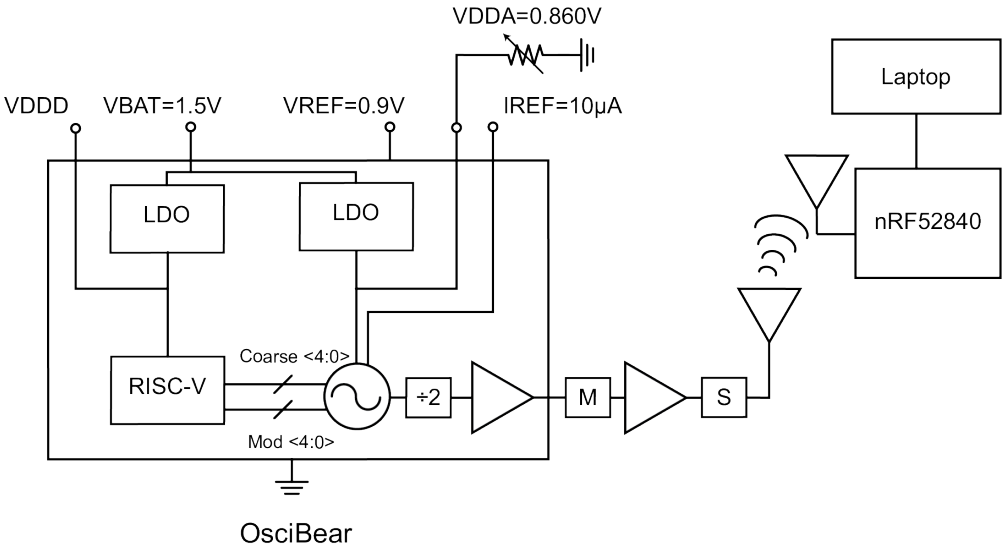

(a) OsciBear's setup for transmitting BLE packets. The following external supplies were provided: VBAT=1.5 V, VREF=0.9 V, and IREF=10 µA. VREF connects to both LDOs. At the output of OsciBear there is matching network ("M"), a 20 dB power amplifier (PA), and an RF switch ("S"). To tune the VCO to channel 38, 2.426 GHz, the closest coarse setting to channel 38 was used then a potentiometer was attached to VDDA and tuned until the correct frequency was reached (VDDA=0.860 V).

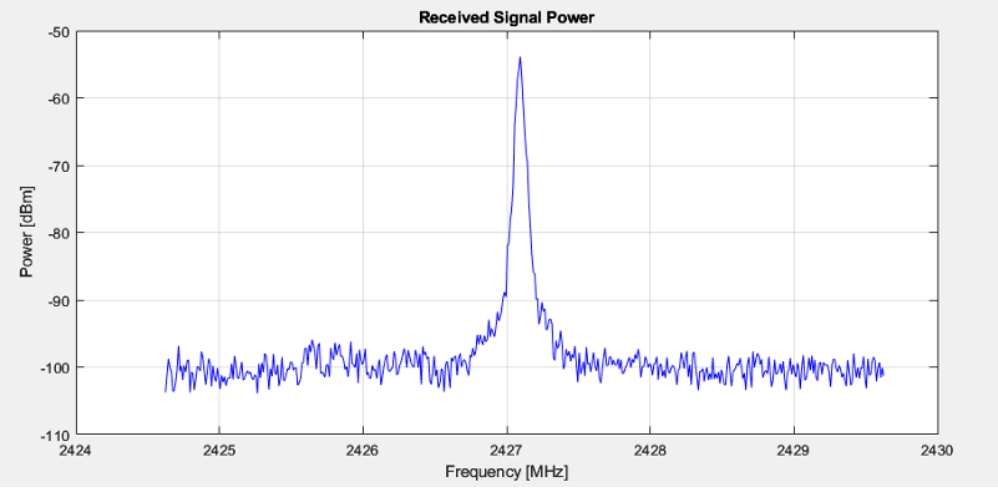

(b) OsciBear's transmit power measured over-the-air with a spectrum analyzer at a 1 m distance

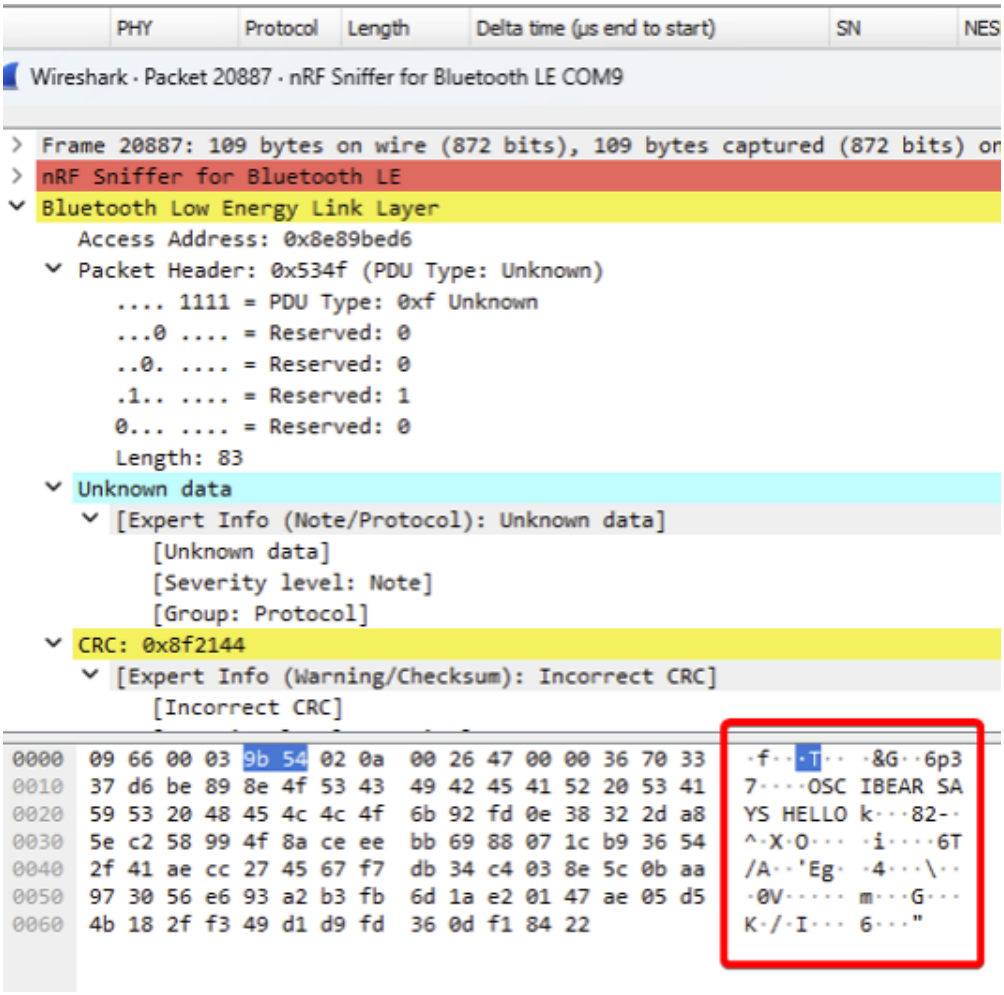

(c) nRF52840 DK receiving a packet from OsciBear containing "OSCIBEAR SAYS HELLO" on BLE's advertising channel 38. Credit goes to Daniel Lovell for implementing this.

Figure 5.7: OsciBear sending packets to nRF52840.

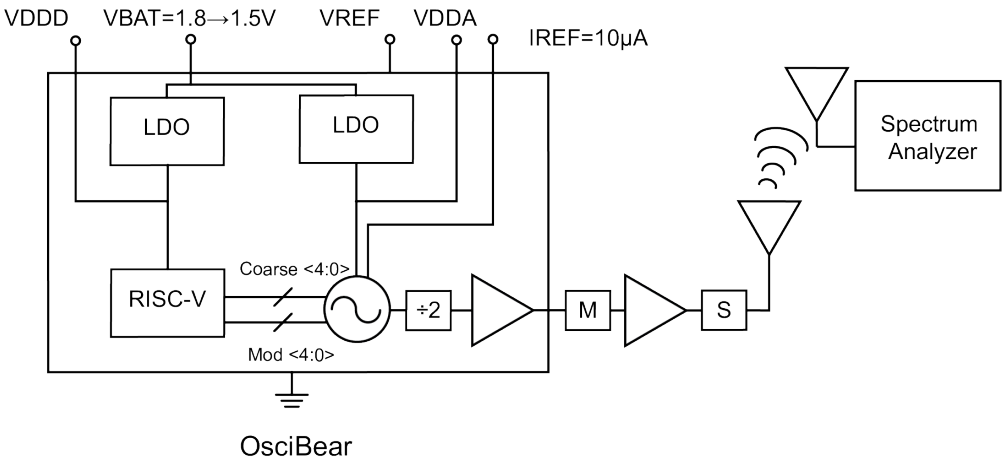

(a) OsciBear's setup for f_{RF} vs VBAT. The following external supplies were provided: VBAT = 1.8→1.5 V, VREF = 0.9 V, and IREF = 10 µA. Coarse setting was set to 0 to output the max frequency.

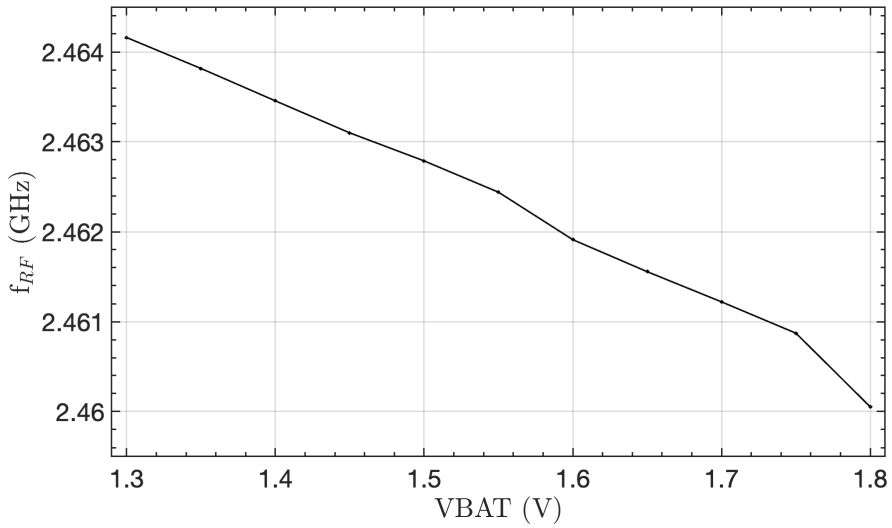

(b) OsciBear's f_{RF} vs VBAT with a varying VREF. To mimic SCµM's bandgap voltage vs VBAT (Fig. 5.12a), VREF was swept in increments of 8 mV from 900 → 820 mV in unison VBAT was swept from 1.8 → 1.3 V in increments of 50 mV. $\Delta f_{\mathrm{RF}} \approx 4.1$ MHz

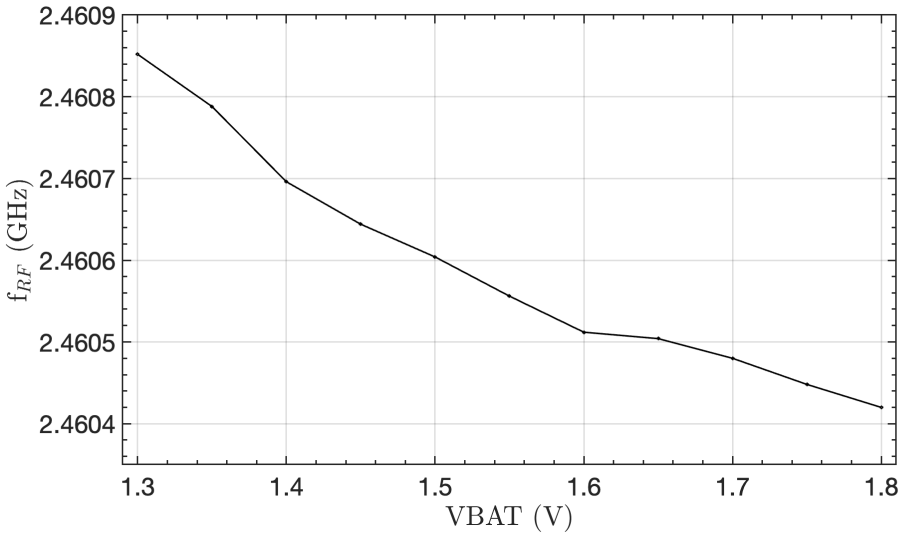

(c) OsciBear's f_{RF} vs VBAT with VREF $= 0.9\,\mathrm{V}$. VBAT was swept from $1.8 \rightarrow 1.3\,\mathrm{V}$ in increments of $50\,\mathrm{mV}$. $\Delta f_{\mathrm{RF}} \approx 432\,\mathrm{kHz}$

Figure 5.8: Frequencies vs VBAT and varying VREF conditions

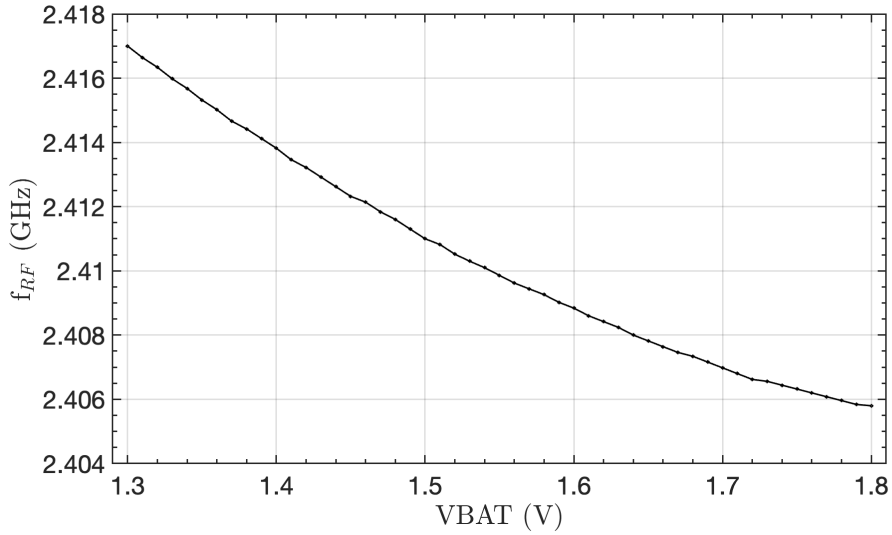

Figure 5.9: SCμM's f_{RF} vs VBAT. VREF is generated by an on-chip bandgap thus was not swept. VBAT was swept from $1.8 \rightarrow 1.3\,\mathrm{V}$ in increments of $50\,\mathrm{mV}$. $\Delta f_{\mathrm{RF}} \approx 11.2\,\mathrm{MHz}$

5.2 Towards Robust Crystal-Free Radios

This paper [87] discusses what can cause oscillators to shift with respect to voltage. As VDD changes then Ibias and Vamp changes. This ultimately affects how much time the transistors spend in each region of operation off, saturation and triode. Overall, this affects the equivalent parasitic capacitance CMOS diff seen by the LC tank inside the VCO.

[16] described two techniques to address this. Amplitude tracking provides optimal biasing point, can track across process, voltage and temperature. However, it consumes a lot of power, the tracking loop bandwidth is limited to $\frac{\omega_{\text{osc}}}{2Q}$. It also is limited by a stable VREF. The feedfoward supply ripple replica and cancellation method consumes less power, has a higher bandwidth, 10x improvement in supply pushing reduction. The drawback is that you need calibration for process, voltage and temperature. While these methods are attractive options, it was beneficial that hardware and software tests could be done on SCµM to better understand f_{RF} vs VBAT. The first step was to replicate the same tests seen on the bench top in simulation as highlighted in Fig. 5.10 VBAT was swept and and the bandgap reference was kept ideal. The results are shown in Fig. 5.11 which lets us know that if the bandgap were ideal a ΔVBAT=150 mV and ΔVBAT=350 mV would be tolerable while still staying withing the 40 ppm and 150 ppm requirement. As discussed in Section 2.3, the voltage drops of ΔVBAT=165 mV would cause f_{LO} to shift by 2.7 MHz. With a better bandgap the calibration procedure could be removed or even better smaller capacitors could be used with the new hardware combined with the compensation technique.

As seen in Fig. 5.12, with a shift of 500 mV in VBAT there is a 75 mV for VBG and 80 mV for VDD_{LO}. This translates to a power supply rejection ratio (PSRR) of ~16 dB for both. In contrast if an ideal bandgap were used the LDO PSRR would shoot up to 34 dB. Since the PSRR of the LDO and bandgap are tied together a better bandgap is desired. As shown if Fig. 5.13, the sub-1 V bandgap was used for SCµM [3]. For PSRR vs the ideal amplifier gain in Fig. 5.15 we notice that the PSRR goes up with the gain. To reach a PSRR = 34 dB a gain of ~240 would be needed. However, a higher PSRR could be achieved if a cascode were to be added. Comparing Eq. 5.6 vs 5.7, there is an additional factor of g_{m} with the addition of a single transistor increasing the PSRR for the cascode. In Fig. 5.15b, the bandgap with a cascode reaches a PSRR = 68 dB with an amplifier gain of 50.

$$Z_1 = R_1 \parallel r_{\text{d}} \tag{5.3}$$

$$Z_2 = R_2 \parallel (R_3{+}r_{\text{d}}) \tag{5.4}$$

$$\frac{V_{\text{g}}}{V_{\text{in}}} = \frac{A_{\text{o}}(1{+}g_{\text{m}}r_{\text{o}})\left(\frac{Z_2}{Z_2{+}r_{\text{o}}}{-}\frac{Z_1}{Z_1{+}r_{\text{o}}}\right)}{\left(1{+}A_{\text{o}}g_{\text{m}}r_{\text{o}}\frac{Z_2}{Z_2{+}r_{\text{o}}}{-}\frac{Z_1}{Z_1{+}r_{\text{o}}}\right)} \tag{5.5}$$

$$\text{PSSR} = \frac{V_{\text{in}}}{V_{\text{ref}}} \tag{5.6a}$$

$$= \frac{1+\frac{r_{\text{o}}}{R_4}}{1-g_{\text{m}}r_{\text{o}}\left(\frac{V_{\text{g}}}{V_{\text{in}}}-1\right)} \tag{5.6b}$$

$$\approx \frac{r_{\text{o}}+R_4}{R_4} \qquad \text{Assuming } A_{\text{o}} \text{ and } g_{\text{m}}r_{\text{o}} \gg 1 \tag{5.6c}$$

$$\text{PSSR}_{\text{cascode}} = \frac{V_{\text{in}}}{V_{\text{ref}}} \tag{5.7a}$$

$$= \frac{R_4+g_{\text{m}}r_{\text{o}}^2+2r_{\text{o}}}{(R_4+g_{\text{m}}r_{\text{o}}R_4)\left(1-g_{\text{m}}r_{\text{o}}\left(\frac{V_{\text{g}}}{V_{\text{in}}}-1\right)\right)} \tag{5.7b}$$

$$\approx \frac{R_4+g_{\text{m}}r_{\text{o}}^2+2r_{\text{o}}}{R_4+g_{\text{m}}r_{\text{o}}R_4} \qquad \text{Assuming } A_{\text{o}} \text{ and } g_{\text{m}}r_{\text{o}} \gg 1 \tag{5.7c}$$

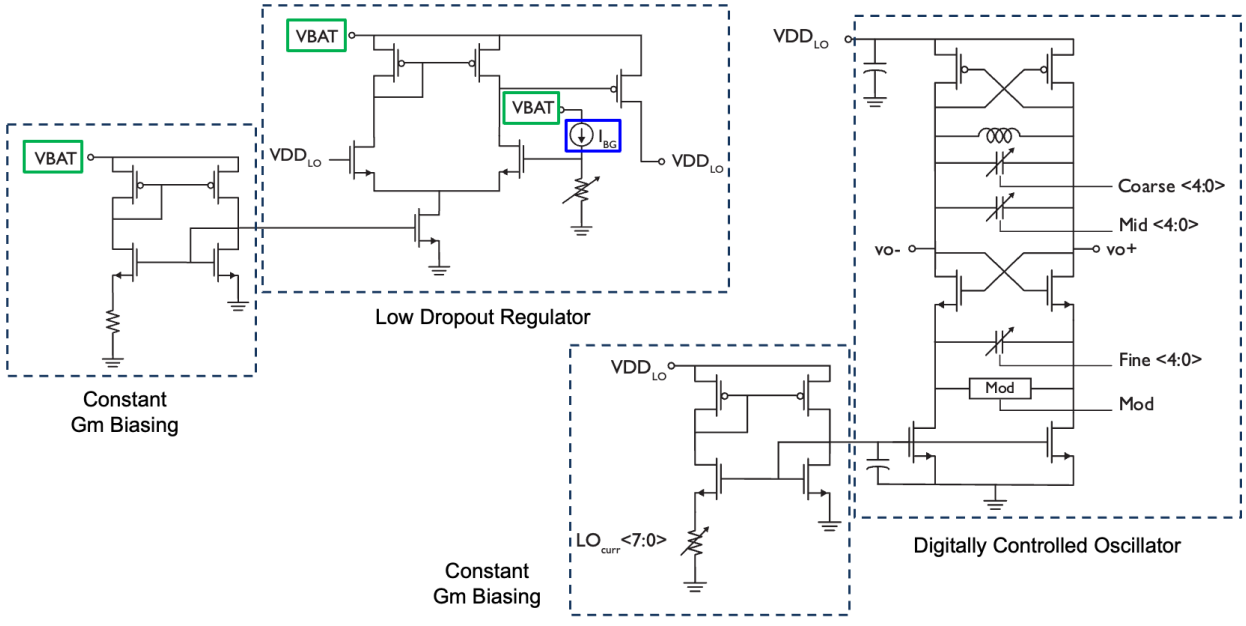

Figure 5.10: Schematic of SCµM's LDO, bandgap and VCO

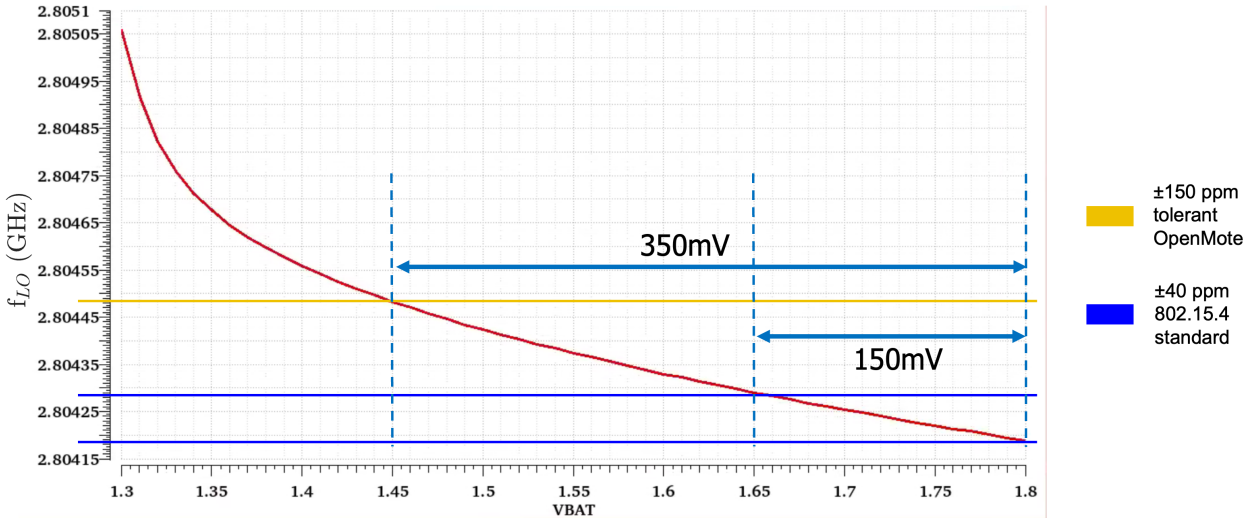

Figure 5.11: Simulation of f_{LO} vs VBAT on SCµM's DCO with an ideal bandgap reference

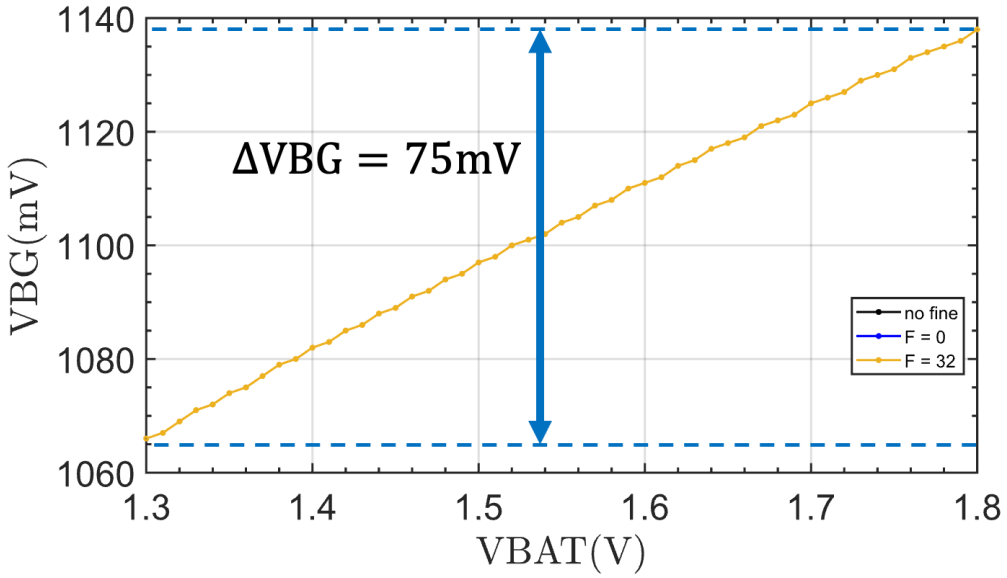

(a) VBG vs VBAT using SCµM's bandgap. The PSRR=~16.4 dB

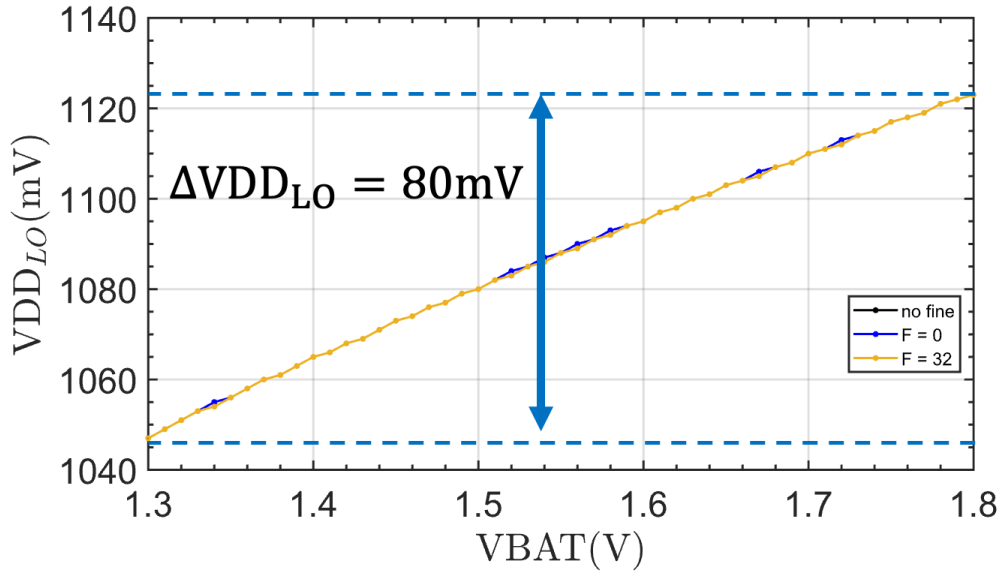

(b) VDD_{LO} vs VBAT using SCµM's bandgap. The PSRR=~15.9 dB

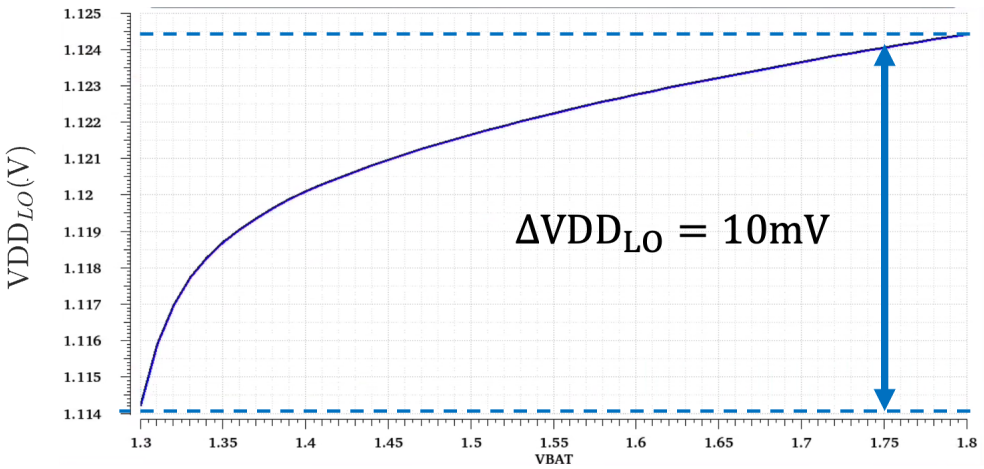

(c) VDD_{LO} vs VBAT using an ideal bandgap. The PSRR=~33.9 dB

Figure 5.12: Comparing how VDD_{LO} and VBG vary with respect to VBAT

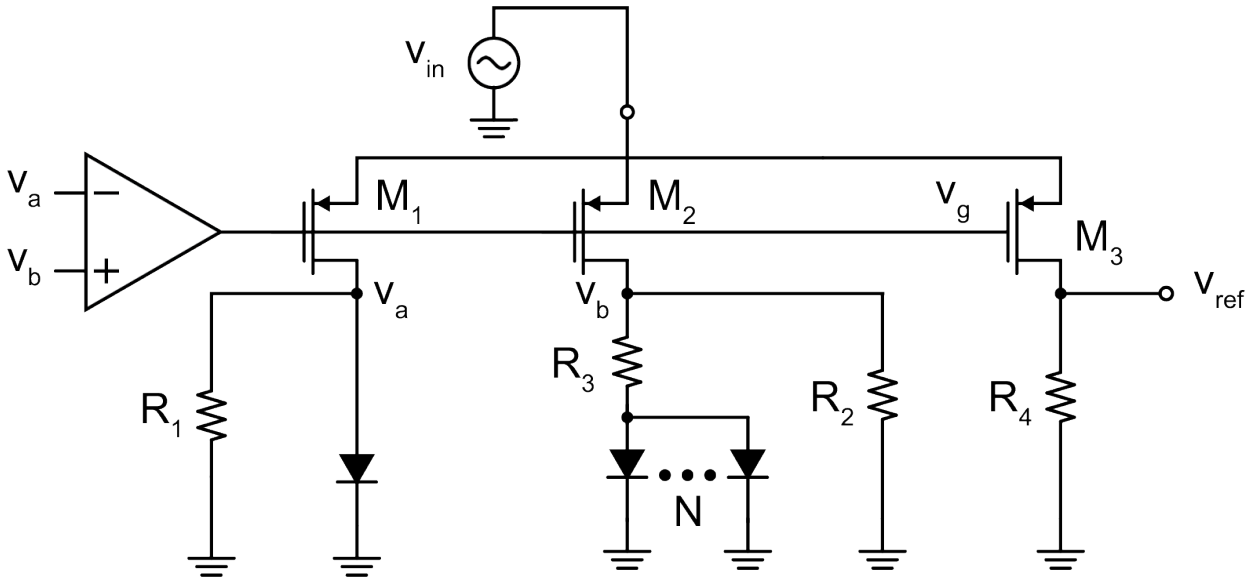

Figure 5.13: Bandgap Schematic

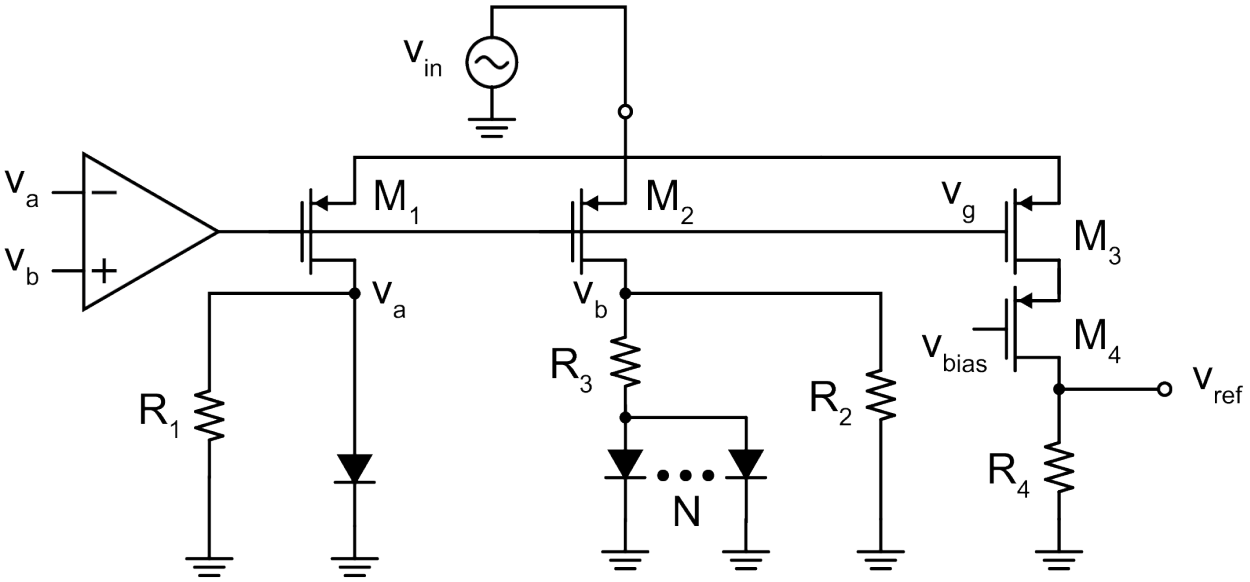

Figure 5.14: Bandgap Cascode Schematic

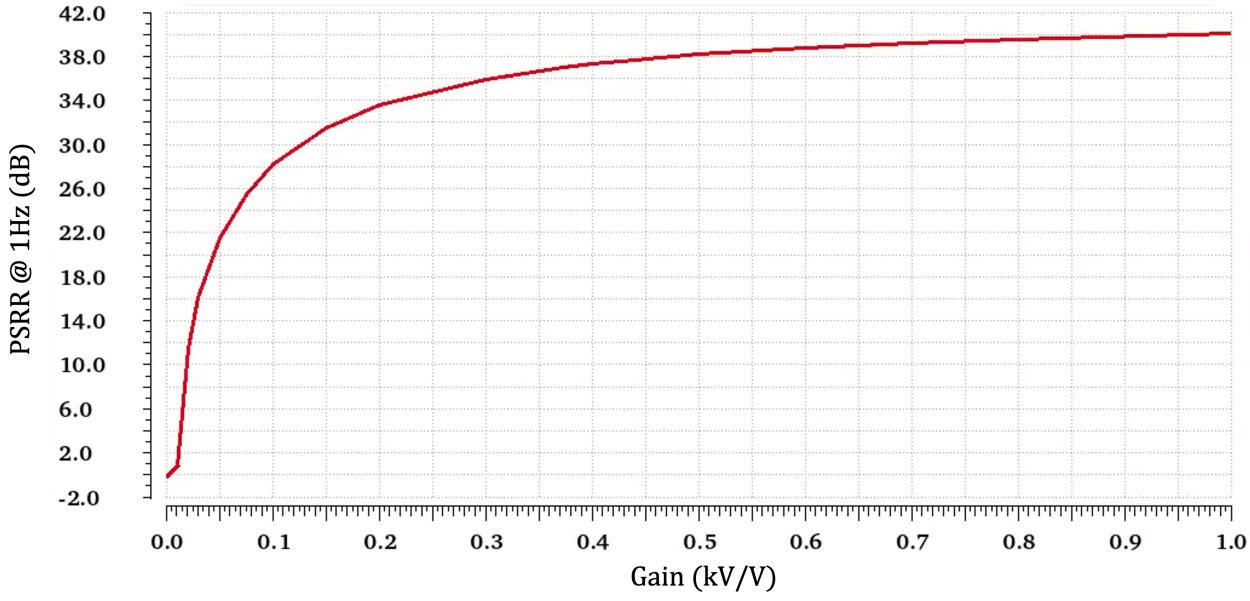

(a) PSRR vs ideal amplifier gain for bandgap. To reach a PSRR = 34 dB a gain of ~240 would be needed

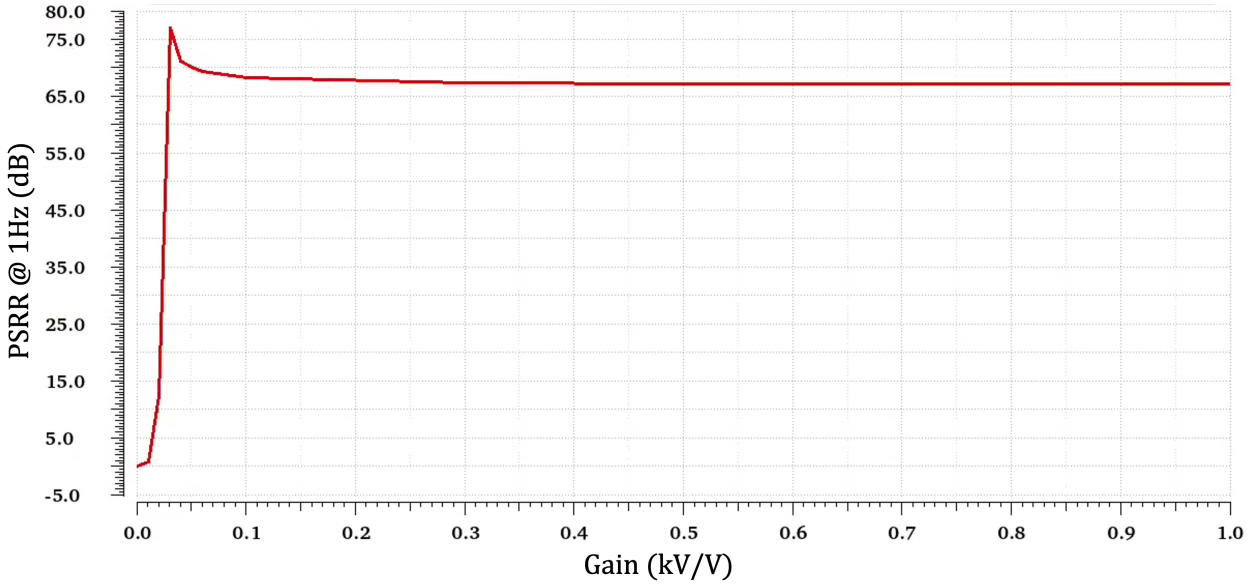

(b) PSRR vs ideal amplifier gain for bandgap with cascode. To reach a PSRR = 34 dB a gain of 50 would suffice

Figure 5.15: PSRR vs amplifier gain

5.3 The Future

Battery Scaling

Batteries can become smaller by using thicker electrodes [91], cell stacking [55] or reducing the capacity. The printed microbatteries Anju Toor [91] made have a series resistance as high as 100 Ω. If we want to reduce the electrode area, cell stacking can be used while keeping the series resistance the same. If we want to reduce volume as well then thicker electrodes and chemistry optimization/manufacturing seem like the right direction. Assuming there is a linear relationship between electrode area and volume with resistance. If you make the electrode's area 2x smaller you would have to increase the thickness 2x to have the same capacity resulting in a resistance 4x higher.

Using a theoretical example: for a battery resistance of 400 Ω where 15 mV corresponds to 40ppm, the maximum current would be limited to 37.5 µA. Otherwise, f_{LO} would get kicked out of the 802.15.4 channel. With a capacitor we are able to bypass our dependence on the battery for short bursts of high current draw.

Assuming the same conditions from above with a TX current equal to 1 mA and an 0402 effective $C_{\mathrm{decap}} = 8\,\mu\mathrm{F}$ (rated for 22 µF). We could transmit for 120 µs or 3B before being pushed out of the 802.15.4 channel.

The two examples above highlight that smaller batteries with higher resistance won't be able to provide the high current loads necessary for low-power radios like SCµM to transmit 133B 802.15.4. However, for future low-power radios a combination of software compensation (Sec. 2.3), high PSRR LDOs (Sec. 5.2) and high PSRR DC-to-DC converter could let the battery voltage fall from 4.2 V to 0 V for short µs bursts of current draw and maintain f_{LO} within ±40 ppm.

Miniaturizing the Radio SoC

Assuming the digital circuits of the SoC follows Moore's law, the number of transistors doubling every 2 year, the size would be cut by half every two years. For example, SCµM's 2017 ARM Cortex M0 is $0.9\times1.5\mathrm{mm}^2$. In contrast, OsciBear's 2021 RISC-V processor measured $0.740\times0.440\mathrm{mm}^2$ roughly 4x smaller. Assuming this trend continues it would take about 8 years for the digital portion to reach $0.200\times0.200\mathrm{mm}^2$. At this point the size limitations would be dominated by the analog components if a 4.8 GHz oscillator like the one on OsciBear is used.

Inductors remain largely unchanged between technology since on-chip inductors depend mostly on the geometry. There is some work [42] that uses intercalated graphene, which has a large kinetic inductance and high conductivity, to make inductors with a Q=12 and a 1.5x higher inductance density. However, reaping these benefits depend on process manufacturers adopting this.

In contrast, the area capacitors take up is substantially smaller thus not a big consideration for scaling. For instance in OsciBear, the coarse cap DAC is ~16x smaller than

the inductor. While we could make the inductor smaller and use dense capacitors, smaller inductors suffer from a lower Q which lowers phase noise, startup time, and increases power consumption.

In terms of LC tank sizes, a 4.8 GHz LC tank divided by two is smaller than a 2.4 GHz one due to the smaller inductor required. By comparison SCuM's entire TRX was $1\times0.980\text{mm}^2$ while OsciBear's entire die with digital and RF was $1\times1\text{mm}^2$. The RF alone was $0.680\times 0.290\text{mm}^2$. The designs do have distinctions: SCµM has a PA and a matching network while OsciBear has a PA driver and a big PLL ($0.0203\,\text{mm}^2$). While it seems attractive to increase the frequency of an LC tank and dividing it down it does not make sense unless we opt for higher power consumption in exchange for a smaller area.

It is generally understood operating at a higher frequency will consume more power because of switching losses, capacitive loading, conduction loading, etc. However, if you reduce the amount to time your radio is ON you could make the radio smaller and consume less power. 802.15.4 has a 250 kbps data rate and takes about 4.256 ms to transmit 133B. Assuming we were using this 24 GHz radio [31] with a 50 mbps data rate it would take 21.28 µs to transmit 133B.

With a VBAT = 1.5 V, ΔVBAT = 15 mV for 40ppm, effective $C_{\text{decap}} = 8\,\mu\text{F}$, and a t_{transmit} = 21.28 µs, this leads to a max current of 5.6 mA for a 24 GHz radio while staying within 40 ppm while transmitting. It might be a challenge to achieve such a current consumption since 24 GHz radios can consume ~30 mA [17] but [51] demonstrated 800 µW 24 GHz was feasible. Assuming 5.6 mA is feasible, the amount of charge consumed is 120 nC or 169 pJ/bit to transmit 133Bytes while for the 2.4 GHz radio it would take 4.256 µC or 6 nJ/bit. Based off the joule per bit and miniaturization, it makes sense to build a 24 GHz.

Making efficient antennas within a space considerably smaller than the wavelength is virtually unattainable. Therefore, when you design an extremely tiny mote and the antenna must fit inside it, you can actually conserve power by shifting to a higher frequency as discussed above. This is because, if not, the efficiency of the antenna decreases both the transmitted power and received power in proportion to the cube of $\left(\left(\frac{antenna_{\text{size}}}{\lambda}\right)^3\right)$. As a result, the overall effect is proportional to $\left(\left(\frac{size}{\lambda}\right)^6\right)$, as depicted in [51].

5.4 Final Remarks

Crystal-free radios provide a path towards making radios smaller. While they reduce size and power consumption, they suffer from a dependence on voltage and temperature. Software compensation techniques (Sec. 2.3) help overcome voltage droops during high transmission current increasing a 802.15.4 packet payload from 10B to 125B. High PSSR LDOs and bandgaps (Sec. 5.2) help reduce the effect VBAT has on f_{RF} as shown in Fig. 5.8c and 5.11. Leveraging these two methods enables the use of smaller microbatteries with high resistance. To push the envelope further to create even smaller IoT radios the next frontier is exploring higher frequencies like (24 GHz) for short µs bursts.

Bibliography

[1] Vive lighthouse base station, https://www.vive.com/us/accessory/base-station, retrieved 1/10/2020.

[2] Alon Amid et al. "Chipyard: Integrated Design, Simulation, and Implementation Framework for Custom SoCs". In: *IEEE Micro* 40.4 (July 2020). Conference Name: IEEE Micro, pp. 10–21. ISSN: 1937-4143. DOI: 10.1109/MM.2020.2996616.

[3] H. Banba et al. "A CMOS bandgap reference circuit with sub-1-V operation". In: *IEEE Journal of Solid-State Circuits* 34.5 (May 1999). Conference Name: IEEE Journal of Solid-State Circuits, pp. 670–674. ISSN: 1558-173X. DOI: 10.1109/4.760378.

[4] Colby L Bellew, Seth Hollar, and KSJ Pister. "An SOI process for fabrication of solar cells, transistors and electrostatic actuators". In: *TRANSDUCERS'03. 12th International Conference on Solid-State Sensors, Actuators and Microsystems. Digest of Technical Papers (Cat. No. 03TH8664)*. Vol. 2. IEEE. 2003, pp. 1075–1078.

[5] S. Boisseau et al. "Electrostatic Conversion for Vibration Energy Harvesting". en. In: *Small-Scale Energy Harvesting*. IntechOpen, Oct. 2012. ISBN: 978-953-51-0826-9. DOI: 10.5772/51360. URL: https://www.intechopen.com/chapters/40640 (visited on 08/07/2023).

[6] Miguel Borges et al. "HTC Vive: Analysis and Accuracy Improvement". In: *2018 IEEE/RSJ International Conference on Intelligent Robots and Systems (IROS)*. ISSN: 2153-0866. Oct. 2018, pp. 2610–2615. DOI: 10.1109/IROS.2018.8593707.

[7] D. C. Burnett et al. "Two-Chip Wireless H_2S Gas Sensor System Requiring Zero Additional Electronic Components". In: *Transducers 2019*. June 2019, pp. 1222–1225. DOI: 10.1109/TRANSDUCERS.2019.8808294.

[8] David C Burnett et al. "CMOS oscillators to satisfy 802.15.4 and Bluetooth LE PHY specifications without a crystal reference". In: *2019 IEEE 9th Annual Computing and Communication Workshop and Conference (CCWC)*. IEEE. 2019, pp. 0218–0223.

[9] David C Burnett et al. "Tapeout class: Taking students from schematic to silicon in one semester". In: *2018 IEEE International Symposium on Circuits and Systems (ISCAS)*. IEEE. 2018, pp. 1–5.

[10] Felipe M. R. Campos et al. "Lighthouse Localization of Wireless Sensor Networks for Latency-Bounded, High-Reliability Industrial Automation Tasks". In: *2020 16th IEEE International Conference on Factory Communication Systems (WFCS)*. Apr. 2020, pp. 1–8. DOI: 10.1109/WFCS47810.2020.9114443.

[11] Gilles Caprari and Roland Siegwart. "Mobile micro-robots ready to use: Alice". In: *2005 IEEE/RSJ international conference on intelligent robots and systems*. IEEE. 2005, pp. 3295–3300.

[12] Eric Chang et al. "BAG2: A process-portable framework for generator-based AMS circuit design". In: *2018 IEEE Custom Integrated Circuits Conference (CICC)*. ISSN: 2152-3630. Apr. 2018, pp. 1–8. DOI: 10.1109/CICC.2018.8357061.

[13] T. Chang et al. "QuickCal: Assisted Calibration for Crystal-Free Micromotes". In: *IEEE Internet of Things Journal* 8.3 (2021), pp. 1846–1858. DOI: 10.1109/JIOT.2020.3015725.

[14] Tengfei Chang et al. "6TiSCH on SCµM:Running a Synchronized Protocol Stack without Crystals". In: *ACMEmbedded Wireless Systems and Networks*. 2020.

[15] Tengfei Chang et al. "Surviving the Hair Dryer: Continuous Calibration of a Crystal-Free Mote-on-Chip". en. In: *IEEE Internet of Things Journal* 9.6 (Mar. 2022), pp. 4737–4747. ISSN: 2327-4662, 2372-2541. DOI: 10.1109/JIOT.2021.3108077. URL: https://ieeexplore.ieee.org/document/9523577/ (visited on 03/22/2022).

[16] Yue Chen et al. "A Supply Pushing Reduction Technique for LC Oscillators Based on Ripple Replication and Cancellation". In: *IEEE Journal of Solid-State Circuits* 54.1 (Jan. 2019). Conference Name: IEEE Journal of Solid-State Circuits, pp. 240–252. ISSN: 1558-173X. DOI: 10.1109/JSSC.2018.2871195.

[17] Chen-Yuan Chu et al. "A 24GHz low-power CMOS receiver design". In: *2008 IEEE International Symposium on Circuits and Systems (ISCAS)*. ISSN: 2158-1525. May 2008, pp. 980–983. DOI: 10.1109/ISCAS.2008.4541584.

[18] Wayne Churaman et al. "The First Launch of an Autonomous Thrust-Driven Microrobot Using Nanoporous Energetic Silicon". In: *Microelectromechanical Systems, Journal of* 21 (Feb. 2012), pp. 198–205. DOI: 10.1109/JMEMS.2011.2174414.

[19] D. S. Contreras, D. S. Drew, and K. S. J. Pister. "First steps of a millimeter-scale walking silicon robot". In: *2017 19th International Conference on Solid-State Sensors, Actuators and Microsystems (TRANSDUCERS)*. 2017, pp. 910–913. DOI: 10.1109/TRANSDUCERS.2017.7994197.

[20] D. S. Contreras and K. S. J. Pister. "Dynamics of electrostatic inchworm motors for silicon microrobots". In: *2017 International Conference on Manipulation, Automation and Robotics at Small Scales (MARSS)*. July 2017, pp. 1–6. DOI: 10.1109/MARSS.2017.8001936.

[21] Daniel S. Contreras, Daniel S. Drew, and Kristofer S. J. Pister. "First steps of a millimeter-scale walking silicon robot". In: *2017 19th International Conference on Solid-State Sensors, Actuators and Microsystems (TRANSDUCERS)*. ISSN: 2167-0021. June 2017, pp. 910–913. DOI: 10.1109/TRANSDUCERS.2017.7994197.

[22] Daniel S. Contreras and K.S.J. Pister. "A Six-Legged MEMS Silicon Robot Using Multichip Assembly". In: *Solid State Sensors and Actuators Workshop, Hilton Head*. 2018.

[23] Nikolaus Correll, Samuel Rutishauser, and Alcherio Martinoli. "Comparing coordination schemes for miniature robotic swarms: A case study in boundary coverage of regular structures". In: *Experimental Robotics*. Springer. 2008, pp. 471–480.

[24] J. Crossley et al. "BAG: A designer-oriented integrated framework for the development of AMS circuit generators". In: *2013 IEEE/ACM International Conference on Computer-Aided Design (ICCAD)*. ISSN: 1558-2434. Nov. 2013, pp. 74–81. DOI: 10.1109/ICCAD.2013.6691100.

[25] Daniel S Drew, Brian Kilberg, and Kristofer SJ Pister. "Future mesh-networked pico air vehicles". In: *2017 International Conference on Unmanned Aircraft Systems (ICUAS)*. IEEE. 2017, pp. 1075–1082.

[26] Daniel S Drew et al. "Toward controlled flight of the ionocraft: a flying microrobot using electrohydrodynamic thrust with onboard sensing and no moving parts". In: *IEEE Robotics and Automation Letters* 3.4 (2018), pp. 2807–2813.

[27] Daniel S. Drew et al. "Toward Controlled Flight of the Ionocraft: A Flying Microrobot Using Electrohydrodynamic Thrust With Onboard Sensing and No Moving Parts". In: *IEEE Robotics and Automation Letters* 3.4 (Oct. 2018). Conference Name: IEEE Robotics and Automation Letters, pp. 2807–2813. ISSN: 2377-3766. DOI: 10.1109/LRA.2018.2844461.

[28] L. Fanori, A. Liscidini, and R. Castello. "Capacitive Degeneration in LC-Tank Oscillator for DCO Fine-Frequency Tuning". In: *Solid-State Circuits, IEEE Journal of* 45 (Jan. 2011), pp. 2737–2745. DOI: 10.1109/JSSC.2010.2077190.

[29] Joseph Greenspun and Kristofer S. J. Pister. "Ring GINA: A Wearable Computer Interaction Device". en. In: *Mobile Computing, Applications, and Services*. Ed. by Gérard Memmi and Ulf Blanke. Lecture Notes of the Institute for Computer Sciences, Social Informatics and Telecommunications Engineering. Cham: Springer International Publishing, 2014, pp. 98–103. ISBN: 978-3-319-05452-0. DOI: 10.1007/978-3-319-05452-0_8.

[30] D. Griffith et al. "A ±10ppm −40 to 125°C BAW-Based Frequency Reference System for Crystal-less Wireless Sensor Nodes". In: *2017 IEEE International Symposium on Circuits and Systems (ISCAS)*. May 2017, pp. 1–4. DOI: 10.1109/ISCAS.2017.8050282.

[31] Liang Han and Ke Wu. "24-GHz Integrated Radio and Radar System Capable of Time-Agile Wireless Communication and Sensing". In: *IEEE Transactions on Microwave Theory and Techniques* 60.3 (Mar. 2012). Conference Name: IEEE Transactions on Microwave Theory and Techniques, pp. 619–631. ISSN: 1557-9670. DOI: 10.1109/TMTT.2011.2179552.

[32] S. Hollar et al. "Solar powered 10 mg silicon robot". In: *IEEE The Sixteenth Annual International Conference on Micro Electro Mechanical Systems, 2003. MEMS-03 Kyoto.* ISSN: 1084-6999. Jan. 2003, pp. 706–711. DOI: 10.1109/MEMSYS.2003.1189847.

[33] Seth Hollar et al. "Solar powered 10 mg silicon robot". In: Feb. 2003, pp. 706–711. DOI: 10.1109/MEMSYS.2003.1189847.

[34] Allen Hsu et al. "Application of micro-robots for building carbon fiber trusses". In: *2016 international conference on manipulation, automation and robotics at small scales (MARSS)*. IEEE. 2016, pp. 1–6.

[35] Vikram Iyer et al. "Airdropping sensor networks from drones and insects". In: *Proceedings of the 26th Annual International Conference on Mobile Computing and Networking*. MobiCom '20. New York, NY, USA: Association for Computing Machinery, Sept. 2020, pp. 1–14. ISBN: 978-1-4503-7085-1. DOI: 10.1145/3372224.3419981. URL: https://dl.acm.org/doi/10.1145/3372224.3419981 (visited on 08/03/2023).

[36] Vikram Iyer et al. "Living IoT: A Flying Wireless Platform on Live Insects". In: *The 25th Annual International Conference on Mobile Computing and Networking*. MobiCom '19. New York, NY, USA: Association for Computing Machinery, Aug. 2019, pp. 1–15. ISBN: 978-1-4503-6169-9. DOI: 10.1145/3300061.3300136. URL: https://dl.acm.org/doi/10.1145/3300061.3300136 (visited on 08/03/2023).

[37] Vikram Iyer et al. "Wireless steerable vision for live insects and insect-scale robots". In: *Science robotics* 5.44 (2020).

[38] Noah Jafferis et al. "Untethered flight of an insect-sized flapping-wing microscale aerial vehicle". In: *Nature* 570 (June 2019), pp. 491–495. DOI: 10.1038/s41586-019-1322-0.

[39] Johannes James et al. "Liftoff of a 190 mg Laser-Powered Aerial Vehicle: The Lightest Wireless Robot to Fly". In: May 2018, pp. 1–8. DOI: 10.1109/ICRA.2018.8460582.

[40] Seokhyeon Jeong et al. "A Fully-Integrated 71 nW CMOS Temperature Sensor for Low Power Wireless Sensor Nodes". In: *IEEE Journal of Solid State Circuits*. 2014, pp. 1682–1693.

[41] Jin Jung et al. "Fingernail Configuration". In: *Archives of Plastic Surgery* 42 (Nov. 2015), p. 753. DOI: 10.5999/aps.2015.42.6.753.

[42] Jiahao Kang et al. "On-chip intercalated-graphene inductors for next-generation radio frequency electronics". en. In: *Nature Electronics* 1.1 (Jan. 2018). Number: 1 Publisher: Nature Publishing Group, pp. 46–51. ISSN: 2520-1131. DOI: 10.1038/s41928-017-0010-z. URL: https://www.nature.com/articles/s41928-017-0010-z (visited on 08/13/2023).

[43] Peter J. Kennedy et al. "Searching for nests of the invasive Asian hornet (Vespa velutina) using radio-telemetry". en. In: *Communications Biology* 1.1 (July 2018). Number: 1 Publisher: Nature Publishing Group, pp. 1–8. ISSN: 2399-3642. DOI: 10.1038/s42003-018-0092-9. URL: https://www.nature.com/articles/s42003-018-0092-9 (visited on 08/03/2023).

[44] Brian Kilberg. *Actuation and Localization of Resource-Constrained Autonomous Microrobotic Systems*. May 2021. URL: https://www2.eecs.berkeley.edu/Pubs/TechRpts/2021/EECS-2021-20.html (visited on 12/15/2021).

[45] Brian G. Kilberg et al. "Accurate 3D Lighthouse Localization of a Low-Power Crystal-Free Single-Chip Mote". In: *Journal of Microelectromechanical Systems* 29.5 (Oct. 2020). Conference Name: Journal of Microelectromechanical Systems, pp. 818–824. ISSN: 1941-0158. DOI: 10.1109/JMEMS.2020.3011460.

[46] Thomas Klose et al. "Fluidmechanical Damping Analysis of Resonant Micromirrors with Out-of-plane Comb Drive". In: *Proceedings of the COMSOL Conference 2008*. Hannover, Nov. 2008.

[47] Matt Last and Kris Pister. "An 8 mm3 digitally steered laser beam transmitter". In: *IEEE/LEOS Intl. Conf. Optical MEMS*. 2000.

[48] Yanqiao Li, Benjamin L Dobbins, and Jason T Stauth. "An Optically Powered, High-Voltage, Switched-Capacitor Drive Circuit for Microrobotics". In: *IEEE Journal of Solid-State Circuits* (2020).

[49] Zhaokai Liu. "Time-interleaved SAR ADC Design Using Berkeley Analog Generator". MA thesis. EECS Department, University of California, Berkeley, May 2020. URL: http://www2.eecs.berkeley.edu/Pubs/TechRpts/2020/EECS-2020-109.html.

[50] Chris Looney et al. "Detection and description of four Vespa mandarinia (Hymenoptera, Vespidae) nests in western North America". en. In: *Journal of Hymenoptera Research* 96 (Feb. 2023). Publisher: Pensoft Publishers, pp. 1–20. ISSN: 1314-2607. DOI: 10.3897/jhr.96.99307. URL: https://jhr.pensoft.net/article/99307/ (visited on 08/06/2023).

[51] Filip Maksimovic. "Monolithic Wireless Transceiver Design". PhD thesis. EECS Department, University of California, Berkeley, May 2020. URL: http://www2.eecs.berkeley.edu/Pubs/TechRpts/2020/EECS-2020-33.html.

[52] Filip Maksimovic et al. "A Crystal-Free Single-Chip Micro Mote with Integrated 802.15.4 Compatible Transceiver, sub-mW BLE Compatible Beacon Transmitter, and Cortex M0". In: *VLSI 2019*. IEEE. 2019, pp. C88–C89.

[53] Filip Maksimovic et al. "A Crystal-Free Single-Chip Micro Mote with Integrated 802.15.4 Compatible Transceiver, sub-mW BLE Compatible Beacon Transmitter, and Cortex M0". In: *2019 Symposium on VLSI Circuits*. ISSN: 2158-5636. June 2019, pp. C88–C89. DOI: 10.23919/VLSIC.2019.8777971.

[54] Filip Maksimovic et al. "Standards Compatible RF Networks without Crystals: A three-pin BLE beacon-on-a-chip". In: *Arm Research Summit 2019*. Sept. 2019.

[55] Murata Manufacturing. *Chip Monolithic Ceramic Capacitor for General GRM188R60G476ME15_ (0603, X5R:EIA, 47uF, DC4V)*. Nov. 2016. URL: https://search.murata.co.jp/Ceramy/image/img/A01X/G101/ENG/GRM188R60G476ME15-01.pdf.

[56] Tom Markvart and Luis Castañer. "Chapter I-1-A - Principles of Solar Cell Operation". en. In: *McEvoy's Handbook of Photovoltaics (Third Edition)*. Ed. by Soteris A. Kalogirou. Academic Press, Jan. 2018, pp. 3–28. ISBN: 978-0-12-809921-6. DOI: 10.1016/B978-0-12-809921-6.00001-X. URL: https://www.sciencedirect.com/science/article/pii/B978012809921600001X (visited on 07/27/2023).

[57] V. Milanovic. "Multilevel beam SOI-MEMS fabrication and applications". In: *Journal of Microelectromechanical Systems* 13.1 (Feb. 2004). Conference Name: Journal of Microelectromechanical Systems, pp. 19–30. ISSN: 1941-0158. DOI: 10.1109/JMEMS.2003.823226.

[58] V. Milanovic, M. Last, and K.S.J. Pister. "Laterally actuated torsional micromirrors for large static deflection". In: *IEEE Photonics Technology Letters* 15.2 (Feb. 2003). Conference Name: IEEE Photonics Technology Letters, pp. 245–247. ISSN: 1941-0174. DOI: 10.1109/LPT.2002.806085.

[59] V. Milanovic, G.A. Matus, and D.T. McCormick. "Gimbal-less monolithic silicon actuators for tip-tilt-piston micromirror applications". In: *IEEE Journal of Selected Topics in Quantum Electronics* 10.3 (May 2004). Conference Name: IEEE Journal of Selected Topics in Quantum Electronics, pp. 462–471. ISSN: 1558-4542. DOI: 10.1109/JSTQE.2004.829205.

[60] R.A. Miller et al. "Electromagnetic MEMS Scanning Mirrors for Holographic Data Storage". en. In: *1996 Solid-State, Actuators, and Microsystems Workshop Technical Digest*. Hilton Head, South Carolina, USA: Transducer Research Foundation, Inc., June 1996, pp. 183–186. ISBN: 978-0-9640024-1-8. DOI: 10.31438/trf.hh1996.42. URL: https://transducer-research-foundation.org/technical_digests/HiltonHead_1996/hh1996_0183.pdf (visited on 11/30/2021).

[61] Alex Moreno and Kristofer Pister. "Frequency Compensated Crystal-Free 802.15.4 Wireless Radio". In: *2022 IEEE Sensors*. ISSN: 2168-9229. Oct. 2022, pp. 1–3. DOI: 10.1109/SENSORS52175.2022.9967165.

[62] Alex Moreno et al. "Small Autonomous Robot Actuator (SARA): A Solar-Powered Wireless MEMS Gripper". In: *2021 IEEE International Conference on Robotics and Automation (ICRA)*. ISSN: 2577-087X. May 2021, pp. 7227–7233. DOI: 10.1109/ICRA48506.2021.9561294.

[63] Alex Moreno et al. "Solar-Powered Crystal-Free 802.15.4 Wireless Temperature Sensor". In: *2020 IEEE SENSORS*. ISSN: 2168-9229. Oct. 2020, pp. 1–4. DOI: 10.1109/SENSORS47125.2020.9278679.

[64] Alex Moreno et al. "Solar-Powered Crystal-Free 802.15.4 Wireless Temperature Sensor". In: *2020 IEEE Sensors*. IEEE. 2020, pp. 1–4.

[65] Jackson Paddock. "Redesigning Power Systems on a Single Chip Micro Mote with Berkeley Analog Generator Low Dropout Series Regulator Generation". MA thesis. EECS Department, University of California, Berkeley, May 2021. URL: http://www2.eecs.berkeley.edu/Pubs/TechRpts/2021/EECS-2021-124.html.

[66] P.R. Patterson et al. "A scanning micromirror with angular comb drive actuation". en. In: *Technical Digest. MEMS 2002 IEEE International Conference. Fifteenth IEEE International Conference on Micro Electro Mechanical Systems (Cat. No.02CH37266)*. Las Vegas, NV, USA: IEEE, 2002, pp. 544–547. ISBN: 978-0-7803-7185-9. DOI: 10.1109/MEMSYS.2002.984329. URL: http://ieeexplore.ieee.org/document/984329/ (visited on 11/30/2021).

[67] I. Penskiy and S. Bergbreiter. "Optimized electrostatic inchworm motors using a flexible driving arm". en. In: *Journal of Micromechanics and Microengineering* 23.1 (Dec. 2012). Publisher: IOP Publishing, p. 015018. ISSN: 0960-1317. DOI: 10.1088/0960-1317/23/1/015018. (Visited on 10/12/2020).

[68] J.K. Perng et al. "Acceleration sensing glove (ASG)". In: *Digest of Papers. Third International Symposium on Wearable Computers*. Oct. 1999, pp. 178–180. DOI: 10.1109/ISWC.1999.806717.

[69] Kurt E. Petersen. "Silicon Torsional Scanning Mirror". In: *IBM Journal of Research and Development* 24.5 (Sept. 1980). Conference Name: IBM Journal of Research and Development, pp. 631–637. ISSN: 0018-8646. DOI: 10.1147/rd.245.0631.

[70] Ahad M. Rauf et al. "TOWARDS AERODYNAMIC CONTROL OF MINIATURE ROCKETS WITH MEMS CONTROL SURFACES". In: *IEEE MEMS*. 2020.

[71] Jan S. Rentmeister et al. "A 120-330V, sub-μA, 4-Channel Driver for Microrobotic Actuators with Wireless- Optical Power Delivery and over 99% Current Efficiency". In: *2020 IEEE Symposium on VLSI Circuits*. Honolulu, HI, USA: IEEE, 2020.

[72] Jan S. Rentmeister et al. "A 120–330V, Sub-microA, 4-Channel Driver for Microrobotic Actuators with Wireless-Optical Power Delivery and over 99% Current Efficiency". In: *2020 IEEE Symposium on VLSI Circuits*. ISSN: 2158-5636. June 2020, pp. 1–2. DOI: 10.1109/VLSICircuits18222.2020.9162908.

[73] Kay Römer. "The lighthouse location system for smart dust". In: *Proceedings of the 1st international conference on Mobile systems, applications and services*. ACM. 2003, pp. 15–30.

[74] Kay Römer. "The Lighthouse Location System for Smart Dust." In: Jan. 2003.

[75] Kai-Uwe Roscher et al. "Driver ASIC for synchronized excitation of resonant micromirrors". In: *MOEMS Display and Imaging Systems*. Vol. 4985. SPIE, Jan. 2003, pp. 121–130. DOI: 10.1117/12.477810. URL: https://www.spiedigitallibrary.org/conference-proceedings-of-spie/4985/0000/Driver-ASIC-for-synchronized-excitation-of-resonant-micromirrors/10.1117/12.477810.full (visited on 04/11/2022).

[76] Michael Rubenstein et al. "Kilobot: A low cost robot with scalable operations designed for collective behaviors". In: *Robotics and Autonomous Systems* 62.7 (2014), pp. 966–975.

[77] Andrew P Sabelhaus et al. "TinyTeRP: A tiny terrestrial robotic platform with modular sensing". In: *2013 IEEE International Conference on Robotics and Automation*. IEEE. 2013, pp. 2600–2605.

[78] Ken Saito et al. "Study on electrostatic inchworm motor device for a heterogeneous integrated microrobot system". In: *Transactions of The Japan Institute of Electronics Packaging* 12 (2019), E18–009.

[79] H. Schenk et al. "Large deflection micromechanical scanning mirrors for linear scans and pattern generation". In: *IEEE Journal of Selected Topics in Quantum Electronics* 6.5 (Sept. 2000). Conference Name: IEEE Journal of Selected Topics in Quantum Electronics, pp. 715–722. ISSN: 1558-4542. DOI: 10.1109/2944.892609.

[80] C. B. Schindler et al. "A Jumping Silicon Microrobot with Electrostatic Inchworm Motors and Energy Storing Substrate Springs". In: *2019 20th International Conference on Solid-State Sensors, Actuators and Microsystems Eurosensors XXXIII (TRANSDUCERS EUROSENSORS XXXIII)*. 2019, pp. 88–91. DOI: 10.1109/TRANSDUCERS.2019.8808463.

[81] Craig Schindler et al. "15 Millinewton Force, 1 Millimeter Displacement, Low-Power MEMS Gripper". In: *IEEE MEMS*. 2020.

[82] Craig B Schindler et al. "A jumping silicon microrobot with electrostatic inchworm motors and energy storing substrate springs". In: *2019 20th International Conference on Solid-State Sensors, Actuators and Microsystems & Eurosensors XXXIII (TRANSDUCERS & EUROSENSORS XXXIII)*. IEEE. 2019, pp. 88–91.

[83] Craig B Schindler et al. "MIMSY: The Micro Inertial Measurement System for the Internet of Things". In: *2019 IEEE 5th World Forum on Internet of Things (WF-IoT)*. IEEE. 2019, pp. 329–334.

[84] Craig B. Schindler et al. "A Jumping Silicon Microrobot with Electrostatic Inchworm Motors and Energy Storing Substrate Springs". In: *2019 20th International Conference on Solid-State Sensors, Actuators and Microsystems Eurosensors XXXIII (TRANSDUCERS EUROSENSORS XXXIII)*. ISSN: 2167-0021. June 2019, pp. 88–91. DOI: 10.1109/TRANSDUCERS.2019.8808463.

[85] Metin Sitti et al. "Biomedical applications of untethered mobile milli/microrobots". In: *Proceedings of the IEEE* 103.2 (2015), pp. 205–224.

[86] Andrew Skelly and Mark Waugh. *Understanding DC Bias Characteristics in High-Capacitance MLCCs*. en. Author: Andrew+Skelly%3BMark+D.+Waugh Cnt_type: open Pg_type: articles Spon: 0 Topic: Advanced+Ceramics. Oct. 2009. URL: http://www.ceramicindustry.com/articles/90304-understanding-dc-bias-characteristics-in-high-capacitance-mlccs/ (visited on 08/11/2023).

[87] B. Soltanian and P. Kinget. "AM-FM conversion by the active devices in MOS LC-VCOs and its effect on the optimal amplitude". In: *IEEE Radio Frequency Integrated Circuits (RFIC) Symposium, 2006*. ISSN: 2375-0995. June 2006, 4 pp.–108. DOI: 10.1109/RFIC.2006.1651102.

[88] Ioana Suciu et al. "Dynamic Channel Calibration on a Crystal-Free Mote-on-a-Chip". In: *IEEE Access* 7 (2019), pp. 120884–120900.

[89] Ioana Suciu et al. "Experimental clock calibration on a crystal-free mote-on-a-chip". In: *IEEE INFOCOM 2019-IEEE Conference on Computer Communications Workshops (INFOCOM WKSHPS)*. IEEE. 2019, pp. 608–613.

[90] "Tape-Out Course: Silicon in a Semester [Society News]". In: *IEEE Solid-State Circuits Magazine* 14.2 (2022). Conference Name: IEEE Solid-State Circuits Magazine, pp. 66–75. ISSN: 1943-0590. DOI: 10.1109/MSSC.2022.3163619.

[91] Anju Toor et al. "Stencil-printed Lithium-ion micro batteries for IoT applications". en. In: *Nano Energy* 82 (Apr. 2021), p. 105666. ISSN: 2211-2855. DOI: 10.1016/j.nanoen.2020.105666. URL: https://www.sciencedirect.com/science/article/pii/S2211285520312398 (visited on 04/25/2022).

[92] A. Tortschanoff et al. "Position encoding and phase control of resonant MOEMS mirrors". en. In: *Sensors and Actuators A: Physical* 162.2 (Aug. 2010), pp. 235–240. ISSN: 09244247. DOI: 10.1016/j.sna.2010.01.011. URL: https://linkinghub.elsevier.com/retrieve/pii/S0924424710000129 (visited on 12/03/2021).

[93] Xavier Vilajosana et al. "OpenMote: Open-Source Prototyping Platform for the Industrial IoT". In: Sept. 2015. DOI: 10.1007/978-3-319-25067-0_17.

[94] Thomas Watteyne. *Tracking Asian Hornets (Vespa velutina) using a 244 mg Crystal-Free Single-Chip Mote*. ACM International Workshop on Nanoscale Computing Communication, and Applications, Nov. 2019.

[95] Thomas Watteyne et al. "Industrial wireless ip-based cyber–physical systems". In: *Proceedings of the IEEE* 104.5 (2016), pp. 1025–1038.

[96] Thomas Watteyne et al. "OpenWSN: a standards-based low-power wireless development environment". In: *Transactions on Emerging Telecommunications Technologies* 23.5 (2012), pp. 480–493.

[97] Brad Wheeler et al. "A Low-Power Optical Receiver for Contact-free Programming and 3D Localization of Autonomous Microsystems". In: *IEEE UEMCON*. 2019.

[98] Brad Wheeler et al. "A Low-Power Optical Receiver for Contact-free Programming and 3D Localization of Autonomous Microsystems". In: *2019 IEEE 10th Annual Ubiquitous Computing, Electronics Mobile Communication Conference (UEMCON)*. Oct. 2019, pp. 0371–0376. DOI: 10.1109/UEMCON47517.2019.8992964.

[99] Bradley Wheeler. "Low Power, Crystal-Free Design for Monolithic Receivers". PhD thesis. EECS Department, University of California, Berkeley, May 2019. URL: http://www2.eecs.berkeley.edu/Pubs/TechRpts/2019/EECS-2019-36.html.

[100] T. Yuan et al. "Temperature Calibration on a Crystal-Free Mote". In: *2020 IEEE 6th World Forum on Internet of Things (WF-IoT)*. Presented at *2020 IEEE 6th World Forum on Internet of Things (WF-IoT)*. 2020.

[101] T. Yuan et al. "Temperature Calibration on a Crystal-Free Mote". In: *2020 IEEE 6th World Forum on Internet of Things (WF-IoT)*. 2020, pp. 1–5. DOI: 10.1109/WF-IoT48130.2020.9221351.

[102] Xiaoyang Zhang, Liang Zhou, and Huikai Xie. "A Fast, Large-Stroke Electrothermal MEMS Mirror Based on Cu/W Bimorph". en. In: *Micromachines* 6.12 (Dec. 2015), pp. 1876–1889. ISSN: 2072-666X. DOI: 10.3390/mi6121460. URL: http://www.mdpi.com/2072-666X/6/12/1460 (visited on 11/30/2021).

[103] Xuan Zhang et al. "A fully integrated battery-powered system-on-chip in 40-nm CMOS for closed-loop control of insect-scale pico-aerial vehicle". In: *IEEE Journal of Solid-State Circuits* 52.9 (2017), pp. 2374–2387.

[104] R. S. Zoll et al. "MEMS-Actuated Carbon Fiber Microelectrode for Neural Recording". In: *IEEE Transactions on NanoBioscience* 18.2 (2019), pp. 234–239. DOI: 10.1109/TNB.2019.2905505.

[105] Rachel S. Zoll et al. "MEMS-Actuated Carbon Fiber Microelectrode for Neural Recording". In: *IEEE Transactions on NanoBioscience* 18.2 (Apr. 2019). Conference Name: IEEE Transactions on NanoBioscience, pp. 234–239. ISSN: 1558-2639. DOI: 10.1109/TNB.2019.2905505.